2017

Glacial to Holocene Changes in Eastern Equatorial Pacific Deep-Water Chemistry and Circulation

Natalie E. Umling
University of South Carolina

GLACIAL TO HOLOCENE CHANGES IN EASTERN EQUATORIAL PACIFIC DEEP-WATER CHEMISTRY AND CIRCULATION

By

Natalie E. Umling

Bachelor of Arts
University of North Carolina at Wilmington, 2013

Submitted in Partial Fulfillment of the Requirements

For the Degree of Doctor of Philosophy in

Geological Sciences

College of Arts and Sciences

University of South Carolina

2017

Accepted by:

Robert Thunell, Major Professor

Howie Scher, Committee Member

Michael Bizimis, Committee Member

Lori Ziolkowski, Committee Member

Ryan Rykaczewski, Committee Member

Cheryl L. Addy, Vice Provost and Dean of the Graduate School

ACKNOWLEDGEMENTS

I am immensely thankful to the support of my advisor Bob Thunell. He gave me the freedom to choose the direction of my research and to develop my own research interests while also providing me with the guidance and confidence to succeed with that research. The opportunities I have had as his student have been incredible and will likely forever shape the scientist I am and become. His high regard for correct usage of the English language has made me a far better writer than when I began my PhD. And luckily, we are both fans of the Oxford comma! I would also like to thank the members of my dissertation committee, who not only had insightful comments and advice for the preparation of my dissertation but also for my professional development as an early career scientist. Their guidance along the way has truly made me a better scientist and researcher. I don't know how to begin to thank my lab-mate Emily, whose close friendship and encouragement helped get me through grad school. I will be forever grateful that our time in Columbia overlapped with one another. I am also grateful for the irreplaceable lab support of Eric Tappa and many hours of help from Chris and Jess in the Marine Sediments lab. And thank you for Beth, Wayne, Brian, and Emily for the many hours of help in the CEMS lab. And finally, I would especially like to thank my family. Although they understand little of what it is that I do, their support has always been unwavering.

ABSTRACT

It has been hypothesized that the oceans store CO_2 during glacial periods and then release it to the atmosphere, causing the onset of warm interglacial periods (Sigman and Boyle, 2000). Documenting this past transfer of CO_2 between the oceans and atmosphere is of utmost importance for better understanding the impact that anthropogenic CO_2 has and will have on Earth's climate. The last deglaciation is a good analogue to modern increases in CO_2 and temperature and is recent enough to be studied using radiocarbon. This period provides important insights into the nature of climate changes during the transition from glacial to interglacial conditions. Specifically, this transition is punctuated by brief periods of rapid return to cold, glacial-like conditions followed by abrupt warmings that are synchronous with increases in atmospheric CO_2 depleted in ^{14}C (Hughen et al., 2000; Monnin et al., 2001). This link between increasing atmospheric CO_2 and abrupt temperature rise during deglaciation has prompted the search for the location of a suitably large ^{14}C-depleted pool of respired carbon in the oceans that could serve as the source for these large increases in atmospheric CO_2. Changes in the efficiency of the biological pump and in meridional overturning circulation have both been cited as possible mechanisms of respired carbon storage. We seek to understand the role of these mechanisms in the Eastern Equatorial Pacific (EEP) over the last 25,000 years using a combination of radiocarbon, trace element, and isotopic studies of deep-ocean chemistry.

TABLE OF CONTENTS

LIST OF TABLES

LIST OF FIGURES

LIST OF SYMBOLS

‰ ..... Per mil

μ ..... micro (10^{-6})

Ce/Ce* ..... Cerium anomaly

D ..... Distribution coefficient

$\Delta^{14}C$ ..... Measured radiocarbon content

$\Delta^{14}C_0$ ..... Initial radiocarbon content

$\Delta^{14}C_{0\text{-atm}}$ ..... Radiocarbon offset from the atmosphere

$\delta^{18}C$ ..... Oxygen isotopic composition

$\delta^{13}C$ ..... Carbon isotopic composition

$\delta^{13}C_{as}$ ..... The air-sea component of $\delta^{13}C$

$\Delta\delta^{13}C$ ..... Foraminiferal infaunal-epifuanal carbon isotope difference

$[CO_3^{2-}]$ ..... Carbonate ion concentration

$[CO_3^{2-}]_{sat}$ ..... Carbonate ion concentration at calcite saturation

$\Delta[CO_3^{2-}]$ ..... Degree of carbonate saturation

U_a ..... Authigenic uranium

LIST OF ABBREVIATIONS

ACC ..... Antarctic Circumpolar Current

Al/Ca ..... Aluminum to Calcium ratio

AMOC ..... Atlantic Meridional Overturning Circulation

AMS ..... Accelerator Mass Spectrometry

BA ..... Bølling Allerød

B/Ca ..... Boron to Calcium ratio

B-P ..... Benthic-Planktonic offset

Cd/Ca ..... Cadmium to Calcium ratio

CdS ..... Cadmium sulfide

CEP ..... Central Equatorial Pacific

C. oolina ..... *Chilostomella oolina*

C. wuellerstorfi ..... *Cibicidoides wuellerstorfi*

EEP ..... Eastern Equatorial Pacific

EqPIW ..... Equatorial Pacific Intermediate Water

ETP ..... Elastic Tie-Pointing

EUC ..... Equatorial Undercurrent

Fe/Ca ..... Iron to Calcium ratio

GICC05 ..... Greenland Ice Core Chronology 05

GLODAP ..... Global Data Analysis Project

GRIP ..... Greenland Ice core Project

HS1 ..... Heinrich Stadial 1

ICP-MS ..... Inductively coupled plasma mass spectrometry

ka ..... Thousands of years ago

km ..... kilometers

kyr ..... Thousands of years

LCDW ..... Lower Circumpolar Deep Water

LGM ..... Last Glacial Maximum

m ..... meters

mg ..... miligram

Mg/Ca ..... Magnesium to Calcium ratio

mol kg^{-1} ..... mol per kilogram

mmol mol^{-1} ..... 10^{-3} mol per mol

Mn/Ca ..... Manganese to Calcium ratio

NADW ..... North Atlantic Deep Water

N. dutertrei ..... *Neogloboquadrina dutertrei*

nmol kg^{-1} ..... 10^{-9} mol per kilogram

NPDW ..... North Pacific Deep Water

PAAS ..... Post-Archaean Australian Shale

PDW ..... Pacific Deep Water

ppm ..... parts per million

REE ..... Rare Earth Element

R/V ..... Research Vessel

SAMW ..... Sub-Antarctic Mode Water

spp ..... Species (plural)

SST ..... Sea Surface Temperature

U/Ca ..... Uranium to Calcium ratio

UCDW ..... Upper Circumpolar Deep Water

U/Mn ..... Uranium to Manganese ratio

µg ..... microgram

µmol kg^{-1} ..... 10^{-6} mol per kilogram

µmol mol^{-1} ..... 10^{-6} mol per mol

WEP ..... Western Equatorial Pacific

YD ..... Younger Dryas

yrs BP ..... years before present

MOTIVATION

Carbon dioxide is the primary atmospheric gas associated with greenhouse forcing, with concentrations of atmospheric CO_2 playing a large role in setting Earth's thermostat (Lacis et al., 2010). The anthropogenic increase in atmospheric CO_2 since the onset of the industrial revolution is widely considered to be the primary driver of changing climate conditions during the past two centuries (IPCC Report, 2014). Similarly, greenhouse gas forcing has been shown to amplify the orbital cycles of the last one million years, driving the transition between glacial and interglacial conditions (Sigman and Boyle, 2000). It has been hypothesized that the oceans store CO_2 during glacial periods and then release it to the atmosphere, causing the onset of warm interglacial periods (Sigman and Boyle, 2000). Documenting this past transfer of CO_2 between the oceans and atmosphere is of utmost importance to understanding the role the oceans play in modifying the natural variability of atmospheric CO_2 during glacial-interglacial cycles and to predict the role the oceans will play in an anthropogenically driven high-CO_2 world.

The overarching goal of my dissertation research is to better understand how the oceans store carbon during glacial periods and then release this carbon to the atmosphere during deglaciations. Specifically, my research focuses on the CO_2 and temperature increases of the last deglacial period (~20,000-10,000 years ago) as it is recent enough to trace carbon sources using radiocarbon, and records for this period can be of sufficiently high-resolution to study rapid climate changes occurring over just several hundred to

several thousand years. This period provides important insights into the transition from glacial to interglacial conditions and the mechanisms that may play a role during present and future rapid climate change. Specifically, this transition is defined by gradually increasing atmospheric CO_2 overprinted by periods of rapid CO_2 rise occurring over several hundred years (Hughen et al., 2000; Marcott et al., 2014; Monnin et al., 2001). In addition to increasing CO_2, gradual decreases in atmospheric radiocarbon content have been recorded over this same period. Radiocarbon is formed cosmogenically in the upper levels of the atmosphere, and the production of radiocarbon varies through time depending on the strength of Earth's magnetic field and the number of cosmic rays hitting Earth (Lal and Peters, 1967). However, the radiocarbon decreases during the last deglaciation cannot be accounted for by changes in production alone (Hain et al., 2014), suggesting the transfer of CO_2 from a radiocarbon-depleted carbon reservoir. This has prompted the search for the location of a suitably large ^{14}C-depleted pool of carbon in the oceans that could serve as the source for these large increases in atmospheric CO_2, as the deep ocean is the largest carbon reservoir to exchange with the atmosphere on hundred and thousand year timescales (Holmen, 1992). While, both physical and biological mechanisms have been suggested as possible drivers of oceanic CO_2 storage and release, there is little general agreement on the relative role of these mechanisms.

Many of the suggested physical drivers focus on changes in the rate and pathway of oceanic circulation as mechanisms for the glacial-interglacial transfer of carbon between the oceans and the atmosphere. Specifically, it was predicted that deep-water production weakened during glacial periods resulting in the build-up of CO_2 due to decreased circulation rates and increased isolation of these water masses from the

atmosphere (Huang et al., 2014; Pahnke et al., 2008). The resumption of a vigorous circulation during deglaciation would rapidly restore communication of isolated deep waters with surface waters and the atmosphere, producing the observed periods of depleted atmospheric ^{14}C and increased CO_2 (Keeling and Stephens, 2001; Broecker et al., 2007; Matsumoto and Yokoyama, 2013; Ferrari et al., 2014). However, there has been much disagreement about the feasibility of an isolated abyssal reservoir, with critics suggesting that the required amount of respiration for this stagnant water-mass would result in anoxic conditions (Hain et al., 2011). So far, little evidence of anoxic conditions and decreased radiocarbon in abyssal-depth waters has been found (Broecker et al., 2004; Jaccard and Galbraith, 2011; Lund, 2013; Rae et al., 2014; Ronge et al., 2016).

In light of these shortcomings, many researchers have focused instead on the biological transfer of carbon from the surface ocean to the deep ocean and the overall efficiency of this biological pump (Anderson et al., 2002; Boyle, 1988; Jaccard et al., 2009; Martin, 1990; Matsumoto et al., 2002). Phytoplankton take up CO_2 from the surface ocean during photosynthesis and subsequently export CO_2 to the deep ocean as organic carbon rain. When the biological pump is inefficient, phytoplankton in the surface ocean are not able to fully use the available nutrients leading to a greater amount of unused, preformed nutrients and a missed opportunity to sequester CO_2. It has been hypothesized that increased atmospheric transport of iron due to glacial erosion and increased aridity could have alleviated iron-limiting conditions in some areas during the glacial period (Martin, 1990). This would have led to a more efficient biological pump and increased CO_2 drawdown. During deglaciation, biological pump efficiency may have decreased due to a declining glacial iron supply resulting in a reduction of the CO_2

transfer to the deep ocean, allowing evasion of excess CO_2 to the atmosphere. A flaw in the hypothesized biological mechanisms of oceanic atmospheric CO_2 exchange is that the biological sequestration of atmospheric CO_2 could at most have accounted for only half of the observed glacial-interglacial atmospheric CO_2 change, requiring a secondary mechanism to account for the full CO_2 change (Kohfeld et al., 2005).

The aim of my dissertation research was to document changes in past oceanic chemistry and circulation in order to evaluate the proposed mechanisms for the glacial-interglacial transfer of CO_2 between the oceans and atmosphere. This was accomplished by developing records of past ocean chemistry using the shells of single-celled protists called foraminifera. As they build their calcite shells, the chemistry of the water in which they live gets incorporated in those shells, and those shells are preserved in sediments allowing us to perform a variety of geochemical analyses to constrain past seawater chemistry. Chapter one of this study uses foraminiferal radiocarbon analyses to assess the physical drivers of oceanic CO_2 sequestration during the last glacial period and subsequent deglacial evasion of this reservoir to the atmosphere. The biological sequestration of CO_2 is investigated in chapter two of this study to evaluate whether changes in the efficiency of the biological pump may have played a role in glacial atmospheric CO_2 drawdown. This is accomplished by documenting changes in respired carbon storage using foraminiferal stable isotope and trace element analyses of past oceanic oxygenation and carbonate chemistry. Finally, the role of circulation in driving changes in the biological pump and in ventilation is investigated in chapter three by characterizing deep and mid-depth water-masses using paired stable isotope and trace element analyses.

This study focuses on the eastern equatorial Pacific as this region is the largest modern oceanic source of CO_2 to the atmosphere (Pennington et al., 2006) making it particularly well suited for investigating the transfer of CO_2 between the oceans and the atmosphere. In this region, CO_2 is brought to the surface ocean by equatorial upwelling, northward advection of cool, nutrient rich waters from the Peru current, and upwelling of cold equatorial undercurrent waters off the Galapagos. This oceanic evasion of CO_2 is modified by the biological uptake of CO_2 during photosynthesis, which works to stem some of the CO_2 leak to the atmosphere. Productivity in this region is spatially variable and is limited in some areas by nitrate availability whereas other regions have excess nitrate and are limited instead by micronutrients such as iron. Reductions in nutrient limiting conditions through time could work to limit the CO_2 flux to the atmosphere.

CHAPTER 1

SYNCHRONOUS DEGLACIAL THERMOCLINE AND DEEP-WATER VENTILATION IN THE EASTERN EQUATORIAL PACIFIC[1]

[1] Umling, N.E., Thunell, R.C., 2017. *Nature Communications*. 8, 14203. doi:10.1038/ncomms14203. Reprinted here with permission of publisher.

1.1 Abstract

The deep-ocean is most likely the primary source of the radiocarbon depleted CO_2 released to the atmosphere during the last deglaciation. While there are well-documented millennial-scale $\Delta^{14}C$ changes during the most recent deglaciation, most marine records lack the resolution needed to identify more rapid ventilation events. Furthermore, potential age model problems with marine $\Delta^{14}C$ records may obscure our understanding of the phase relationship between inter-ocean ventilation changes. Here we reconstruct changes in deep water and thermocline radiocarbon content over the last deglaciation in the Eastern Equatorial Pacific (EEP) using benthic and planktonic foraminiferal ^{14}C. Our records demonstrate that ventilation of EEP thermocline and deep waters occurred synchronously during the last deglaciation. Additionally, both gradual and rapid deglacial radiocarbon changes in these Pacific records are coeval with changes in Atlantic records. This in-phase behavior suggests that Southern Ocean overturning was the dominant driver of changes in Atlantic and Pacific ventilation during deglaciation.

1.2 Introduction

Atmospheric CO_2 plays an important role in setting Earth's thermostat and changes in atmospheric CO_2 provide the feedback mechanism needed to amplify the orbitally-driven Pleistocene glacial-interglacial climate cycles (Sigman and Boyle, 2000). Documenting the transfer of CO_2 between oceanic and atmospheric reservoirs is paramount to understanding the relationship between CO_2 and climate change. Radiocarbon studies are uniquely suited for identifying the pathway and rate of CO_2 exchange between the oceans and atmosphere by providing a tool for tracing carbon sources over the past 40,000 years. The last deglacial period (~20,000-10,000 years ago)

is recent enough to be studied using radiocarbon and provides important insights into the nature of climate transitions and the role of tipping points in predicting abrupt shifts in the climate system (Lenton et al., 2012).

Antarctic ice core records spanning the last deglaciation reveal a tight coupling between changes in atmospheric CO_2 and temperature (Parrenin et al., 2013). In particular, these records contain two millennial-scale episodes of increasing atmospheric CO_2 that are synchronous with decreases in atmospheric $\Delta^{14}C$ (Hughen et al., 2000; Monnin et al., 2001). The first is a large 170‰ drop in $\Delta^{14}C$ and ~50 ppmv rise in CO_2 occurring during late Heinrich Stadial 1 (HS1; ~17.5 to 14.7 ka), and the second is a smaller $\Delta^{14}C$ drop of 70‰ and ~30 ppmv rise in CO_2 marking the end of the Younger Dryas (YD; ~12.8 to 11.5 ka; Monnin et al., 2001; Hain et al., 2014; Figure 1.1). The magnitudes of these events suggest that the intermediate and/or deep ocean must be the primary source of this excess CO_2 (Broecker and Barker, 2007), although identifying the specific source region has proven difficult. There is evidence to suggest that the large fluctuations in atmospheric CO_2 are driven by changes in Southern Ocean meridional overturning circulation (Watson and Naveira Garabato, 2006).

Previous studies from both intermediate and deep water locations yield conflicting results regarding the magnitude and extent of the glacial carbon pool, as well as the timing of deglacial ventilation events (Rae e al., 2014; Marchitto et al., 2007; Lindsay et al., 2015; Burke and Robinson, 2012; Skinner et al., 2010; Thornalley et al., 2011; Robinson et al., 2005; Chen et al., 2015; Skinner et al., 2014; de la Fuente et al., 2015; Sikes et al., 2000; Broecker et al., 2008; De Pol-Holz et al., 2010; Siani et al., 2013; Burke et al., 2015; Freeman et al., 2015; Skinner et al., 2015; Ronge et al., 2016; Sikes et

al., 2016) , resulting in difficulty resolving both regional and inter-ocean ventilation signals. These inconsistencies may be due, at least in part, to the age models used for the different records. Traditionally, a constant reservoir age is used when calibrating foraminiferal radiocarbon dates (Broecker et al., 2008, De Pol-Holz et al., 2010; Freeman et al., 2015). However, variability in marine reservoir ages of at least several hundred years have been documented for the Pacific since the last glacial maximum (LGM) from dating of contemporaneous marine and terrestrial samples (Ortlieb et al., 2011), from correlation of marine tephra layers to dated terrestrial eruptions (Siani et al., 2013), and from paired U-Th and ^{14}C dating of corals (Paterne et al., 2004). Additionally, reservoir age variability of >800 years has been suggested from tuning of plateaus in atmospheric ^{14}C (Sarnthein et al., 2015; Balmer et al., 2016), from several tephra-dated records (Sikes et al., 2000; 2016), and from correlation of climatic events to age control points in independently dated oxygen isotope records from the Hulu Cave speleothem or Greenland and Antarctic ice cores (Skinner et al., 2010; 2014; 2015). Without independent age control of radiocarbon-derived ventilation records, it is difficult to quantify the actual magnitude of error introduced into initial foraminiferal radiocarbon content ($\Delta^{14}C_0$) calculations from age model uncertainty (Cook and Keigwin, 2015). Furthermore, age model uncertainties make it difficult to determine whether ventilation events in different ocean basins occur synchronously or if there is an inter-ocean ventilation seesaw associated with the waxing of North Pacific Deep Water (NPDW) production when North Atlantic Deep Water (NADW) production waned (Freeman et al., 2015).

Here we reconstruct surface and deep water mass radiocarbon contents in the Eastern Equatorial Pacific (EEP) from sediment core TR163-23 (0°24'N, 92°09'W; 2,730 m water depth). This core site is located within the eastern equatorial cold tongue region off the Galapagos platform, along the return pathway of Pacific Deep Water (PDW; Figure 1.2). The Galapagos region presently is influenced by the upwelling of nutrients and CO_2 from the Equatorial Undercurrent (EUC) into thermocline depth waters (Toggweiler et al., 1991). The southern hemisphere currently accounts for ~2/3 of the source waters feeding the EUC with Sub-Antarctic Mode Water (SAMW) formed along the northern edge of the Antarctic Circumpolar Current (ACC) contributing much of the $\Delta^{14}C$ signature (Toggweiler et al., 1991). Consequently, TR163-23 is ideally positioned to record Southern Ocean-sourced ventilation of both thermocline and deep waters. We develop a well constrained age model for TR163-23 that does not require a static reservoir age and minimizes chronological uncertainty associated with the calculation of past radiocarbon content. Our records demonstrate that EEP thermocline and deep water ventilation occurred synchronously over the last 25,000 yrs. They also indicate that both Atlantic and Pacific ventilation were sensitive to changes in Southern Ocean deep-water formation consistent with a southern driver of deglacial climate change (Sigman and Boyle, 2000; Keeling and Stephens, 2001; Watson et al., 2015).

1.3 Results

1.3.1 Age Model Development

To constrain age model uncertainty, three independent age models have been developed for TR163-23 (Figure 1.3), along with an age model based on a constant reservoir correction ($\Delta R=147\pm13$) of 31 *Neogloboquadrina dutertrei* radiocarbon ages

(Supplementary tables A.1 and A.2). Two of the age models were derived from the tuning of a planktonic foraminiferal (*Globigerinoides ruber)* oxygen isotope record for TR163-23 (Supplementary Fig. A.1) to the $\delta^{18}O$ records from the GRIP Greenland ice core (Figure 1.3a; Johnson et al., 1997; Rasmussen et al., 2014; Seierstad et al., 2014) and the Hulu Cave speleothems (Wang et al., 2001; Wu et al., 2009; Southon et al., 2012; Figure 1.3b). In addition, we used ^{14}C plateau tuning of the *N. dutertrei* radiocarbon dates following the procedure presented in Sarnthein et al. (2015; Figure 1.3c) to develop a third independent age model. Reference record age estimates for the various tie points (Supplementary Table A.3) were translated to TR163-23 using the elastic tie-point (ETP) method (Heaton et al., 2013), and the final age models were developed using the Bayesian age-depth modeling program BACON (Blaauw and Christen, 2011; Supplementary Tables 4-5).

This method was chosen as it provides a computationally feasible way to quantify uncertainty associated with the transfer of age-depth estimates from a reference chronology. Tie-point constraint allows us to estimate reservoir age changes over the last glacial-interglacial transition, and our sampling resolution of TR163-23 permits the observation of sub-millennial scale ventilation events. Above all, this technique of age model construction is not reliant upon the assumption of an unchanging reservoir age throughout deglaciation and provides more realistic estimates of age-model uncertainty. We did not have sufficient resolution during the Holocene to identify tie points, and as a result this portion of the chronology was constructed using three calibrated ($\Delta R=147\pm13$) *N. dutertrei* calendar ages. All three of the independently developed age models yield results that are indistinguishable from one another (Figure 1.4). Conversely, the

radiocarbon-based age model yields significantly different and generally older ages (Figure 1.4). For the purpose of this study, we use the Hulu cave speleothem tuned age model to interpret our results from the Galapagos. A more detailed description of the procedures used to establish each of the four age models is presented in the Methods.

1.3.2 Thermocline and Deep Water Ventilation

The deep and thermocline carbon pools were assessed through calculation of the paleo-reservoir ages and the anomaly of the initial foraminiferal radiocarbon content ($\Delta^{14}C_0$) from the IntCal13 atmospheric record (Reimer et al., 2013), or $\Delta^{14}C_{0\text{-}atm}$ as defined by Cook and Keigwin (2015). Contemporaneous atmosphere ^{14}C and $\Delta^{14}C$ values were averaged around associated Hulu-tuned age model 2σ error windows, and the error was estimated from the standard deviation of each averaged value. Reservoir ages and $\Delta^{14}C_{0\text{-}atm}$ values were calculated from measured radiocarbon ages of mixed benthic foraminifera for deep waters and of *N. dutertrei* for thermocline depths (Figure 1.5; Supplementary Table A.6). An initial increase in EEP $\Delta^{14}C_{0\text{-}atm}$ at ~17.5 ka coincides with the onset of rising atmospheric CO_2 at the beginning of HS1 (Parrenin et al., 2013; Marcott et al., 2014), with a second period of increasing $\Delta^{14}C_{0\text{-}atm}$ corresponding to the YD-Holocene transition (Figure 1.6). These two episodes of gradually increasing $\Delta^{14}C_{0\text{-}atm}$ are separated by a period of generally well ventilated thermocline and deep waters during the Bølling-Allerød (BA), a time when atmospheric CO_2 levels remained constant. For TR163-23, benthic and planktonic foraminiferal ^{14}C offsets from the atmosphere co-vary and as a result the B-P offset changes very little over the past 22,000 years, remaining close to the modern difference of ~1,250 ^{14}C years (Figure 1.5). Although the radiocarbon content in the EEP is primarily increasing throughout the deglaciation, there

are three brief periods of little to no increase or even decline in deep water $\Delta^{14}C_{0\text{-atm}}$ (15.6-15.1 ka; 14.6-13.3 ka; 13.1-12.4 ka). Each of these events is followed by a period of rapid $\Delta^{14}C_{0\text{-atm}}$ increase (15.1-14.6 ka; 13.3-13.1 ka; 12.4-10.8 ka). Our results clearly demonstrate that the $\Delta^{14}C_{0\text{-atm}}$ of EEP thermocline and deep waters varied by at least 250‰ since the last glacial period (Figure 1.6).

1.4 Discussion

Benthic-planktonic (B-P) ^{14}C offsets have often been used to estimate past ventilation changes (Broecker et al., 2008; De Pol-holz et al., 2010; Freeman et al., 2015). However, concurrent increases in surface ocean reservoir ages and bottom water radiocarbon depletion, as seen in this study, may lead to the underestimation of ventilation changes calculated simply from B-P ^{14}C age differences (Sikes et al., 2016). While both TR163-23 and Panama Basin core ODP1240 (de la Fuente et al., 2015) suggest similar B-P offsets during the deglacial, ODP1240 indicates an overall decrease of ~870 years in the B-P offset from the glacial to the Holocene (Figure 1.5). This dissimilarity in the two records could be due to differences in stratification through time between the two locations or it could be due to the fact that we have very little data for TR163-23 older than HS1 and thus are not capturing the true glacial B-P differences at our core location. Simultaneous deglacial benthic and planktonic reservoir age changes during deglaciation have also been observed in the southeast (Siani et al., 2013) and southwest Pacific (Skinner et al., 2015; Sikes et al., 2016; Sikes and Guilderson, 2016). This observation is consistent with modeling studies suggesting that surface reservoir ages are influenced not only by changes in lateral and vertical mixing, but also by the

"ρCO_2 effect" in which higher atmospheric CO_2 concentrations result in an increased oceanic equilibration rate of $\Delta^{14}C$ (Galbraith et al., 2015).

Our B-P and $\Delta^{14}C_{0\text{-atm}}$ results indicate that increases in both thermocline and deep water radiocarbon content not only occurred synchronously over the last deglaciation but that the magnitude of change was similar at both depths (Figure 1.6). Taken together, these records suggest that the initial oceanic "flushing" of the respired carbon reservoir was likely completed by ~14.5 ka and that any continued ventilation during the BA did not release a significant amount of carbon to the atmosphere. In addition, regrowth of the terrestrial biosphere during the BA may have contributed to the drawdown of CO_2 (Bauska et al., 2016; Crichton et al., 2016), offsetting any oceanic CO_2 ventilation during this period. The ^{14}C-depleted deep waters at our site likely represent depletions within PDW as it flows southward at mid-water depths (2-3.5 km). Similar radiocarbon anomalies have been recorded at this depth range in high latitudes in the Gulf of Alaska (Rae et al., 2014), off New Zealand (Ronge et al., 2016; Sikes et al., 2016), in the northwest Atlantic (Robinson et al., 2005), and in the south Atlantic (Burke et al., 2015; Skinner et al., 2014). Thus, this mid-depth carbon reservoir (Burke et al., 2015) appears to have been a pervasive feature of the glacial ocean. The ventilation pathway of this carbon to surface waters is less clear. The simultaneous ^{14}C depletions in EEP deep and thermocline waters indicate that the EUC likely transported carbon to upwelling zones in the Eastern Pacific, much as it does at present. Indeed, boron isotope derived pH estimates suggest that ventilation in the EEP was a significant source of CO_2 to the atmosphere during the deglaciation (Martínez-Botí et al., 2015). While SAMW is a major contributor to EUC waters, significantly aged SAMW has yet to be identified in the

Southern Ocean after ~18 ka (Sikes et al., 2016). Although the north Pacific currently produces only ~1/3 of EUC waters (Rodgers et al., 2003), it could have been a more important source of ^{14}C-depleted waters to the EUC during deglaciation.

As mentioned, the last deglaciation is marked by two millennial scale periods of increasing atmospheric CO_2 (17.5-14.5 ka; 13-11.5 ka), which are overprinted by several short-lived, rapid increases and plateaus (Marcott et al., 2014; Figure 1.6). Generally, each period of little to no increase or even decline in $\Delta^{14}C_{0\text{-atm}}$ appears to correspond with a pause in the build-up of atmospheric CO_2 (Marcott et al., 2014) and may be indicative of the establishment of brief periods of stable climate conditions (Figure 1.6). Alternating periods of oceanic ventilation and stratification during deglaciation appear to be tightly coupled to the increases and plateaus, respectively, in the CO_2 record, beginning with the initial rise in CO_2 and the onset of increasing ventilation in marine records at 17.5 ka (Marcott et al., 2014). More importantly, this emphasizes the integral role of oceanic ventilation in modulating atmospheric CO_2.

The West Antarctic Ice Sheet Divide Ice Core (WDC) atmospheric CO_2 record is marked by three centennial-scale increases during the last deglaciation at ~16.3, 14.8, and 11.7 ka (Marcott et al., 2014; Figure 1.6). No marine equivalent of the 16.3 ka increase in atmospheric CO_2 has been identified in Southern Ocean ^{14}C records. However, high latitude ventilation records from the North Pacific (Rae et al., 2014), Nordic Seas (Thornalley et al., 2015), and Iceland margin (Thornalley et al., 2011) record decreased deep water reservoir ages at ~16 ka. Concurrent decreases in surface water reservoir ages have been recorded in the sub-tropical south Atlantic at 16.3 ka (Balmer et al., 2016). While we see no evidence of NPDW ventilation at this time in our benthic $\Delta^{14}C_{0\text{-atm}}$

record, thermocline waters at our site display a small excursion towards younger radiocarbon values and less negative $\Delta^{14}C_{0\text{-}atm}$. This thermocline event is reduced in magnitude relative to that seen in North Pacific records and is consistent with a smaller proportion of northern relative to southern sourced waters incorporated into the EUC waters feeding our study site. Alternately, the 16.3 ka CO_2 increase may not be due to increased ocean ventilation but rather to the transfer of terrestrial carbon to the atmosphere (Balmer et al., 2016; Bauska et al., 2016). In contrast, the 14.8 ka event at the HS1-Bølling transition is coincident with a ~200‰ increase in $\Delta^{14}C_{0\text{-}atm}$ in both EEP thermocline and deep waters (Figure 1.6). This is easily the largest magnitude ventilation change recorded in TR163-23 and it is likely responsible for release of a significant amount of the carbon stored in the mid-depth reservoir. After a period of generally decreasing $\Delta^{14}C_{0\text{-}atm}$ from ~14.1-12.4 ka, TR163-23 records the resumption of increased EEP ventilation at ~12.4 ka during the Younger Dryas. However, during this period our record has insufficient resolution to identify the presence of a distinct EEP ventilation event associated with the rapid 100-200 year long increase in CO_2 at ~11.7 ka. Nevertheless, a significant rapid increase in $\Delta^{14}C_{0\text{-}atm}$ is recorded at this time in intermediate depth waters off Baja, California (Marchitto et al., 2007; Lindsay et al., 2015), supporting a link between ocean ventilation and the centennial-scale CO_2 rise at ~11.7 ka.

While the rapid increases in CO_2 at 14.8 and 11.7 ka coincide with changes in ocean ventilation, we also observe 75‰ and 100‰ $\Delta^{14}C_{0\text{-}atm}$ increases in EEP deep and thermocline depth waters, respectively, during the late-BA (~13.0-13.3 ka) that are not associated with an increase in atmospheric CO_2 (Figure 1.6). Although changes in

thermocline depth or upwelling strength can result in $\Delta^{14}C$ variability, the magnitude of the late-BA increase in $\Delta^{14}C_{0\text{-atm}}$ far exceeds the range of thermocline driven seasonal and decadal variability observed in Galapagos coral radiocarbon over the last 400 years (Druffel et al., 2007). This suggests that although upwelling may have increased at ~13.3 ka, a change in endmember $\Delta^{14}C$ is required to produce an increase of the magnitude we observe at this time. Several explanations could account for the lack of an equivalent late-BA increase in atmospheric CO_2: (1) a more efficient biological pump reduced the "leak" of CO_2 to the atmosphere, (2) the re-growth of terrestrial forests caused a draw-down of atmospheric CO_2, and/or (3) decreased air-sea exchange in the North Atlantic or Southern Ocean due to changes in wind stress and/or sea ice extent kept pace with ventilation, sequestering an amount of carbon comparable to that released in the EEP (Marcott et al., 2014).

Using only marine ^{14}C records with independently constrained age models (Table 1) we find that EEP reservoir age changes are coherent with both shallow and deep Atlantic and Pacific reservoir ages, not only at the millennial scale but also with more rapid ventilation events (Figure 1.7). Specifically, gradually increasing ventilation early in HS1 (~17.5 ka) followed by an abrupt acceleration in the rate of ventilation coincident with the ~14.8 ka rise in atmospheric CO_2 is recorded in the EEP (this study), the subtropical NE Pacific (Marchitto et al., 2007; Lindsay et al., 2015), the subpolar NE Pacific (Rae et al., 2014), the Equatorial Atlantic (Chen et al., 2015), the North Atlantic (Thornalley et al., 2011; Robinson et al., 2005; Skinner et al., 2014), and the sub-polar South Atlantic (Skinner et al., 2010). Among these records, the EEP (this study), the subtropical NE Pacific (Marchitto et al., 2007; Lindsay et al., 2015), and the North

Atlantic (Thornalley et al., 2011; Skinner et al., 2014) also indicate a period of enhanced ventilation during the late Younger Dryas (Figure 1.7). Using the Bayesian age-depth modeling program BACON (Blaauw et al., 2007; Blaauw and Christen, 2011), each of these records was analyzed for the probability that the 14.8 ka ventilation event occurred at a given point in time from 13-18 ka. For each region, the probability of this event occurring at a given point in time was combined with the event probability for TR163-23 to determine the likelihood that EEP ventilation was occurring simultaneously with ventilation in the Atlantic and Southern oceans. Taking into account chronological uncertainty, rapid ventilation in the EEP during the HS1-BA transition was synchronous with the North Atlantic (Figure 1.8) but did not show significant likelihood of synchronicity with the Southern Ocean. Rather, the Southern Ocean ventilation event associated with the 14.8 ka atmospheric CO_2 excursion (Marcott et al., 2014) occurs slightly earlier than in the Eastern Pacific and the North Atlantic. Because of their low resolution, it is not possible to calculate the synchronicity of events from the equatorial Atlantic coral records.

The internal consistency of the Atlantic and Pacific ventilation records argues against the existence of inter-ocean differences in the timing of ventilation changes during the last deglaciation (Freeman et al., 2015). Furthermore, the early onset of ventilation in the Southern Ocean due to overturning (Watson et al., 2015) suggests that this region was the dominant driver of deglacial ocean ventilation that then propagated northward into both the Pacific and Atlantic basins. The close correlation between Greenland ice core and Gulf of Alaska oxygen isotope records has been used as a basis for suggesting the close coupling and synchronization of poleward heat transport in the

Pacific and Atlantic oceans during the last deglaciation (Praetorius and Mix, 2014). Similarly, the results of our study suggest that ventilation of the Atlantic and Pacific Oceans was also synchronous during the most recent deglaciation (Figure 1.8).

1.5 Methods

1.5.1 Radiocarbon Analysis

Sediment core TR163-23 (0°24'N, 92°09'W) was collected from 2,730 m water-depth off the western margin of the Galapagos Islands during R/V Trident cruise TR-163 in February 1975. Sedimentation rates in this core range from 8 to12 cm/kyr making it ideally suited for study of the last deglaciation. Samples of ~10 mg of the thermocline dwelling planktonic foraminifera *Neogloboquadrina dutertrei* and 3-8 mg of mixed benthic species were measured for radiocarbon content at the University of California, Irvine Keck-Carbon Cycle AMS facility (Supplementary Table A.1 and Supplementary Figure A.1). Mixed genus benthic foraminiferal samples were necessary to assure sufficient material for radiocarbon analysis. Deep infaunal species (*Globobulimina spp., Chilostomella oolina*) that may bias the results towards younger calendar ages were avoided (Magana et al., 2010). The contemporary benthic-planktonic offset was calculated using bomb corrected $\Delta^{14}C$ from the Global Ocean Data Analysis Project (GLODAP) bottle data (Key et al., 2004), following de la Fuente et al. (2015). The modern ^{14}C ages were estimated from GLODAP $\Delta^{14}C$ using the equation from Stuiver and Polach (1977; ^{14}C age=-8033*ln(1+($D^{14}C$/1000)) modified for $\Delta^{14}C$.

1.5.2 Stratigraphic Alignment

In addition to the tuned age models, an age model was developed by applying a constant reservoir correction of 147±13 years to 31 *N. dutertrei* radiocarbon dates using the

Bayesian age-depth modeling program BACON (Blaauw and Christen, 2011). Oxygen isotope analyses were carried out on the planktonic foraminifera *G. ruber* (Supplementary Figure A.1) using an Elementar Isoprime stable isotope ratio mass spectrometer. Distinctive oxygen isotope events were visually identified in TR163-23 and matched to Northern Hemisphere reference events in the GRIP Greenland ice core on the Greenland Ice Core Chronology 05 (GICC05; Johnsen et al., 1997; Rasmussen et al., 2014; Seierstad et al., 2014) for the Greenland-tuned chronology and to the H82 and MSD Hulu speleothems (Wang et al., 2001; Wu et al., 2009; Southon et al., 2012) for the Hulu-tuned age model. Tuning the EEP to Northern Hemisphere climatic events is supported mechanistically by an atmospheric bridge across the Isthmus of Panama (Xie et al., 2008). During North Atlantic cold periods increased northeasterly winds across Panama drive decreased sea surface temperatures (SST) and shoaling of the thermocline resulting in an expansion of the equatorial cold tongue. The link between Northern Hemisphere climate change and the EEP has been recorded over the last 100 kyr by paleoclimate records of SST and sea surface salinity (Kienast et al., 2006; Leduc et al., 2007; Dubois et al., 2014).

1.5.3 Radiocarbon Plateau Tuning

Visually identified TR163-23 radiocarbon plateaus were matched to Lake Suigetsu atmospheric ^{14}C-plateaus (Sarnthein et al., 2015; Bronkk Ramsey et al., 2012) on the varve-derived Suigetsu age model consistent with published plateau-tuned age models (Balmer et al., 2016; Sarnthein et al., 2015). This chronology is preferable to the modeled chronology because it is independent of assumed limits on changes in the dead carbon fraction of U/Th dated Hulu and Bahama speleothems (Sarnthein et al., 2015).

Furthermore, the plateau tuned age model developed using the varve chronology provides a closer match to the Hulu speleothem and Greenland ice core tuned age models for TR163-23. The indistinct base of plateau 1a/top of plateau 1 was not included in the final plateau-tuned age model. Plateau tuning suggest the presence of a short hiatus between the Younger Dryas plateau and plateau 1a. The timing and length of the hiatus is estimated using the Bayesian age modeling program BACON (Blaauw and Christen, 2011) with the prior distribution for the hiatus modelled by a gamma distribution with a mean chronological time gap of 1000 years. Accumulation rates are assumed not to be auto-correlated between the depths just before and after the hiatus. However, inclusion of the hiatus has little effect on the final age model. The Elastic Tie Pointing method (Heaton et al., 2013) was used to transfer tie-point ages from the reference record to TR163-23. Larger matching uncertainty was applied to the glacial tie-points in each of the tuned records to allow for a lower level of certainty associated with event contemporaneity during this period. Because we did not have sufficient resolution to identify tie-points during the Holocene this portion of the chronology was constructed using 3 calibrated ($\Delta R=147\pm13$) *N. dutertrei* calendar ages for each of the tuned chronologies. Additionally, radiocarbon plateaus could not be identified in TR163-23 during the glacial period requiring the use of one Greenland tie-point to constrain this period. Tie-point errors determined using the ETP method (Heaton et al., 2013) and conventional radiocarbon ages were incorporated into the Bayesian age-depth modeling program BACON (Blaauw and Christen, 2011) to calibrate Holocene radiocarbon dates and to constrain the final age models and their uncertainty.

Table 1.1 Method of age model constraint for cited radiocarbon records.

Archive	region	Depth (m)	age constraint	Reference
TR163-23	Galapagos	2,730	Stratigraphic tie points (ice core $\delta^{18}O$ and ^{14}C plateaus)	This study
ODP1240	Panama Basin	2,921	Stratigraphic tie points (correlation of Mg/Ca and δ18O to Greenland ice core)	de la Fuente et al., 2015
coral transect	Equatorial Atlantic	750-2,100	Paired U/Th and ^{14}C ages	Chen et al., 2015
coral transect	Drake Passage	819-1,750	Paired U/Th and ^{14}C ages	Burke and Robinson, 2012
MD02-2489	Gulf of Alaska	3,640	Stratigraphic tie points (ice core δ18O)	Rae et al., 2014
MD99-2334k	NE Atlantic	3,146	Stratigraphic tie points (correlation of Mg/Ca and δ18O to Hulu cave speleothems)	Skinner et al., 2014
MD07-3076	Sub-Antarctic Atlantic	3,770	Stratigraphic tie points (Correlation of Mg/Ca to ice cores)	Skinner et al., 2010
Iceland core compilation	N Atlantic	1,237-2,303	Correlation of ash layers to dated terrestrial eruptions	Thornalley et al., 2011
coral compilation	NW Atlantic	1,713-2,590	Paired U/Th and ^{14}C ages	Robinson et al., 2005
MV99-MC19/GC31/PC08	E Pacific	705	Correlation of Diffuse Spectral Reflectance to GISP2 $\delta^{18}O$	Marchitto et al., 2007, Lindsay et al., 2015

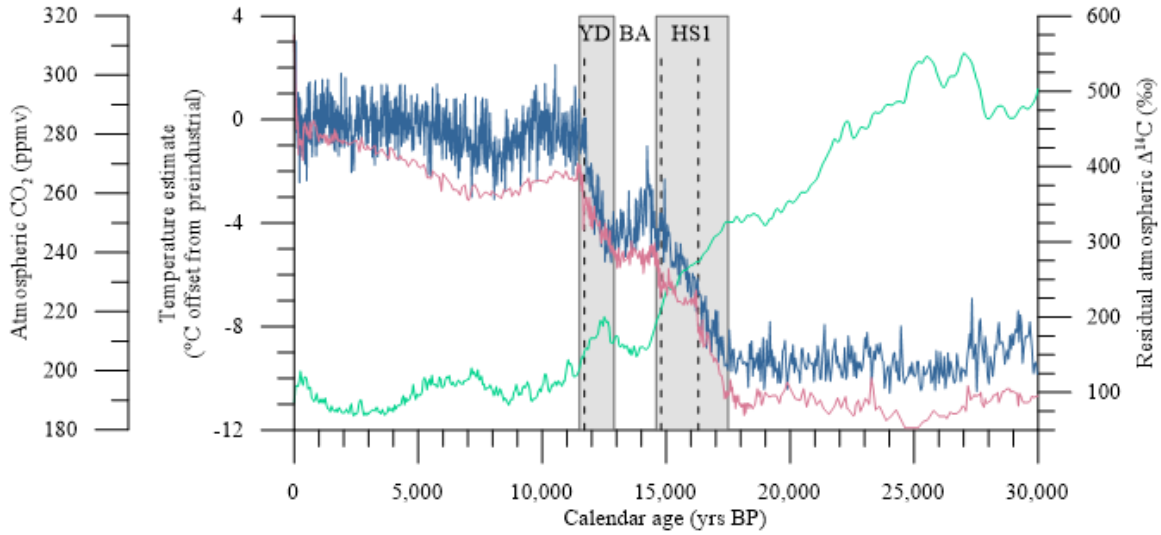

Figure 1.1. Atmospheric CO_2 and temperature changes across the last deglaciation. Both atmospheric CO_2 from a composite record of Antarctic ice cores (blue) (Bereiter et al., 2015) and Antarctic temperature change recorded by the Epica Dome C ice core (pink) (Parrenin et al., 2013) show a two-step increase through the deglaciation. Increasing Atmospheric temperature and CO_2 during Heinrich Stadial 1 (HS1) and the Younger Dryas (YD) is separated by a period of little to no change during the Bølling Allerød (BA). Atmospheric radiocarbon content ($\Delta^{14}C$ corrected for natural production; green; Hain et al., 2014) decreases over the same period. Dashed lines indicate century long periods of abrupt CO_2 rise identified by Marcott et al. (2014).

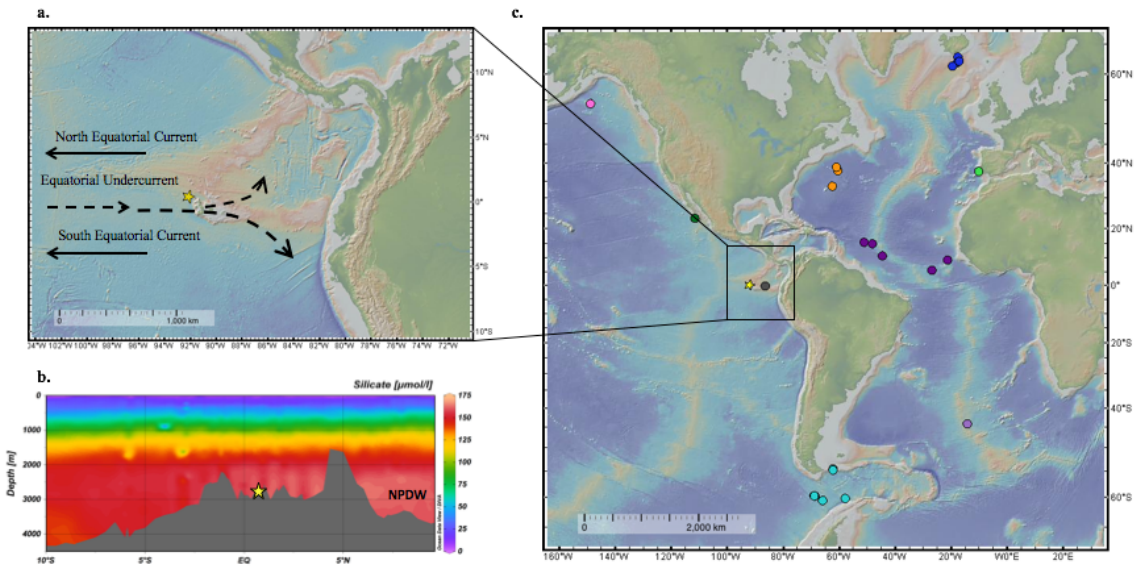

Figure 1.2 Core locations and study area. (**a**) Location of TR163-23 (0.41°N, 92.16°W; 2730 m water depth) with the main bathymetric features and important currents of this region. (**b**) A cross-section of silicate concentrations along 88°W generated using Ocean Data View software (Schlitzer, 2015); the location of TR163-23 is within the North Pacific Deep Water silicate maximum (Tsuchiya and Talley, 1998; Key et al., 2004). (**c**) The location of marine records displayed in Figure 1.7 including TR163-23 (this study) shown with a star, ODP1240 (0.01°N, 86.46°W; 2,921 m; de la Fuente et al., 2015) in grey, MD02-2489 (54.39°N, 148.92°W; 3,640 m; Rae et al., 2014) in pink, MV99-MC19/GC31/PC08 (23.47° N, 111.6°W; 705 m; Marchitto et al., 2007; Lindsay et al., 2015) in dark green, Drake Passage corals (Burke and Robinson, 2012) in light blue, MD07-3076 (44.07°S, 14.21°W; 3,770 m; Skinner et al., 2010) in light purple, a transect of S. Iceland cores (1200-2300 m; Thornalley et al., 2011) in dark blue, northwest Atlantic corals (Robinson et al., 2004) in orange, equatorial Atlantic corals (Chen et al., 2015) in dark purple, and eastern North Atlantic core MD99-2334k (37.8°N, 10.17°W; 3,146 m; Skinner et al., 2014) in light green.

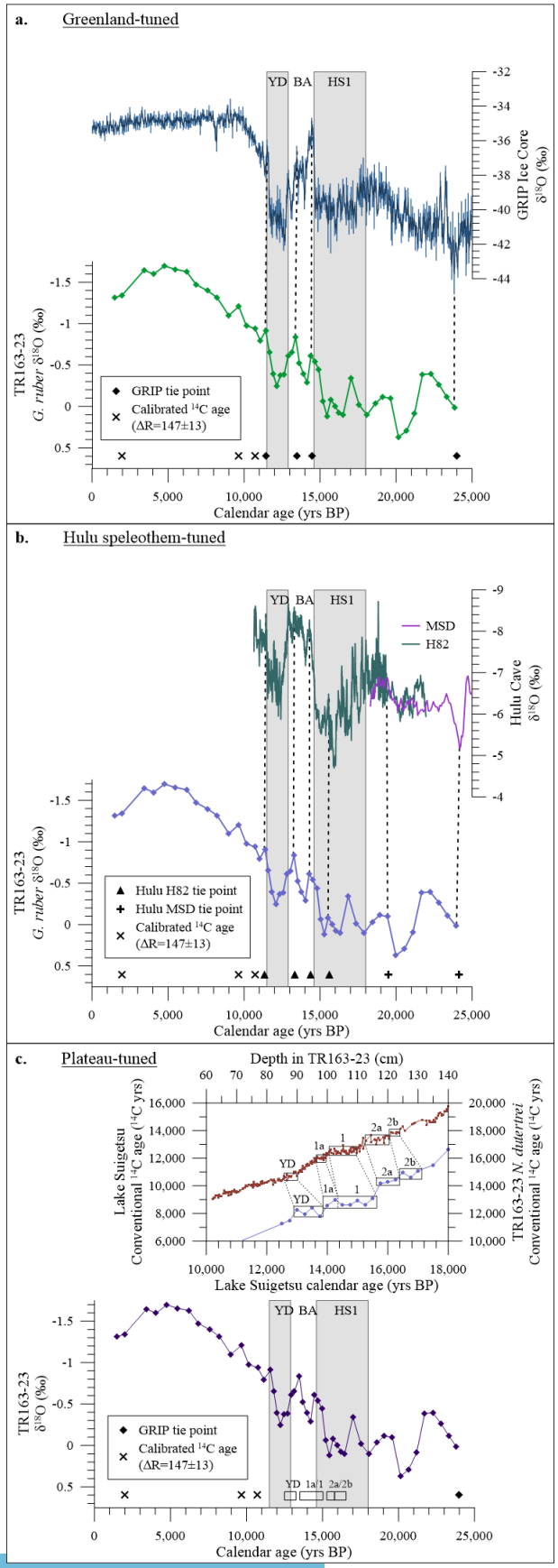

Figure 1.3 Construction of TR163-23 tuned chronologies. **(a)** Tie point ages and age uncertainty for the TR163-23 *Globigerinoides ruber* $\delta^{18}O$ record were constrained from the GRIP ice core $\delta^{18}O$ record (Johnsen et al., 1997; Rasmussen et al., 2014; Seierstad et al., 2014) using Elastic Tie-Pointing (ETP; Heaton et al., 2013). Calibrated radiocarbon ages used in the final age model are indicated with an X and ETP derived tie points are indicated with a diamond. **(b)** ETP constrained deglacial tie-points from the H82 speleothem and glacial tie-points from the MSD speleothem $\delta^{18}O$ records (Wang et al., 2001; Wu et al., 2009; Southon et al., 2012) are indicated by a triangle. As with the Greenland-tuned age model, calibrated radiocarbon ages are used to date the Holocene portion of the core in the final Bayesian-derived age model. Dashed lines connect TR163-23 $\delta^{18}O$ data points to corresponding Hulu speleothem and Greenland ice core reference record events used as tie points. **(c)** Five ^{14}C-plateaus were identified in the TR163-23 *N. dutertrei* radiocarbon record that correspond to ^{14}C-plateaus previously identified in the Lake Suigetsu atmospheric ^{14}C record (Bronk Ramsey et al., 2012) by Sarnthein et al. (2015). A hiatus between the Younger Dryas plateau and plateau 1a was included in the final Bayesian-derived age model. Additionally, a Greenland ice core tie point was used to constrain the LGM portion of the core.

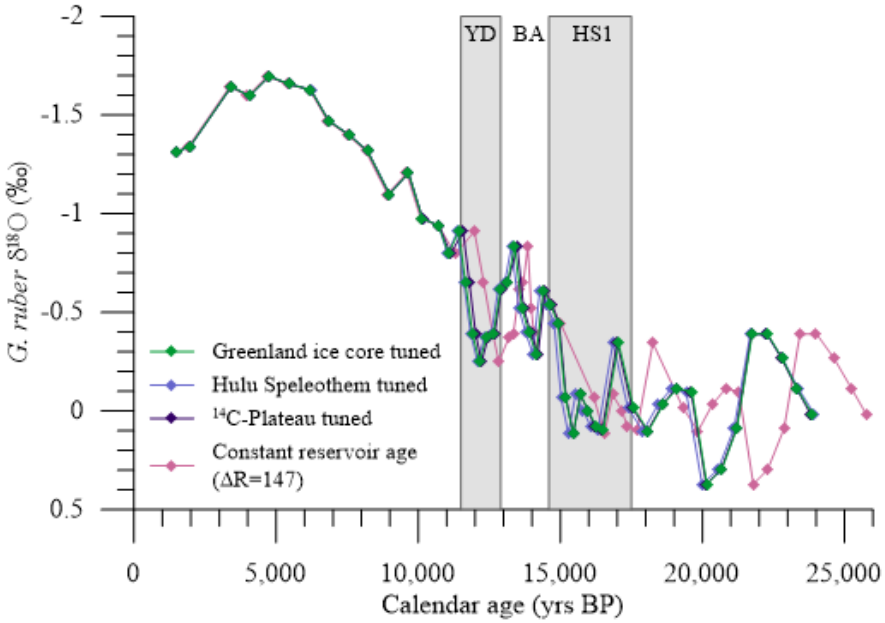

Figure 1.4 Comparison of age model techniques. The three tuned age models yield results that are indistinguishable from one another within 1σ error windows. In contrast, the calibration of TR163-23 *N. dutertrei* ^{14}C-ages using a constant reservoir correction (ΔR=147±13) results in chronological offsets of up to ~2,000 yrs from the tuned age models.

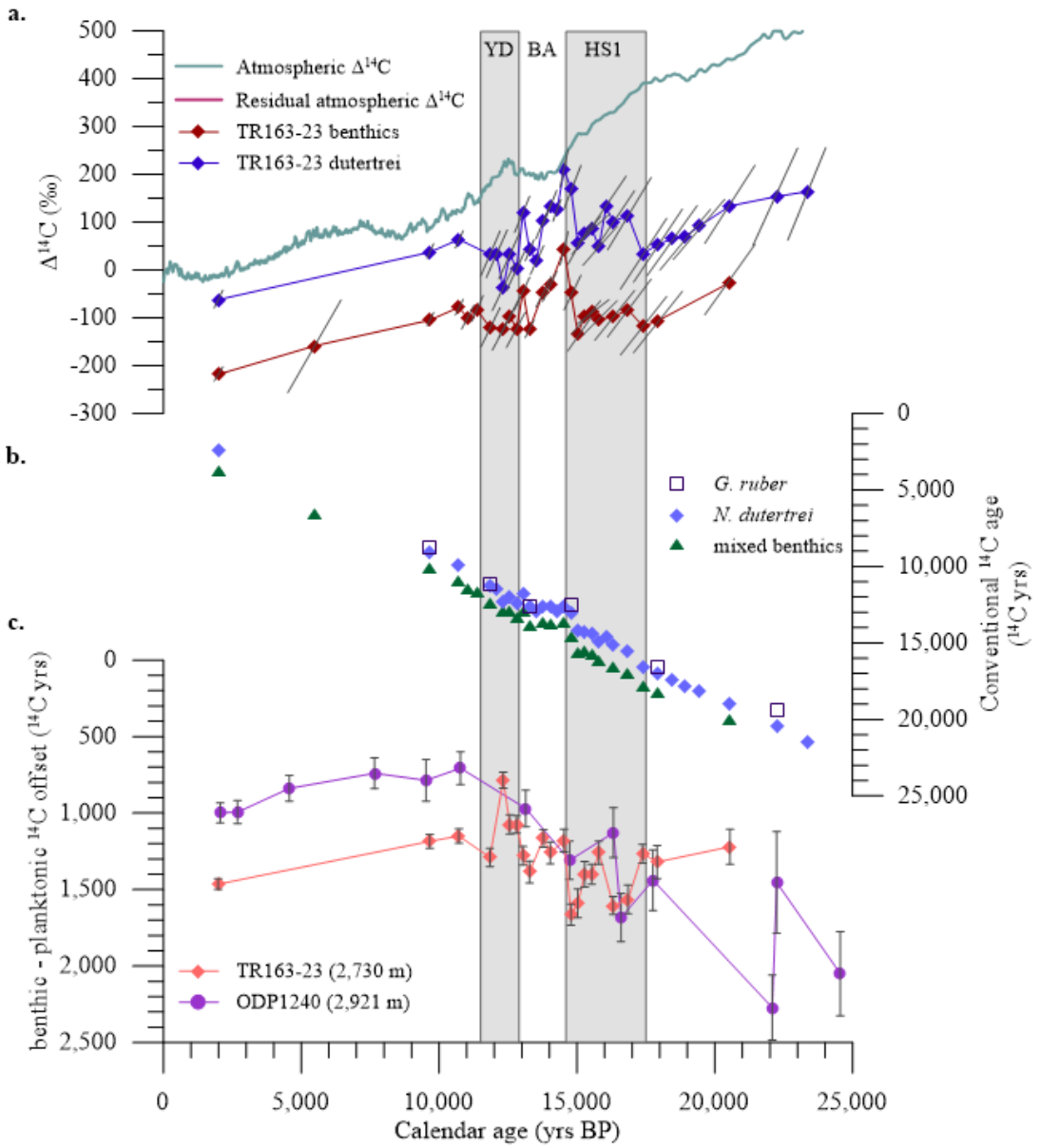

Figure 1.5 Radiocarbon records for TR163-23. **(a)** TR163-23 benthic and planktonic $\Delta^{14}C_0$ and atmospheric records of $\Delta^{14}C$. The residual atmospheric $\Delta^{14}C$ has been corrected for modeled cosmogenic ^{14}C production (Hain et al., 2014). Benthic and planktonic $\Delta^{14}C_0$ remains relatively constant through deglaciation except for a rapid increase at the end of HS1 and at the end of the BA. The major axis of 1σ error ellipses is plotted for benthic and planktonic $\Delta^{14}C_0$. **(b)** Conventional radiocarbon ages measured from 31 *Neogloboquadrina dutertrei*, 3 *Globogerinoides ruber*, and 25 mixed benthic samples. Deglacial *G. ruber* and *N.* dutertrei samples show negligible ^{14}C offsets. **(c)** Benthic-planktonic ^{14}C offsets in Galapagos core TR163-23 and Panama Basin core ODP 1240 (de la Fuente et al., 2015) indicate similar offsets during the deglacial period. Although TR163-23 B-P offsets show little overall change from the LGM to the Holocene, ODP 1240 suggests a trend of decreasing B-P offsets during this period. One sigma error bars are plotted for B-P offsets.

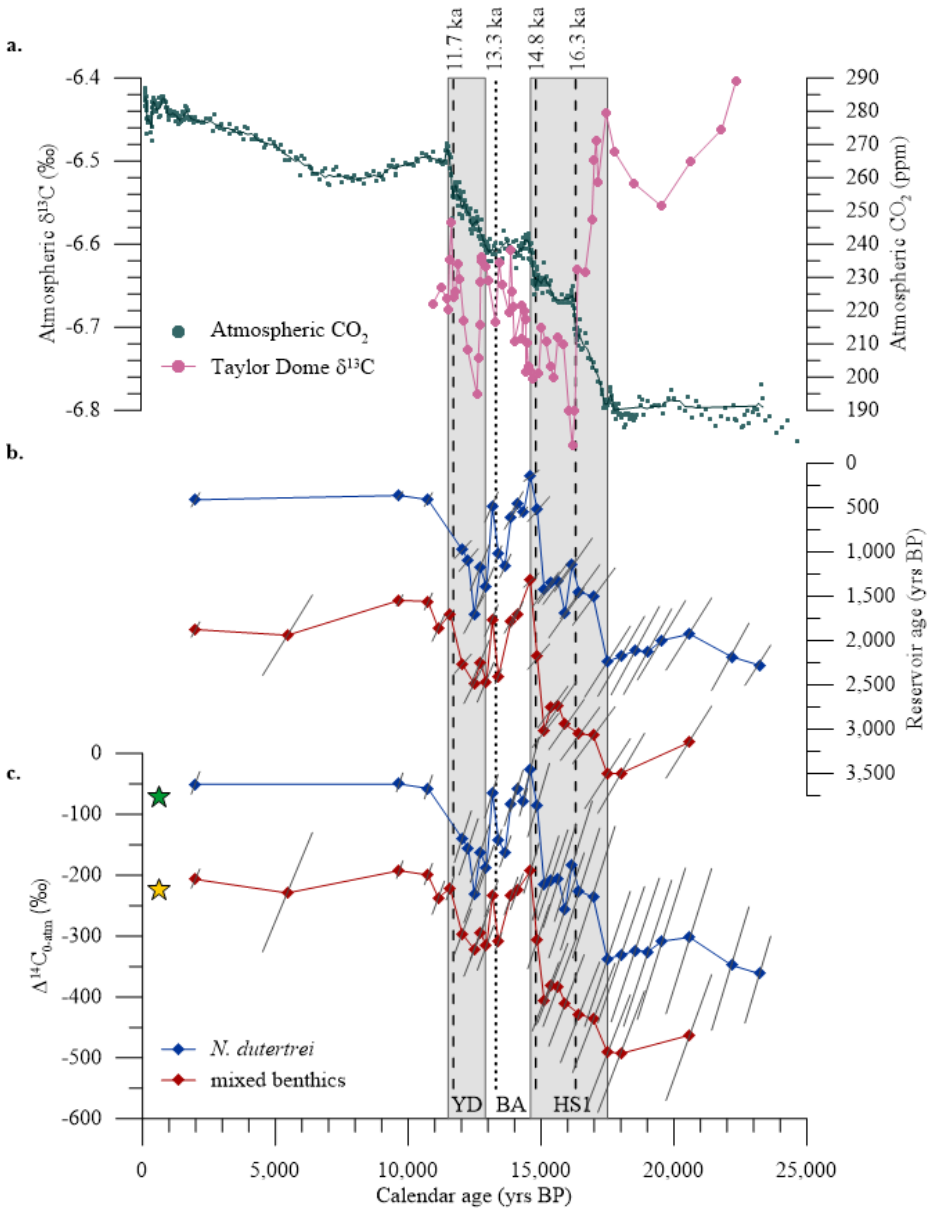

Figure 1.6 Foraminifera radiocarbon offsets from the atmosphere over the last 25,000 years. **(a)** Composite atmospheric [CO_2] record from Antarctic ice cores (Bereiter et al., 2015) and $\delta^{13}C$ from Taylor Glacier, Antarctica (Bauska et al., 2016). **(b** and **c)** Reconstructed radiocarbon offsets from the atmosphere displayed in calendar years and as $\Delta^{14}C_{0\text{-atm}}$ with the major axis of 1σ error ellipses displayed. Contemporary $\Delta^{14}C$ from GLODAP (Key et al., 2004) is shown for thermocline depths (green star, -85‰) and for 2.7 km (yellow star, -220‰). Three centennial increases in the WDC atmospheric CO_2 record occur at 16.3, 14.8, and 11.7 ka (dashed line; Marcott et al., 2014). There is an EEP equivalent at both thermocline and deep water-depths for the 14.8 ka event, while a possible 16.3 ka event corresponds with only an increase in thermocline ventilation. Our records do not have sufficient resolution at 11.7 ka to capture ventilation changes associated with this century-long CO_2 increases. An additional ventilation event is recorded in TR163-23 in the late BA (dotted line).

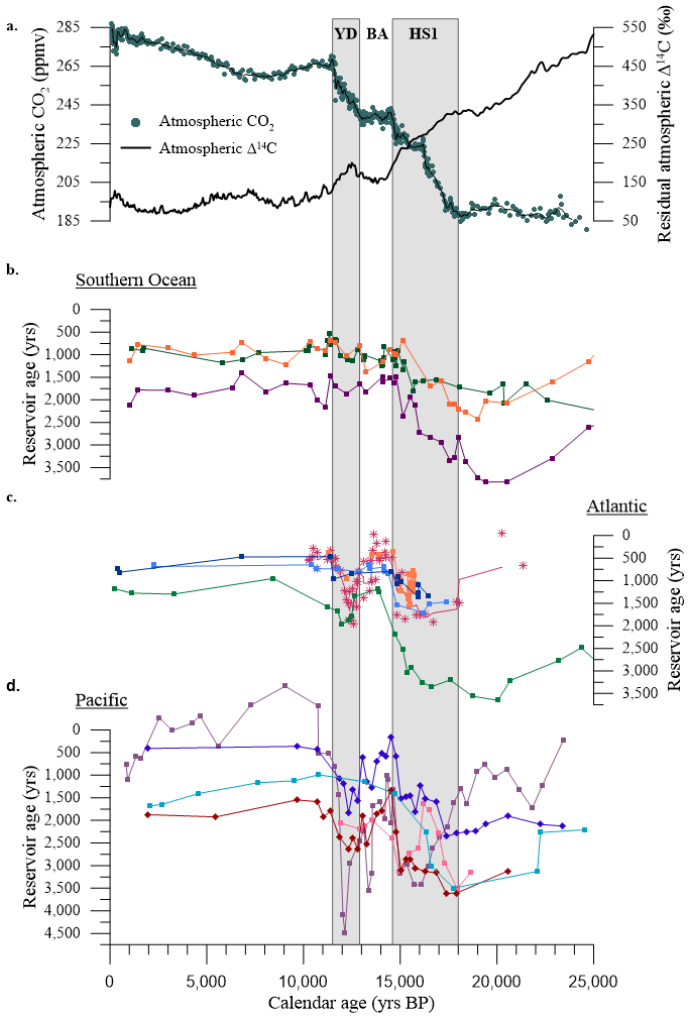

Figure 1.7 Interocean comparison of shallow and deep water ventilation. **(a)** An Antarctic ice core compilation of Atmospheric CO_2 (Bereiter et al., 2015) indicates increasing CO_2 during the deglacial coeval with declining Atmospheric $\Delta^{14}C$ (corrected for natural production; Hain et al., 2014; Marcott et al., 2014). **(b)** Southern Ocean records include surface (dark-orange) and deep (3,770 m; dark-purple) water-depths from core MD07-3076 (Skinner et al., 2010) in the sub-Antarctic South Atlantic along with a Drake Passage coral compilation from Upper Circumpolar Deep Water (dark-green; Burke and Robinson, 2012). **(c)** Atlantic records include deep-water core MD99-2334k (3,146 m; green; Skinner et al., 2014) in the eastern Atlantic, a transect of cores off the southern coast of Iceland (1,237-2,303 m; magenta; Thornalley et al., 2011), a coral compilation from the NW Atlantic (819-1,750 m; orange; Robinson et al., 2005), along with intermediate (1,296-1,492 m; navy-blue) and deep (1,827-2,100 m; light-blue) water-depth equatorial Atlantic coral compilations (Chen et al., 2015). **(d)** Pacific records include thermocline (dark-blue) and deep (2,730 m; red) water-depths from EEP core TR163-23 (this study), deep-water Panama Basin core ODP1240 (2,921 m; cyan; de la Fuente et al., 2015), deep-water Gulf of Alaska core MD02-2489 (3,640 m; pink; Rae et al., 2014), and intermediate depth Eastern Pacific core MV99-MC19/GC31/PC08 (705 m; purple; Marchitto et al., 2007; Lindsay et al., 2015).

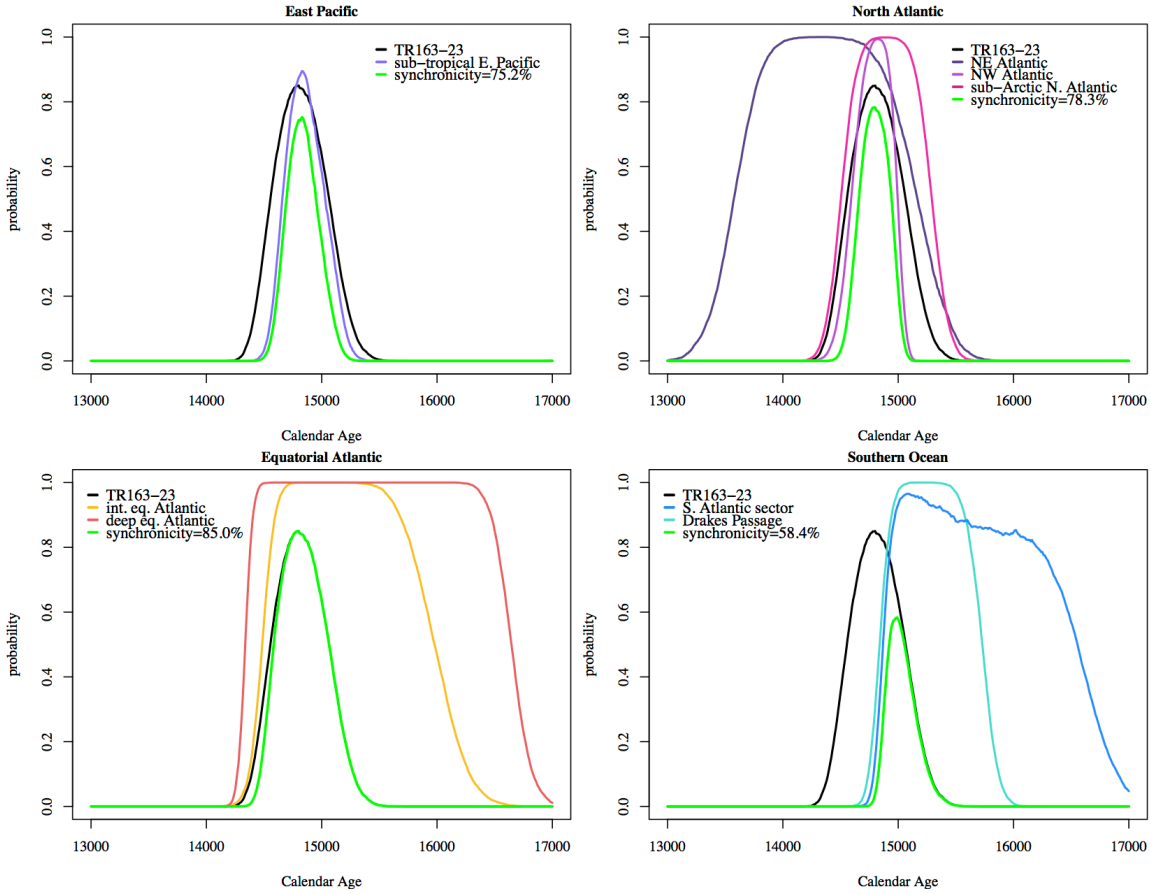

Figure 1.8 Inter-ocean synchronicity of the 14.8 ka ventilation event. The Bayesian age modeling program BACON (Blaauw and Christen, 2011) was used to resample reported chronologies along a uniform time interval and to calculate the probability of the 14.8 ka ventilation event occurring at each study site from 13.0-17.0 ka using a 100 year window with a 10 year time step (Blaauw et al., 2007). Incorporating age uncertainties, event probabilities were combined to test for synchronicity. The width of an individual probability curve is determined both by event length and age model uncertainty whereas the height is a function of age model certainty alone; e.g. a narrow curve with peak probability close to 1.0 corresponds to a brief, well-defined event. Our EEP record is synchronous with the other **a)** East Pacific (72.3%), and **b)** North Atlantic (78.0%) records within 1σ (68.27%). **c)** The 14.8 ka event in equatorial Atlantic records ends at a similar time as the EEP, however this region has insufficient resolution at the onset of this event to determine whether the 14.8 ka event was indeed simultaneous with the EEP. **d)** Southern Ocean records suggest an earlier ventilation event with less likelihood of synchronicity (48.7%) at 14.8 ka.

CHAPTER 2

MID-DEPTH RESPIRED CARBON STORAGE AND OXYGENATION OF THE EASTERN EQUATORIAL PACIFIC OVER THE LAST 25,000 YEARS [2]

[2] Umling, N.E., Thunell, R.C. Submitted to *Earth and Planetary Science Letters* 06/07/17.

2.1 Abstract

A growing body of evidence suggests that respired carbon was stored in mid-depth waters during the last glacial maximum (LGM) and released to the atmosphere from upwelling regions during deglaciation. A more efficient biological pump has been cited as a possible mechanism for increased nutrient and CO_2 concentrations at depth during the LGM, while a less efficient biological pump may have contributed to CO_2 evasion to the atmosphere during deglaciation. An increase in glacial mid-depth water respired carbon storage should result in a shift of DIC speciation towards lower carbonate ion concentrations, along with deoxygenation of bottom waters. In this study, we use the boron to calcium (B/Ca) ratios of the benthic foraminifera *Cibicidoides wuellerstorfi* to reconstruct deep-water carbonate ion concentrations. Additionally, bottom water oxygenation is estimated from the difference in $\delta^{13}C$ of infaunal benthic foraminifera living in pore waters at the anoxic boundary and of epifaunal species living in bottom water. Our records indicate that oxygenation of the mid-depth Eastern Equatorial Pacific increased through deglaciation by 80 μmol kg^{-1} and that carbonate ion concentrations were significantly lower during the Younger Dryas and Heinrich Stadial 1 cold periods relative to the Holocene. These results suggest that Eastern Equatorial Pacific mid-depth waters stored respired carbon during the LGM releasing it to the atmosphere during deglaciation, consistent with a deglacial reinvigoration of overturning circulation.

2.2 Introduction

The last deglaciation provides important insights into the nature of climate changes during the transition from glacial to interglacial conditions. Specifically, this transition is punctuated by brief periods of rapid return to cold, glacial-like conditions

followed by abrupt warmings (Shakun et al., 2012). These cold periods are accompanied by gradually increasing atmospheric CO_2, ~50 ppmv during late Heinrich Stadial 1 (HS1; ~17.5-14.7 ka) and ~30 ppmv during the Younger Dryas (YD; ~12.8-11.5 ka) (Monnin et al., 2001), overprinted by periods of rapid (100-200 yrs) CO_2 increase at 11.7 ka, 14.8 ka, 16.3 ka (Marcott et al., 2014) (Figure 2.1). The deep and intermediate ocean is thought to be a major contributor to the rise in atmospheric CO_2 during the last deglaciation. Recent radiocarbon evidence suggests that ventilation of mid-depth waters was reduced during the last glacial maximum (LGM; Burke et al., 2015; Ronge et al., 2016; Umling and Thunell, 2017), allowing respired carbon to accumulate before being subsequently released to the atmosphere from upwelling regions such as the Eastern Equatorial Pacific (EEP) during deglaciation (de la Fuente et al., 2015; Martínez-Botí et al., 2015; Umling and Thunell, 2017). However, alternate mechanisms have been suggested to drive the atmospheric CO_2 excursions of the last 25,000 years (Broecker and Peng, 1987; Jaccard et al., 2009; Köhler et al., 2014; Martínez-García et al., 2014, Matsumoto et al., 2002).

It has been hypothesized that a less efficient biological pump during periods of enhanced oceanic circulation could have been responsible for the deglacial CO_2 increases (Ziegler et al., 2013), whereas more efficient sequestration of respired carbon from the surface ocean to deeper waters during periods of reduced circulation may have contributed to lower glacial atmospheric CO_2 concentrations (Jaccard et al., 2009). Benthic and planktonic foraminiferal $\delta^{13}C$ records suggest that the surface to deep-water carbon isotope gradient was lower during HS1 and the YD, when Atlantic Meridional Overturning Circulation (AMOC) was reduced (Hertzberg et al., 2016). This implies that surface-water preformed nutrients were being increasingly under-utilized, reducing the

amount of carbon exported to deep waters and allowing enhanced CO_2 evasion to the atmosphere (Hertzberg et al., 2016). However, the contribution of CO_2 from decreased biological pump efficiency alone, is not of sufficient magnitude to account for the total deglacial atmospheric CO_2 increase. Permafrost thawing (Köhler et al., 2014), carbonate compensation (Broecker and Peng, 1987), and enhanced deep-water ventilation (Broecker and Barker, 2007) have also been suggested as complementary mechanisms for driving CO_2 increases. The atmospheric carbon isotopic composition recorded in ice cores suggests that the release of terrestrial carbon may have been important during rapid (100-200 years) CO_2 increases at 16.3 and 12.9 kyr (Bauska et al., 2016). However, rising ocean temperatures and a less efficient biological pump likely drove much of the millennial and some of the centennial-scale CO_2 changes (Bauska et al., 2016). Because the efficiency of the biological pump is modified, in part, by changes in oceanic ventilation, a coupling of these two processes could account for the full deglacial CO^2 increase.

Evidence of coeval shifts in ventilation and respired carbon export in Sub-Antarctic Atlantic deep-waters hint that the biological pump and ocean circulation likely worked in tandem to modify atmospheric CO_2 concentrations during the last glacial period (Gottschalk et al., 2016). However, it is not yet apparent whether this relationship is limited to glacial Circumpolar Deep Waters (CDW) or whether it is regionally more extensive. Qualitative estimates of intermediate and deep-water oxygen content suggest large spatial and depth-dependent differences in oxygenation between the LGM and Holocene (Jaccard and Galbraith, 2011), but the deglacial variability is not as well constrained. Here, we present multi-proxy records of mid-depth and deep-water

chemistry for the Eastern Equatorial Pacific over the last 25,000 years to investigate the linkages between respired carbon storage and ocean ventilation during the last glacial-interglacial transition. Additionally, we evaluate regional trends in respired carbon variability by compiling published records of deep and intermediate water carbonate chemistry from benthic foraminiferal boron to calcium ratios.

2.3 Sample Material and Oceanographic Setting

This study utilizes a series of cores collected from the Panama Basin during R/V Trident cruise TR-163 (Figure 2.2, Table 2.1). For a detailed analysis of the deglaciation we focus on core TR163-23 (0°24.6'N, 92°9.6'W) collected from 2,730 m water-depth off the Galapagos platform. Five additional cores from the Cocos and Carnegie Ridges in the Panama Basin were used to evaluate depth dependent changes in mid-depth and deep water properties during three time periods: LGM, Bolling-Alerod (B-A), and Holocene. The Panama Basin is an important region for study of the biological pump because it is responsible for ~10% of global ocean primary productivity and is strongly connected to the Southern Ocean (Pennington et al., 2006). Primary productivity in this region is controlled by upwelling strength, thermocline depth, and supply of nutrients to the thermocline (Pennington et al., 2006). In particular, upwelling of the Equatorial Undercurrent (EUC) is an important source of nutrients and CO_2 to surface waters (Fiedler and Talley, 2006). At present, the Panama Basin serves as a major site for the efflux of CO_2 from the surface ocean to the atmosphere (Takahashi et al., 2002).
Deep and mid-depth waters of the EEP are composed of Lower Circumpolar Deep Water (LCDW) at abyssal depths and Pacific Deep Water at depths of ~1,000-3,200 m. LCDW is formed from mixing of Antarctic Bottom Water (AABW) and North Atlantic Deep

Water (NADW) in the Southern Ocean (Fiedler and Talley, 2006). The warming and freshening of LCDW forms PDW at mid-depths; these waters are characterized by a silica maximum at ~2,500-3,200 m, overlain by waters with low oxygen and silica concentrations but overall higher concentrations of nutrients than found within mid-depth waters (Fiedler and Talley, 2006).

2.4 Methods

2.4.1 Age Model Development

The age model for TR163-23 was developed using a combination of radiocarbon dating and tuning of the oxygen isotope record from the planktonic foraminifera species *Globogerinoides ruber* to the Hulu Cave Speleothem $\delta^{18}O$ record (Southon et al., 2012; Wang et al., 2001; Wu et al., 2009). *Globigerinoides ruber* oxygen isotope events were visually identified in TR163-23 and matched to reference events in the U/Th dated Hulu Cave Speleothem (Southon et al., 2012; Wang et al., 2001; Wu et al., 2009). For estimation of tie-point uncertainty, the Hulu speleothem reference chronology was translated to TR163-23 using the elastic tie-point method developed by Heaton et al. (2013). Larger matching uncertainty was applied to the glacial tie-points to allow for a lower level of certainty associated with event contemporaneity during this period. Three samples of ~10 mg of the planktonic foraminifera *Neogloboquadrina dutertrei* were measured for radiocarbon content at the University of California, Irvine Keck-Carbon Cycle AMS facility and used to date the Holocene portion of the core (Figure 2.3). The Bayesian age-depth modeling program BACON (Blaauw and Christen, 2011) was used to calibrate the *N. dutertrei* radiocarbon ages ($\Delta R=147\pm13$) and to construct the final age model. This Bayesian method incorporates age model uncertainty associated with

calibration of the radiocarbon ages and tie-point uncertainty for constraint of the final age model and its associated uncertainty. A more detailed description of the age model construction for TR163-23 can be found in Umling and Thunell (2017). TR163-23 reservoir ages estimated from this method (Supplementary Table B2) were used with BACON to calibrate *N. dutertrei* radiocarbon ages from each of the TR163 cores (Figure 2.3) used in this study and to develop chronologies for each of the cores.

2.4.2 Estimation of Bottom Water Carbonate Chemistry

Approximately 10 *Cibicidoides wuellerstorfi* of consistent morphology (Rae et al., 2011) were picked from the 250-425 μm size fraction of each core sample for trace element analyses. When limited material was available, additional *C. wuellerstorfi* were picked from the 212-250 μm size fraction. Samples were cleaned in over-pressured flow hoods equipped with boron-free HEPA filters following the Cd-cleaning protocol from Boyle and Keigwin (1985/86) as modified by Boyle and Rosenthal (1996) using the minimal settling technique from Barker et al. (2003) and analyzed on a Thermo Element II high resolution ICP-MS. To increase boron washout efficiency and reduce boron memory effects in the sample introduction system we used a HF-HNO_3 sample matrix (0.06 M HF and 0.1 M HNO_3) following Misra et al. (2014). Multi-element standard solutions were prepared gravimetrically using high purity mono-element standards. Samples were dissolved in 100 μl of 0.2% Teflon-distilled HNO_3. For each sample run, calcium concentrations were measured from an aliquot of each sample solution and both sample and standard solutions were diluted accordingly to 20 ppm Ca using the HF-HNO_3 matrix. Samples were introduced using a Teflon barrel spray chamber and

platinum injector. The analytical error for B/Ca is ± 1.4 μmol mol^{-1} (± 0.9%) based on repeated measurements of a standard of ~175 μmol mol^{-1}.

The global core top calibration from Yu et al. (2013) was used to estimate deep water carbonate saturation state ($\Delta[CO_3^{2-}]$) from B/Ca values (Eq. 2.1) and carbonate ion values were estimated according to Equation 2.2. The $[CO_3^{2-}]_{sat}$ was calculated from preindustrial $[CO_3^{2-}]$ estimated from nearby GLODAP stations (Key et al., 2004) using CO2SYS (Pelletier et al., 2005) with K1 and K2 of Mehrbach et al. (1973) refit by Dickson and Millero (1987), KSO_4 of Dickson (1990), and the boron-salinity relationship of Lee et al. (2010).

$$B/Ca = 1.14 \pm 0.04 * \Delta[CO_3^{2-}] + 176.6 \pm 1.0 \quad \text{(Eq. 2.1)}$$

$$\Delta[CO_3^{2-}] = [CO_3^{2-}]_{in\ situ} - [CO_3^{2-}]_{sat} \quad \text{(Eq. 2.2)}$$

We monitored Al-silicate and oxide contamination through concurrent analysis of diagenetic indicators Fe/Ca, Mn/Ca, and Al/Ca. Generally, Fe/Ca ratios in the TR163 cores were below ~100 μmol mol^{-1}but, measured Al/Ca and Mn/Ca ratios were commonly elevated with the lowest median Al/Ca occurring in cores TR163-20B and TR163-18 which had generally the highest median Mn/Ca (Supplementary Fig. B1). Despite the elevated Mn and Al, there was no significant correlation with B/Ca and any of the diagenetic indicators (Supplementary Fig. B2).

2.4.3 Bottom Water Oxygen Estimates

The redox sensitive element uranium accumulates in sediments when bottom water oxygenation is low and/or there is high flux of organic carbon to the seafloor (McManus et al., 2005). This signal is recorded in the authigenic coating of bulk sediments (McManus et al., 2005). Additionally, foraminiferal coatings have been shown

to faithfully record the bulk sedimentary authigenic uranium (U_a) signal (Boiteau et al., 2012) and have the advantage of not requiring a correction for non-authigenic sedimentary uranium. We measured the U/Ca ratio on samples of ~10 *N.* dutertrei picked from the 300-425 μm size fraction for each of the cores. Samples were cleaned using alternating water and methanol rinses to preserve authigenic coatings. Foraminiferal intra-shell U/Ca has a negligible contribution towards total U_a and can be disregarded (Boiteau et al., 2012). *Neogloboquadrina dutertrei* U_a was corrected for changes in shell thickness and size by normalizing to manganese concentrations (U/Mn; Gottschalk et al., 2016). Authigenic uranium concentrations were also measured on 50 mg samples of lightly-cleaned, mixed planktonic foraminifera from the >355 μg size fraction. Both the bulk planktonic samples and the *N. dutertrei* samples were and analyzed on a Thermo Element II high resolution ICP-MS. The analytical error for the *N. dutertrei* U/Ca is ± 2.08 nmol mol^{-1} (± 2.6%) based on repeated measurements of an internal standard of ~79 nmol mol^{-1}. An isotopic spike was used to monitor analytical drift during the measurement of bulk planktonic foraminifera samples along with repeated measures of the USGS rock standard BHVO-2. Bulk planktonic foraminifera uranium concentrations were normalized to manganese concentrations. Measurements of both *N. dutertrei* and bulk planktonic samples from TR163-20B reveal that although the overall magnitude of authigenic uranium was different, the recorded glacial-interglacial U_a pattern is consistent regardless of which analytical method was used.

Bottom water oxygen content was reconstructed using the benthic foraminiferal $\Delta\delta^{13}C$ proxy of Hoogakker et al. (2014). This proxy exploits the relationship between organic carbon remineralization and pore-water oxygen concentrations. Specifically, the

depth of the oxic-anoxic boundary in sediments is related to both the amount of oxygen consumed from organic carbon remineralization and to overlying bottom water oxygen concentrations. The carbon isotope gradient from bottom waters to the sedimentary oxic-anoxic boundary corresponds to the amount of organic matter remineralized and the benthic foraminiferal $\delta^{13}C$ gradient can used to calculate bottom-water oxygen concentrations (McCorkle and Emerson, 1988). Bottom water $\delta^{13}C$ was estimated from the $\delta^{13}C$ of the epifaunal benthic formainifera *C. wuellerstorfi.* This species has an elevated microhabitat and secretes its calcite in a 1:1 relationship with bottom water $\delta^{13}C$ (Mackensen, 2008). The carbon isotope value at the oxic-anoxic boundary was determined from the $\delta^{13}C$ value recorded by the deep infaunal benthic foraminifera *Globobulimina* spp. which thrives at the sedimentary dysoxic-anoxic boundary and will migrate within the sediment following this boundary (McCorkle et al., 1990). Shallow infaunal species *Uvigerina* spp. and intermediate infaunal species *Chilostomella oolina* also were measured in conjunction with *C. wuellerstorfi* and *Globobulimina* spp. to approximate changes in the sedimentary $\delta^{13}C$ gradient.

2.5 Results

2.5.1 Eastern Equatorial Pacific Mid-Depth Oxygenation

Carbon isotopes from epifaunal species *C. wuellerstorfi* and shallow infaunal species *Uvigerina* spp. generally increase by ~0.5‰ from the LGM to the Holocene (Figure 2.4), similar to the estimated mean change in Pacific bottom water $\delta^{13}C$ over this time period (Curry et al., 1988), suggesting that it is unlikely that TR163-23 was influenced by a photodetrital effect associated with high productivity (Mackensen et al., 1993). The most negative $\delta^{13}C$ values (-2.5 to -2.8‰) were recorded by the intermediate

infaunal species, *Chilostomella oolina* (Figure 2.4). Although *C. oolina* was not present in sufficient numbers for isotopic analyses throughout the entire core, this species does record a similar $\delta^{13}C$ increase from the Bolling Allerod (BA) to the Holocene. Conversely, $\delta^{13}C$ from deep-dwelling *Globobulimina* spp. does not change significantly during the last deglaciation (Figure 2.4). The quantitative $\Delta\delta^{13}C$ estimates of $[O_2]$ reveal that mid-depth waters off the Galapagos remained well-oxygenated ($[O_2] > 80$ μmol/kg) throughout the glacial-interglacial transition, with oxygen concentrations gradually increasing by 60-80 μmol kg^{-1} from the LGM to the Holocene (Figure 2.4). This is supported by the generally low glacial and Holocene accumulations of authigenic uranium in TR163-23 (Figure 2.5). The exception to this is a period of enhanced U_a accumulation during the late deglacial Younger Dryas (Figure 2.5). $\Delta\delta^{13}C$ estimates of $[O_2]$ decrease in association with this YD increase in U_a, however, the oxygen concentrations do not return to the lower values seen during the LGM and HS1 (Figure 2.4). Records of authigenic uranium from nearby TR163 cores demonstrate that this late deglacial maximum in U_a was replicated in nearby core TR163-20B whereas Carnegie and Cocos Ridge cores TR163-14 and TR163-25 record a HS1/LGM maximum in authigenic uranium accumulation along with overall higher concentrations of U_a (Figure 2.5).

2.5.2 Glacial-Interglacial Carbonate Ion Variability

Over the last 25,000 years, *C. wuellerstorfi* B/Ca values for TR163-23 ranged from ~175 to ~215 μmol mol^{-1} in EEP mid-depth waters, although there is no significant difference in B/Ca values between the last glacial period and the Holocene (Figure 2.6). There are however, two distinct changes in B/Ca during deglaciation. The first is an

increase from 180 to 215 μmol mol^{-1} during HS1, followed by a decrease of similar magnitude from the BA into the YD (Figure 2.6). This range of B/Ca values equates to a range in [CO_3^{2-}] of ~ 70 to 105 μmol kg^{-1} (Figure 2.6), which is five to six times higher than the ~15 μmol kg^{-1}change recorded in mid-depth Western Equatorial Pacific cores (Yu et al., 2013). The mid-deglacial maximum in Δ[CO_3^{2-}] at ~14-15 ka in cores TR163-23 and TR163-14 is similar to that recorded in the two shallowest cores (TR163-18 and TR163-2) almost 2,000 years later at ~13 ka. However, this apparent difference in timing may be an artifact of the low sedimentation rates in these cores (2-4 cm/kyr). Conversely, there may be a depth-dependent lag in the timing of the deglacial Δ[CO_3^{2-}] maximum recorded by the two cores at depths of ~2 km and bellow. Results from TR163-25 and TR163-20B are more variable and do not demonstrate a clear mid-deglacial maximum. Rather, these cores suggest a slight overall increase in Δ[CO_3^{2-}] from the LGM to the Holocene. The location of TR163-25 on the Carnegie Ridge saddle could contribute to the higher variability in the recorded Δ[CO_3^{2-}], with modified deep-water from within the basin mixing with waters sourced from outside the basin. Conversely, TR163-20B is located close to the boundary between younger, northward flowing LCDW and old, southward flowing PDW. A shoaling of this boundary during the glacial-interglacial transition would shift the saturation state at the depth of TR163-20B towards higher values, overprinting changes in saturation state related to enhanced DIC storage. Nonetheless, after ~19 ka both TR163-20B and TR163-23 document similar changes in Δ[CO_3^{2-}].

2.6 Discussion

2.6.1 Deglacial Mid-Depth Oxygenation

Southern Ocean records of deep-water chemistry indicate that increases in export production occurred simultaneously with reductions in ventilation, bottom-water oxygenation, and atmospheric CO_2 during the last two glacial periods (Gottschalk et al., 2016). Many studies of the glacial-interglacial transfer of CO_2 between the oceans and atmosphere have focused on changes in the biological pump in the Southern Ocean because this is a key region of modern CO_2 evasion to the atmosphere. Less attention has been paid to the dynamics of these processes in low-latitude upwelling regions such as the EEP, although the modern EEP is also an important source of CO_2 to the atmosphere.

Our $\Delta\delta^{13}C$ oxygen estimates suggest that increasing mid-depth oxygenation in the EEP occurred in unison with increases in ventilation. Specifically, both mid-depth $[O_2]$ and $\Delta^{14}C_{0\text{-}atm}$ increase gradually through HS1 with rapid increases at the HS1-BA transition (Figure 2.7). Benthic foraminiferal $\delta^{13}C$ values have been suggested to reflect microhabitat differences and species-specific "vital effects" (McCorkle et al., 1990). The $\delta^{13}C$ gradient among foraminifera at different microhabitat depths is a function not only of oxygen availability but also of the quality and quantity of organic matter reaching the sea floor (Jorissen et al., 1995). A decrease in the $\delta^{13}C$ gradient reflects a shoaling of the average living depths of infaunal foraminifera taxa. While different species may exhibit large shifts in microhabitat depth as a response to different environmental drivers (e.g. food and oxygen availability, bioturbation, competition, and predation), convergence of $\delta^{13}C$ among several different species reflects a general decline in oxygen and organic matter availability. Our results indicate that the $\delta^{13}C$ gradient among the different benthic

foraminifera taxa increased from the LGM to the Holocene (Figure 2.4), suggesting a divergence in average microhabitat depth consistent with our $\Delta\delta^{13}C$ estimates of increasing oxygenation.

It has been hypothesized that bottom-waters would become suboxic or even anoxic during periods of reduced ventilation (Hain et al., 2011). While mid-depth oxygenation was much lower during the LGM and HS1, our core site never approached suboxic conditions (Figure 2.7). This may not have been the case for the entire EEP. The productivity history of the equatorial Pacific has been shown to be spatially variable, especially within the EEP (Costa et al., 2017; Jaccard and Galbriath, 2011). Several patterns of glacial-interglacial productivity changes have been identified for this region, including a deglacial productivity maximum (Costa et al., 2017) similar to the U_a maximum recorded in the two deeper TR163 cores, 23 and 20B (Figure 2.5). Similarly, some records suggest a reduction of glacial productivity while other records suggest that productivity was enhanced during the LGM (Costa et al., 2017), much like we find in the U_a from TR163 cores 14 and 25 (Figure 2.5). Spatial variability in productivity could account for some of these differences. The two deeper cores, TR163-23 and TR163-20B, were collected from the Galapagos platform in the core of equatorial upwelling whereas the shallower cores, TR163-14 and TR163-25, were collected from the Carnegie and Cocos ridges (Figure 2.2). Previous studies of Galapagos and Panama Basin cores have emphasized the susceptibility of this region to trace element enrichments related to hydrothermal activity, reducing conditions, and volcanic debris (Lea et al., 2005; Pena et al., 2005). An input of hydrothermal Mn or formation of Mn-carbonate overgrowths (Pena et al., 2005) could bias the authigenic U/Mn values toward lower U_a and account

for the different U_a histories between the cores located off the Galapagos and on the ridges.

2.6.2 Eastern Equatorial Pacific Carbonate Chemistry

Carbonate ion saturation ($\Delta[CO_3^{2-}]$) estimates from B/Ca provide an additional measure of glacial respired carbon storage (Figure 2.6) and can provide additional constraints on the deglacial biological pump to help disentangle the inconsistencies among records of export productivity and oxygenation. An increase in the amount of respired carbon stored in the deep ocean would result in decreased carbonate ion concentrations and subsequent dissolution of $CaCO_3$ to compensate for the excess CO_2. Similarly, $CaCO_3$ compensation would have buffered excess CO_2, allowing the deep-ocean to store larger amounts of respired carbon during the LGM and HS1 and avoid anoxic conditions (Broecker and Peng, 1987). Because $CaCO_3$ compensation works on time scales of several thousand years, it has been hypothesized that abrupt ventilation of a respired carbon reservoir would result in a brief perturbation of carbonate ion saturation and carbonate preservation, followed by a return to steady-state $\Delta[CO_3^{2-}]$ values (Broecker and Peng, 1987). Because carbonate compensation does not occur at the shorter timescales observed during the deglaciation, brief changes in carbonate saturation are driven by other processes such as changes in organic matter respiration and export along with changes in ocean circulation and ventilation. The B/Ca record from TR163-23 displays no overall change between mean glacial and mean Holocene $\Delta[CO_3^{2-}]$ values is recorded, suggesting that sufficient $CaCO_3$ was present to fully buffer the glacial-interglacial change in respired CO_2 at this core location (Figure 2.7). However, significant changes in carbonate ion concentration occur at this core location during

deglaciation. During HS1 and the YD, carbonate ion concentrations are at their lowest, coincident with reduced ventilation as indicated by the ^{14}C record (Figure 2.7).

The low carbonate ion values during HS1 and YD are separated by a mid-deglacial (BA) maximum in $\Delta[CO_3^{2-}]$ (Figure 2.7). This mid-deglacial $\Delta[CO_3^{2-}]$ maximum occurs coevally with a period of increasing ventilation providing support for a link between CO_2 evasion and increasing $\Delta[CO_3^{2-}]$. Surprisingly, the lowest $\Delta[CO_3^{2-}]$ values are recorded in TR163-23 during the Younger Dryas rather than during HS1 or the LGM when ventilation rates were lowest. This is the same period of time when the highest U/Mn concentrations are recorded suggesting enhanced productivity as a driver of much of the $\Delta[CO_3^{2-}]$ decrease. Also, accumulation of respired carbon in association with recorded reductions in ventilation would have amplified the productivity driven $\Delta[CO_3^{2-}]$ decreases and contributed to the very low $\Delta[CO_3^{2-}]$ values at this time

2.6.3 Regional Trends in Carbonate Chemistry

A compilation of published records of B/Ca from the Atlantic and Pacific oceans reveals significant regional variability in past carbonate ion saturation (Figure 2.8). When separating records by ocean and depth, several distinctive patterns emerge. For the North Atlantic (including the Caribbean Sea), mid and intermediate water depth records (1.2-3.6 km; Figure 2.8) display an overall decrease in B/Ca from the LGM to Holocene, while the reverse is true for records from deep water-depths (>3.5 km). The larger intermediate to deep-water carbonate ion gradient in the glacial north Atlantic relative to the Holocene (Figure 2.9) can be attributed to increased stratification and a reorganization of water masses in the Atlantic (Yu et al., 2013). Specifically, the replacement of nutrient-poor,

northern-sourced waters with nutrient-rich, southern-source waters would allow greater respired carbon storage in the deep-Atlantic.

Little to no overall change between glacial and late Holocene carbonate ion concentration is seen in the equatorial Pacific and S. Atlantic records (Figure 2.8). Notably, carbonate ion concentrations from the Western Equatorial Pacific (WEP) and Central Equatorial Pacific (CEP) remain almost unchanged throughout the glacial-interglacial transition, with lower [CO_3^{2-}] generally corresponding to deeper water-depths. This could indicate the absence of a glacial respired carbon reservoir in the WEP and CEP, or changes in carbonate saturation could by obscured by simultaneous changes in circulation. There are two major return pathways for North Pacific deep water to the Southern Ocean (Key et al., 1996), an eastern path and a less well-defined western path. Changes in the vertical and/or horizontal extent of the western pathway could overprint [CO_3^{2-}] changes related to changes in respired carbon storage in the WEP and CEP. Alternately, changes in the North Pacific-Southern Ocean deep water mixing ratio may also have obscured any glacial-interglacial [CO_3^{2-}] changes (Yu et al., 2010).

Although carbonate ion concentrations in the EEP, Southwest Pacific, and S. Atlantic return to glacial-like values during the Holocene, these locations document a distinct deglacial maximum in carbonate saturation. Carbonate ion concentrations in the EEP and SW Pacific began to increase during the mid to late HS1, reaching maximum [CO_3^{2-}] at ~14.5 ka. The increase in EEP and SW Pacific [CO_3^{2-}] occurred concurrently with the onset of increases in both ventilation and [O^2] recorded by TR163-23. This suggests that changes in the rate of Southern Ocean circulation drove not only the shifts in the carbonate saturation in the EEP but also in the SW Pacific, as both the EEP and

SW Pacific core sites lie along the return pathway of PDW circulation. However, S. Atlantic [CO_3^{2-}] values do not begin to increase until ~15.0 ka, simultaneous with the resumption of Atlantic Meridional Overturning Circulation (AMOC).

Depth transects of carbonate ion concentrations from the equatorial Pacific for different time periods (Holocene, BA, and LGM) show much smaller shifts in the deep-water [CO_3^{2-}] gradient than recorded in the North Atlantic (Figure 2.9), with very little to no change in the equatorial Pacific gradient aside from a slight glacial-interglacial increase in [CO_3^{2-}] at ~3.4 km water depth. During the Holocene, the EEP [CO_3^{2-}] gradient resembles the rest of the equatorial Pacific, with slightly increasing [CO_3^{2-}] with depth but overall higher [CO_3^{2-}] concentrations than found in the WEP and CEP. Notably, the EEP gradient displays a pronounced minimum in glacial [CO_3^{2-}] values at ~2.4 km water depth that persists into the Bølling Allerød (Figure 2.9). If this glacial low in [CO_3^{2-}] is indicative of enhanced respired carbon storage, it is surprising that it persists into the Bølling Allerød when there was a rapid increase in ventilation. However, rather than low [CO_3^{2-}] values at 2.4 km driving this feature, it is high [CO_3^{2-}] values at ~1.6-2.0 km that account for this pattern, suggesting a transfer of alkalinity from deep to intermediate water depths during the Bølling Allerød. Although some of the respired carbon reservoir may have persisted through the Bølling Allerød in mid-depth waters, much of it had likely dissipated by this time.

During the glacial period, [CO_3^{2-}] values from intermediate depth waters in the SW Pacific, mid-depth waters in the EEP and deep-waters in the North Atlantic begin to approach the low [CO_3^{2-}] values recorded in the WEP and CEP, suggesting that during the LGM/HS1 these regions were all influenced by southern-source waters. This previously

described homogenization of deep waters from the North Atlantic and the equatorial Pacific (Yu et al., 2013) can now be extended to the EEP at water depths of ~2.2 km and to the SW Pacific at water depths of ~1.6 km. This is consistent with the Southern Ocean being a dominant driver of changes in both the Atlantic and Pacific during deglaciation (Umling and Thunell, 2017) due to increasing Southern Ocean sea ice extent and/or stratification (Stephens and Keeling, 2000; Ferrari et al., 2014).

2.7 Conclusions

Our $\Delta\delta^{13}C$ records of oxygen concentrations and authigenic uranium records of redox history suggest that oxygenation generally increased in intermediate and deep waters of the EEP during the glacial-interglacial transition. B/Ca records of carbonate chemistry reveal decreases in carbonate saturation during periods of reduced ventilation along with a mid-deglacial carbonate ion maximum similar to what has been recorded in the SW Pacific (Allen et al., 2015). The deglacial increases in $[O_2]$ and $[CO_3^{2-}]$ occur in tandem with increased EEP ventilation, supporting a deglacial release of a respired carbon reservoir. The link between mid-depth respired carbon storage and ventilation suggests that the link between the biological pump and circulation was not limited to the Southern Ocean (Gottschalk et al., 2016) but extended to the EEP during the last glacial-interglacial transition. Furthermore, the similarity of EEP glacial carbonate ion concentrations with those of the western and central equatorial Pacific corroborates the proposed homogenization of glacial deep waters (Yu et al., 2013) and suggests that the Southern Ocean was a primary driver of respired carbon storage and release during the deglaciation.

Table 2.1 Core locations and depths.

Core	Latitude	Longitude	Depth (m)
TR163-2	8° 14.4’ N	84° 21.0’ W	1,620
TR163-14	5° 54.0’ N	87° 14.4’ W	2,365
TR163-18	2° 48.6’ N	89° 51’ W	2,030
TR163-20B	0° 47.4’ N	93° 50.4’ W	3,200
TR163-23	0° 24.6’ N	92° 9.6’ W	2,730
TR163-25	1° 39’ S	88° 27’ W	2,650

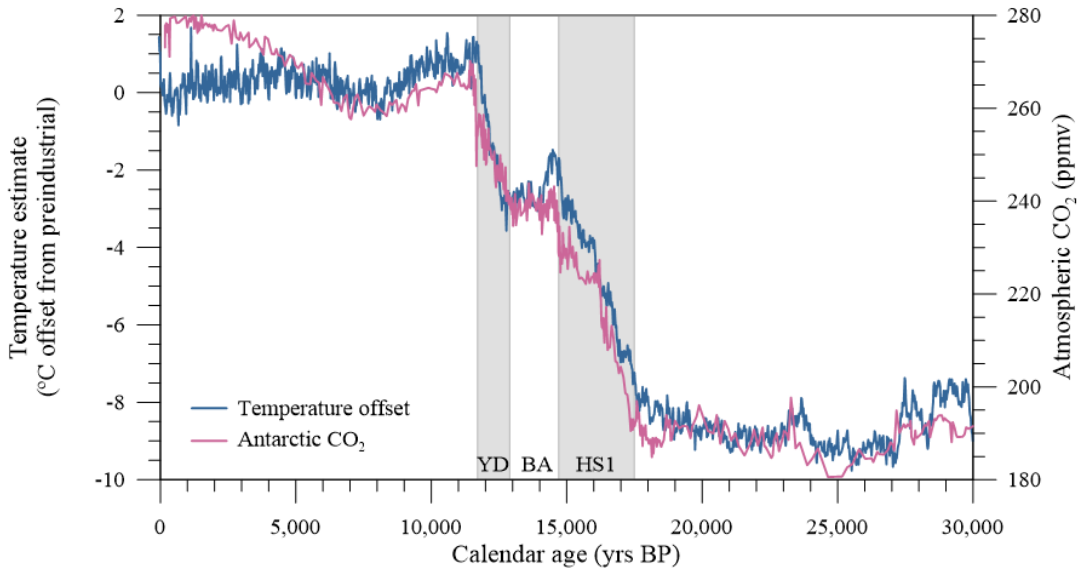

Figure 2.1 Antarctic records of atmospheric CO_2 (Bereiter et al., 2015) and temperature (Parrenin et al., 2015) indicate periods of gradual increase during the Younger Dryas (YD) and Heinrich Stadial 1 (HS1) separated by a period of very little to even decreasing change during the Bølling Alerød (BA).

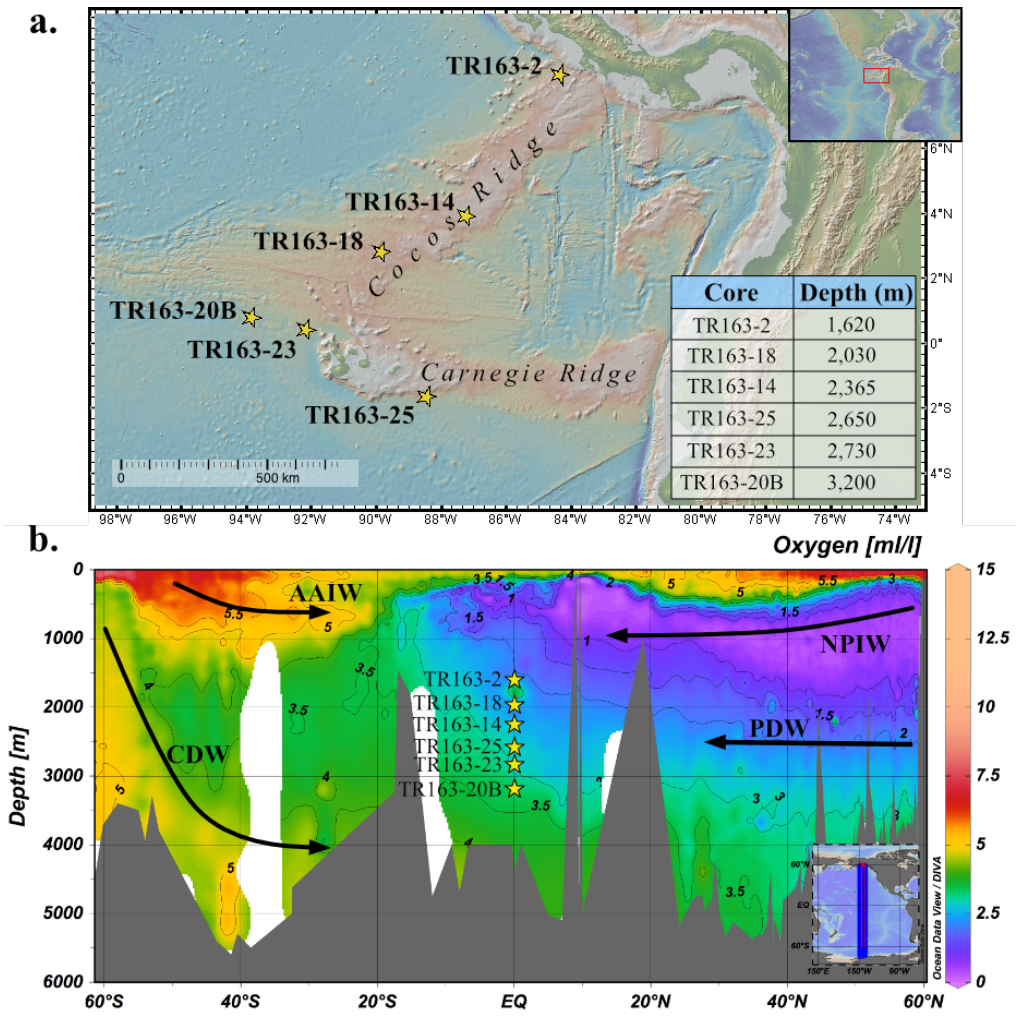

Figure 2.2 **(a)** High resolution core TR163-23 is located off the Galapagos Platform in the equatorial cold tongue region. A transect of TR163 cores located on the Cocos and Carnegie ridges is used for lower-resolution carbonate-ion study. **(b)** Core locations relative to Pacific water masses is depicted on a plot of modern oxygen content from the Global Data Analysis Project (GLODAP; Key et al., 2004).

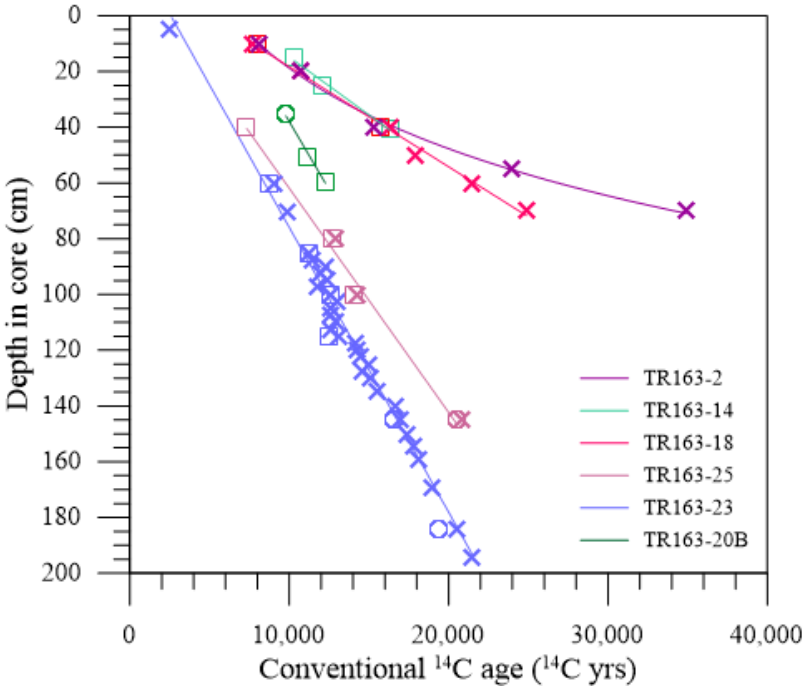

Figure 2.3 Radiocarbon ages for each core were measured from *Neogloboquadrina dutertrei* (X) and *Globogerinoides ruber* (squares) samples. Small samples of *G. ruber* samples were supplemented with *Globogerinoides sacculifer* (circles) to achieve sufficient material for AMS analysis. All samples were measured for radiocarbon content at the University of California, Irvine Keck-Carbon Cycle AMS facility.

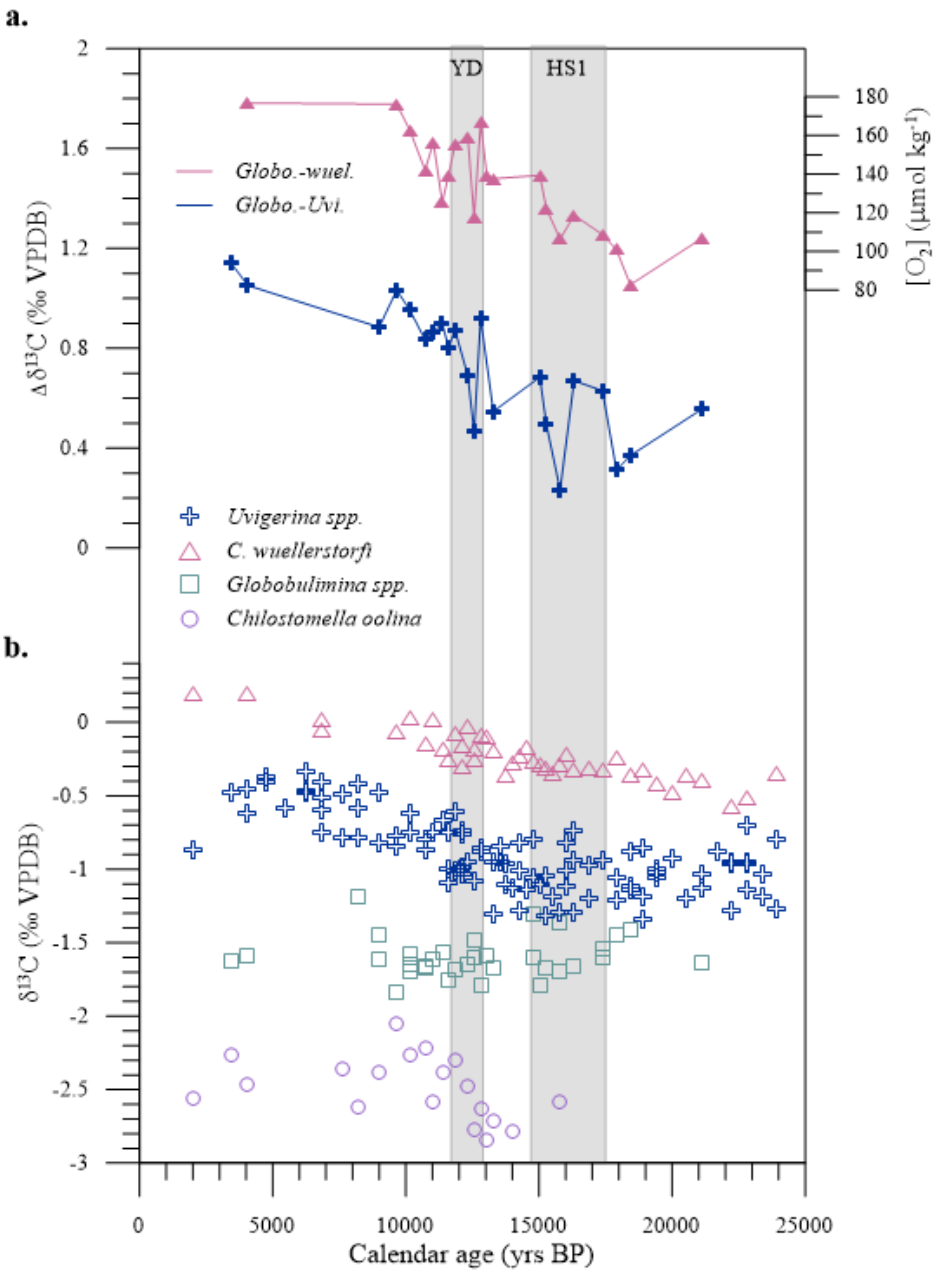

Figure 2.4. **(a)** The oxygen content for TR163-23 was estimated using the calibration of Hoogakker et al. (2014) for the $\delta^{13}C$ offset between deep-dwelling infaunal benthic foraminifera *Globobulimina spp.* and the epifaunal foraminifera *C. wuellerstorfi*. The difference in the carbon isotopic values of *Globobulimina spp.* and shallow infaunal species *Uvigerina spp* demonstrate similar offsets. **(b)** *Globobulimina spp.* $\delta^{13}C$ values decrease slightly through deglaciation, whereas *Uvigerina spp.* and *C. wuellerstorfi* $\delta^{13}C$ values increase over the same period. While *Chilostomella oolina* carbon isotopes show a sharp increase over the late deglacial, there were insufficient individuals present for $\delta^{13}C$ measurements during the early deglacial and LGM.

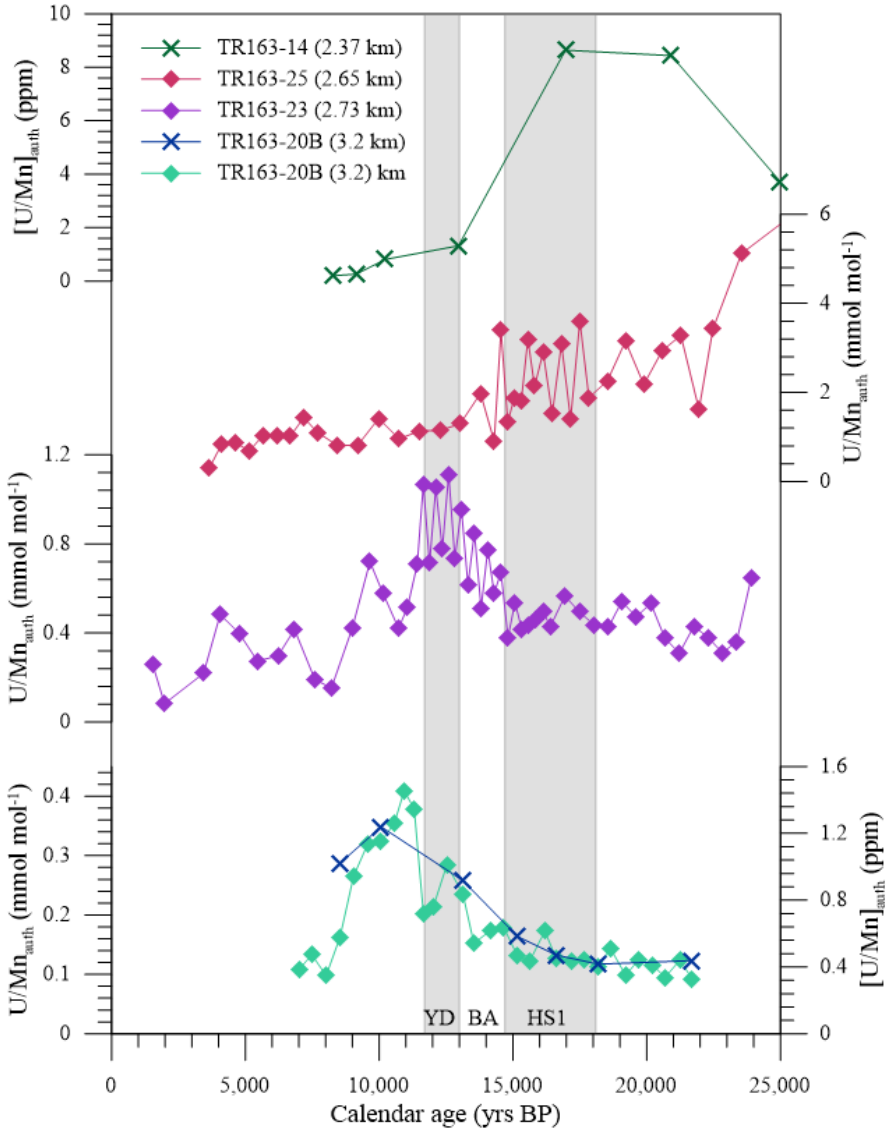

Figure 2.5 Authigenic uranium concentrations were measured in bulk planktonic foraminifera samples (X's) and normalized to manganese concentrations. Authigenic uranium to calcium ratios (U/Ca) were measured in *N. dutertrei* samples (diamonds) and normalized to manganese to calcium ratios (Mn/Ca). Despite the method used, U_a from TR163-20B displays the same glacial-interglacial pattern. Cores TR163-14 and TR163-25 record significantly higher concentrations of U_a during the LGM and early deglaciation than recorded by TR163-23 and TR163-20B over the entire glacial-interglacial transition.

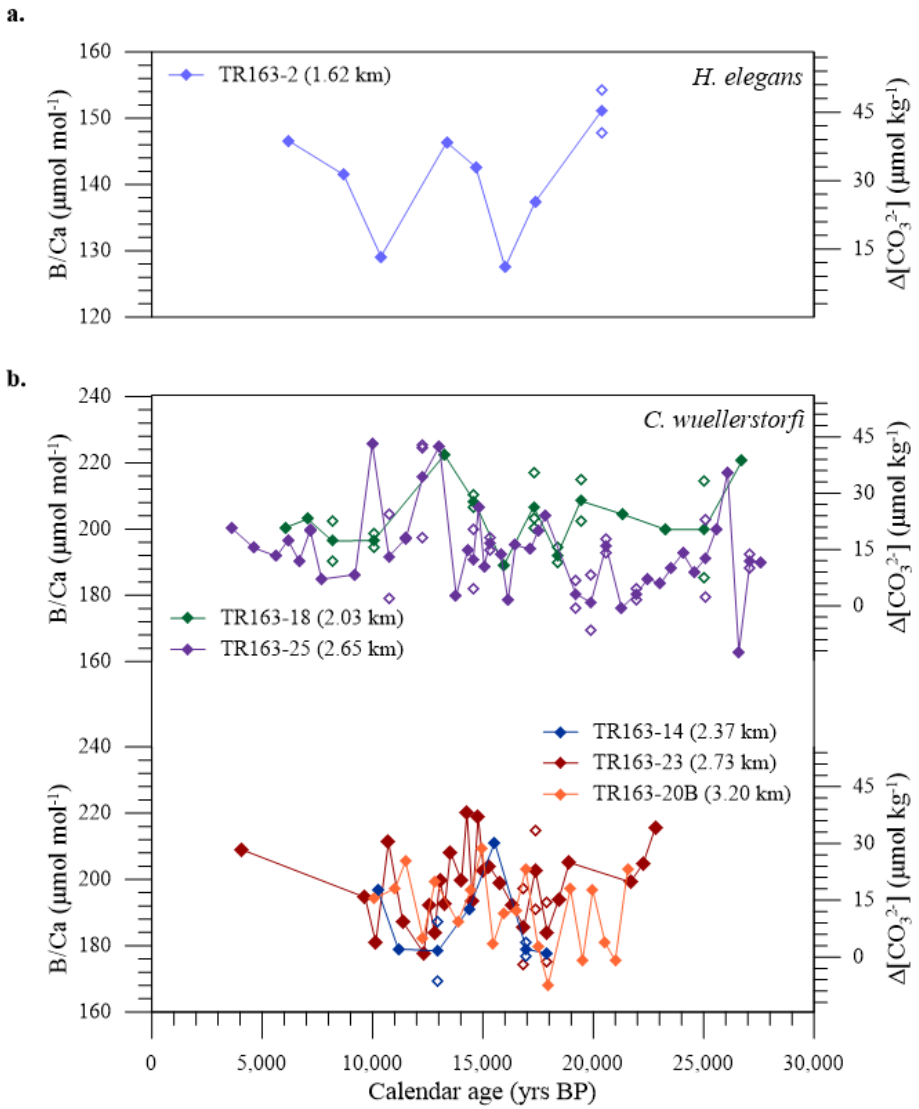

Figure 2.6. Using the global core-top calibrations from Yu et al. (2013), **(a)** the degree of carbonate saturation, $\Delta[CO_3^{2-}]$, was estimated from *C. mundulus* for TR163-2 (1.62 km). **(b)** B/Ca from *C. wuellerstorfi* was used to calculate $\Delta[CO_3^{2-}]$ for TR163 cores from below 2 km water depth. Open diamonds indicate replicates used to compute an average value for a specific core depth.

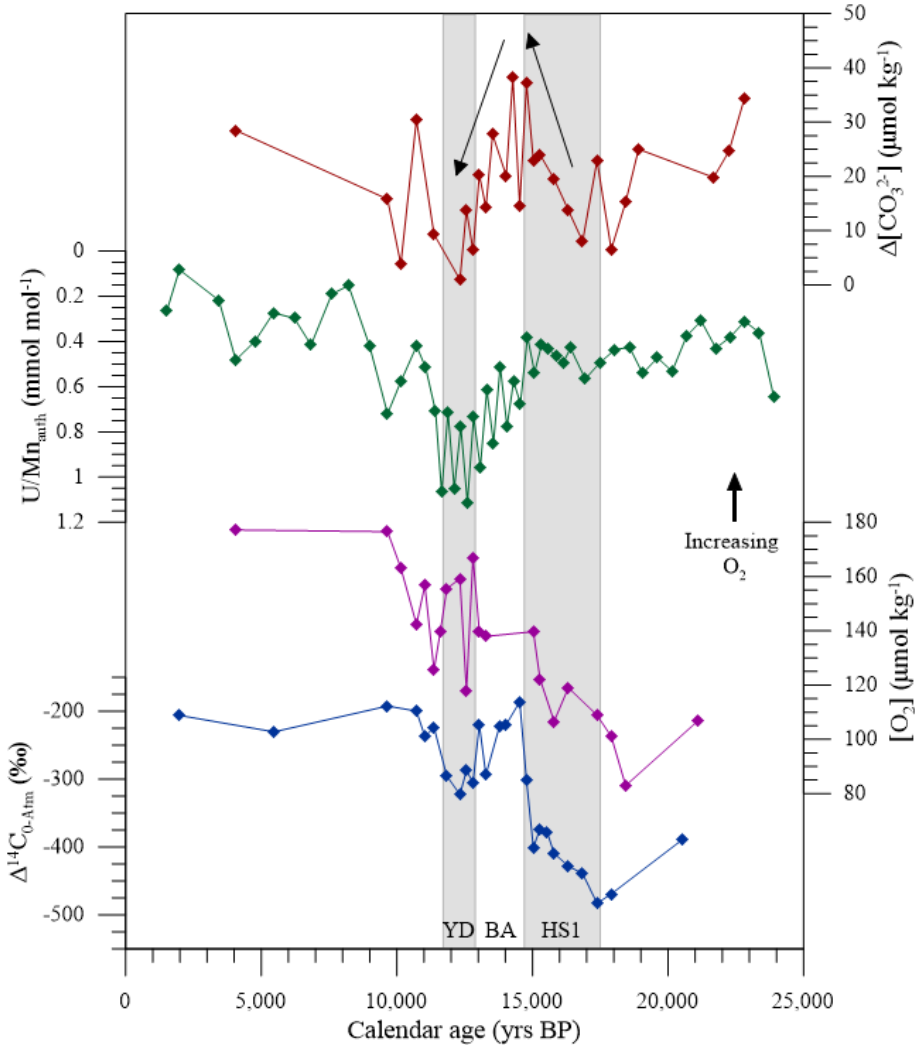

Figure 2.7 Past deep-water carbonate chemistry was constrained for TR163-23 using a benthic record of B/Ca developed for reductive and oxidatively cleaned samples of *C. wuellerstorfi* suggest a mid-deglacial maximum in carbonate ion concentration. The redox history of TR163-23 was constrained from measurements of authigenic uranium developed from lightly cleaned (clay removal only) samples of *N. dutertrei* and normalized to manganese concentrations following Gottschalk et al (2016; U/Mn). Oxygen content estimated from the $\delta^{13}C$ difference between epifaunal species *C. wuellerstorfi* and deep-infaunal species *Globobulimina spp.* demonstrates gradually increasing $[O_2]$ over the glacial-interglacial transition broadly similar to periods of increasing ventilation recorded in the same core (Umling and Thunell, 2017).

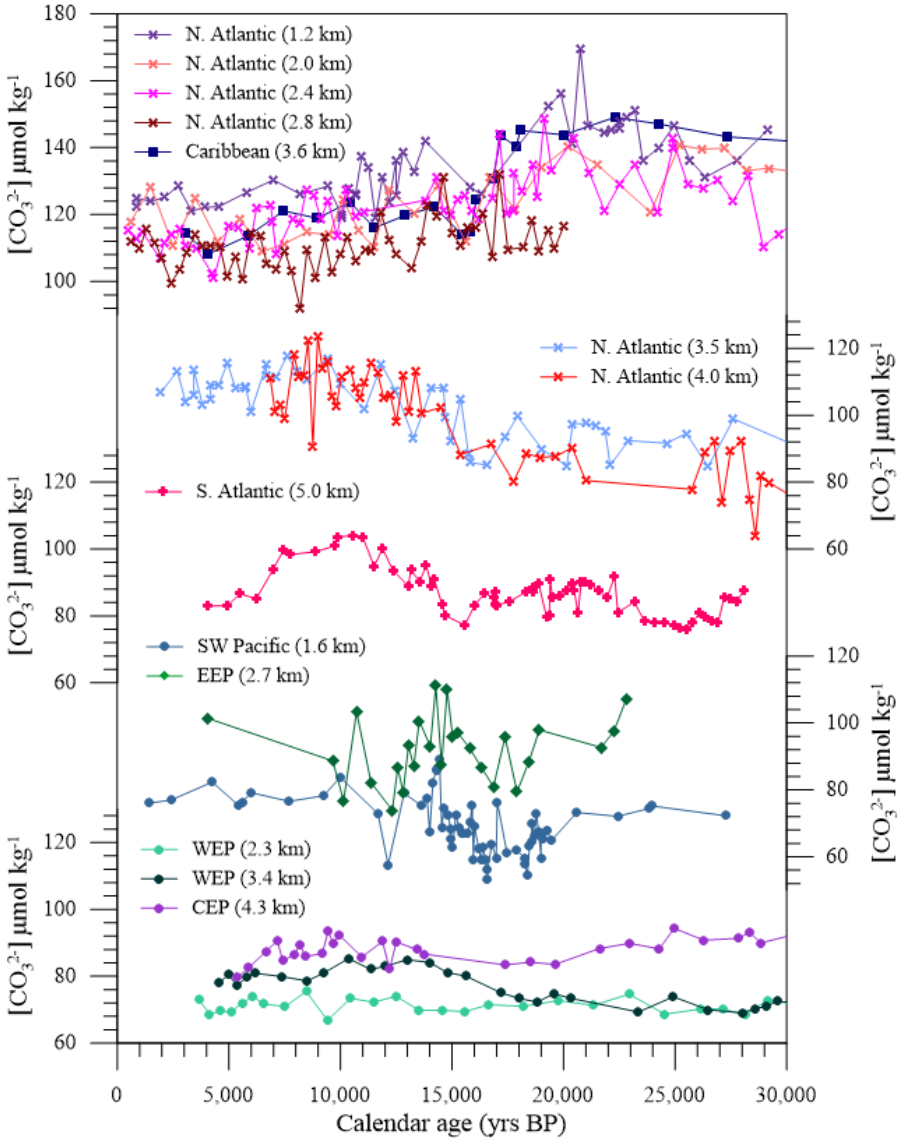

Figure 2.8 A compilation of B/Ca records from the North Atlantic (Yu et al., 2008), Caribbean Sea (Yu et al., 2013), South Atlantic (Yu et al., 2014), Western Equatorial Pacific (WEP; Yu et al., 2013), Central Equatorial Pacific (CEP; Yu et al., 2013), Eastern Equatorial Pacific (this study), and the Southwest Pacific (Allen et al., 2015) demonstrate regional variability. The benthic foraminifera species *Cibicidoides wuellerstorfi* was used for all records shown here, excluding the N. Atlantic record from 1.2 km water-depth which used *Cibicidoides mundulus*. Records from intermediate to mid-depth North Atlantic water depths (1.2-2.8 km) and the deep Caribbean Sea (3.6 km) suggest declining carbonate ion concentration from the LGM to the Holocene. Alternatively, records from the deep North Atlantic (3.5-4.0 km) and abyssal South Atlantic (5 km) suggest increasing [CO_3^-] during this same period. Pacific records reveal a different trend with a mid-deglacial peak in [CO_3^-] during deglaciation recorded in the EEP and SW Pacific while little to no change is recorded in WEP and CEP waters.

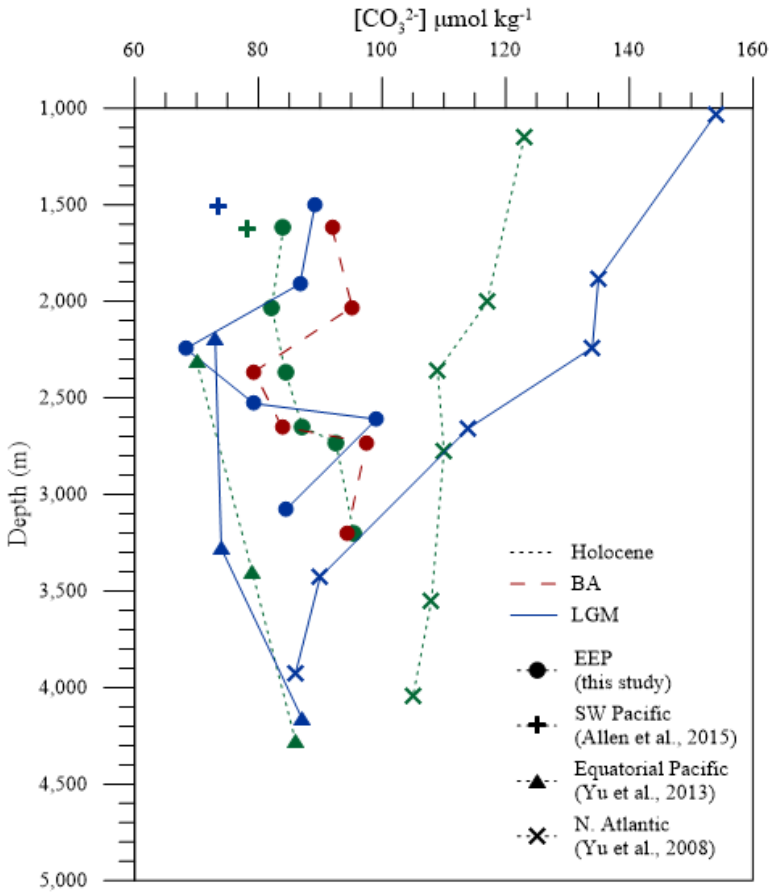

Figure 2.9 Depth profiles of carbonate ion concentrations estimated from benthic B/Ca following Yu et al. (2013) and Allen et al. (2015). Glacial water depths have been adjusted for 120 m lower sea levels. The North Atlantic changes in $[CO_3^{2-}]$ are dominated by changes in ocean circulation whereas Pacific $[CO_3^{2-}]$ more closely reflects changes in carbon inventory.

CHAPTER 3

EVIDENCE FOR GLACIAL DEEP-WATER EXPANSION AND ENHANCED REMINERALIZATION IN THE EASTERN EQUATORIAL PACIFIC[3]

[3] Umling, N.E., Thunell, R.C., Bizimis, M. To be submitted to *Paleoceanography.*

3.1 Abstract

Previously published foraminiferal-derived estimates of bottom water oxygenation and carbonate chemistry from multiple locations suggest the build-up of a mid-depth respired carbon reservoir during the last glacial period that subsequently was released to the atmosphere during deglaciation. This movement of carbon between the oceans and atmosphere has generally been attributed to changes in the biological pump and ocean ventilation. However, reorganization of intermediate and deep water-masses could complicate our understanding of changes in the biological pump and ventilation during this time period. Here we present benthic foraminiferal carbon isotope ($\delta^{13}C$) and cadmium/calcium (Cd/Ca) records from the eastern equatorial Pacific to identify water masses and constrain circulation changes since the last glacial period in this region. These records are complemented with elemental measurements of the authigenic coatings of foraminifera to monitor post-depositional changes in bottom water properties. Our results suggest a glacial expansion of Lower Circumpolar Deep Water (LCDW), consistent with increased influence of southern sourced waters during periods of increased sea-ice extent and/or stratification. Additionally, our records demonstrate increased organic matter remineralization in mid-depth waters during the last glacial period. This suggests that variability in both ventilation and biological pump efficiency were important mechanisms for the glacial-interglacial transfer of CO_2 between the oceans and atmosphere.

3.2 Introduction

Changes in atmospheric CO_2 are thought to amplify solar variability associated with the orbital cycles, driving the transition between glacial and interglacial climate states over at least the last ~800 kyr (Sigman and Boyle, 2000, Galbraith and Eggleston,

2017). The abrupt CO_2 increases during the last deglaciation (Parrenin et al., 2013) provide a unique opportunity to study the relationship between increasing CO_2 and rapid climate warming. Because of the size and mobility of the deep ocean carbon reservoir, it has been implicated as the primary source of CO_2 to the atmosphere during deglaciation (Broecker and Barker, 2007). Antarctic ice cores record decreasing atmospheric radiocarbon values simultaneous with increasing CO_2 (Hughen et al., 2000; Monnin et al., 2001), suggesting the a ^{14}C-depleted carbon source to the atmosphere.

It has been hypothesized that changes in Southern Ocean meridional overturning circulation driven by increased sea ice extent or stratification allowed respired carbon to accumulate in the deep-ocean during the last glacial period (Anderson et al., 2009; Keeling and Stephens, 2001; Toggweiler et al., 2006; Watson et al., 2015). Isolation of deep-waters would have allowed ^{14}C to decay, thus providing a source for the ^{14}C-depleted carbon delivered to the atmosphere during deglaciation (Broecker and Barker, 2007). Additionally, changes in the efficiency of the oceanic biological pump have been linked to the glacial-interglacial transfer of CO_2 between the oceans and atmosphere (Hertzberg et al., 2016; Pichevin et al., 2009; Ziegler et al., 2013). However, it has been estimated that the biological pump could only have contributed up to half of the observed CO_2 flux (Kohfeld et al., 2005), necessitating an additional process such as ventilation to achieve the full glacial-interglacial CO_2 change.

Recent evidence suggests that respired carbon primarily accumulated in mid-depth waters rather than deep-waters during the last glacial (Burke et al., 2015) due to shoaling of the boundary between the upper and lower branches of Southern Ocean overturning circulation (Skinner et al., 2010; Ferrari et al., 2014). Furthermore, an

increase in the proportion of cold, nutrient-rich Lower Circumpolar Deep Water (LCDW) relative to other deep water masses, would have allowed the oceans to store more carbon without necessitating changes in ventilation rate or biological productivity (Skinner, 2009). Reductions in mid-depth ^{14}C are coeval with increases in respired carbon in the eastern equatorial Pacific (EEP) during the last glacial period (Umling and Thunell, submitted). However, it is not known whether this region underwent an expansion of LCDW or whether a decreased ventilation alone was responsible for the low ^{14}C values (de la Fuente et al., 2015; Umling and Thunell, 2017).

Here we characterize the water masses of the deep eastern equatorial Pacific during the last 25,000 years utilizing coupled measurements of benthic foraminiferal carbon isotopes ($\delta^{13}C$) and cadmium/calcium (Cd/Ca) from a transect of sediment cores from the Panama Basin. Cadmium is tightly coupled with the nutrient phosphate in the world's oceans and foraminiferal Cd/Ca ratios have been shown to record the seawater cadmium concentrations with a depth-dependent fractionation (Boyle, 1992). Similarly, seawater $\delta^{13}C$ is related to biological nutrient utilization and demonstrates a negative correlation with phosphate. As surface waters equilibrate with the atmosphere during air-sea exchange, there is an additional isotopic fractionation of carbon (Inoue and Sugimura, 1985). Therefore, the $\delta^{13}C$ value of a water-mass reflects both air-sea exchange and nutrient utilization. By utilizing Cd/Ca to constrain the nutrient concentration, the air-sea component of $\delta^{13}C$ ($\delta^{13}C_{as}$) can be isolated from the measured $\delta^{13}C$ (Lynch-Stieglitz and Fairbanks, 1994; Lynch-Stieglitz et al., 1995). Together, measurements of benthic foraminiferal Cd/Ca and $\delta^{13}C$ provide information on both water mass source and deep-water mixing along with nutrient utilization.

3.3 Sample Material and Oceanographic Setting

This study utilizes a series of cores collected from intermediate and deep water-depths (1,620-3,200 m) of the Panama Basin during R/V Trident cruise TR-163 (Table 3.1; Figure 3.1). The Panama Basin is a semi-enclosed basin bounded by South and Central America to the north and east. The Carnegie and Cocos submarine ridges form the southern and northwest boundaries of the basin, converging westward towards the volcanically active Galapagos Islands. The Galapagos spreading center extends eastward along 1°N towards the center of the basin and northeast from the center of the basin towards Panama. These features are potential sources of volcanic and hydrothermal products to the surrounding sediments (Pedersen, 1979). Deep-water cores TR163-23 and TR163-20B were collected off the west flank of the Galapagos platform at depths of 2,730 and 3,200 m, respectively. TR163-25 was collected from the Carnegie Ridge and the three shallowest cores were collected from the Cocos Ridge (Figure 3.1). No distinct ash layers were found in any of the cores, but TR163-23 occasionally contained volcanic debris mainly comprised of amber-brown to clear volcanic shards. These glass shards are consistent with microtephra described from nearby core TR163-22 (Lea et al., 2005) and similar deposits have been described for the Panama Basin by Kowsman (1973) and attributed to subaerial eruptions or extremely shallow submarine vents.

The Eastern Equatorial Pacific (EEP) is a region characterized by a shallow thermocline and the upwelling of nutrient-rich waters. In particular, surface waters near the Galapagos Islands are highly productive due to upwelling of the Equatorial Undercurrent (EUC; Pennington et al., 2006). The basin is also marked by a strong meridional sea surface temperature (SST) gradient. The southern part of the basin is

located within the equatorial cold-tongue with SST increasing northward across the basin into the eastern Pacific warm-pool (Fiedler and Talley, 2006). The world's largest oxygen minimum zones are located in the eastern Pacific, north and south of the equator at depths of ~250-1,000 m (Kamykowski and Zentara, 1990). At present, abyssal waters (>3,500 m) in the EEP originate from Lower Circumpolar Deep Waters (LCDW) that has been modified by geothermal heating within deep basins of the eastern Pacific (Lonsdale, 1976; Tsuchiya and Talley, 1998). These waters are overlain by Pacific Deep Water (PDW) at mid-depths (~1,000-3,200 m) and by Equatorial Pacific Intermediate Water (EqPIW) at intermediate water-depths (~700-1000 m; Tsuchiya and Talley, 1998).

The heterogeneous distribution of hydrothermal and volcanic activity, along with variable surface productivity and water-column oxygenation sets up a complex geochemical environment within the Panama Basin. Precipitation of manganese-carbonate phases have been documented (Pedersen and Price, 1982; Boyle, 1983; Pena et al., 2008) in Panama Basin sediments along with Al-silicate contamination (Lea et al., 2005). These conditions require careful cleaning of foraminiferal samples along with close monitoring of authigenic and biogenic element compositions.

3.4 METHODS

Carbon isotopes were measured on specimens of the benthic foraminifera *Cibicidoides wuellerstorfi* from three TR163 cores with sedimentation rates >5 cm/kyr, (TR163-20B, TR163-23, and TR163-25). All analyses were carried out on a GV Isoprime stable isotope ratio mass spectrometer. The long-term reproducibility of $\delta^{13}C$ measurements is 0.06‰ and all samples are reported relative to the Vienna Peedee belemnite scale (VPDB). Samples were cleaned for isotopic analysis in 3% H_2O_2 to

remove organic material and then briefly sonicated in acetone to remove adhered particles. *Cibicidoides wuellerstorfi* is ideal for monitoring past deep-ocean chemistry as it has an epifaunal habitat and has been shown to incorporate carbon isotopes in a roughly 1:1 ratio with bottom water (Mackensen, 2008; Schmittner et al., 2017). Age models for these cores were constructed from calibrated radiocarbon ages with a variable reservoir age as previously reported (Umling and Thunell, 2017).

Samples of 5-15 *C. wuellerstorfi* were cleaned for trace element analysis following the Cd-cleaning protocol from Boyle and Keigwin (1985/86) as modified by Boyle and Rosenthal (1996) using the minimal settling technique from Barker et al. (2003). All analyses were carried out on a Thermo Element II High Resolution ICP-MS at the Center for Elemental Mass Spectrometry (CEMS) at the University of South Carolina. To minimize matrix effects, the Ca content of each analyzed sample solution was matched to a gravimetrically made standard at 20 ppm Ca, by first performing a dip check and diluting the sample. The analytical reproducibility for Cd/Ca is ± 0.003 μmol mol^{-1} (± 3.7%) based on repeated measurements of a standard of ~0.190 μmol mol^{-1}.

We monitored Al-silicate and oxide contamination through concurrent analysis of diagenetic indicators Fe/Ca, Mn/Ca, and Al/Ca. The Fe/Ca values were generally low (<50 mmol mol^{-1}) in all TR163 cores; samples with elevated Fe/Ca values (>100 mmol mol^{-1}) were excluded. In contrast, Mn/Ca and Al/Ca values were commonly elevated (>100 μmol mol^{-1}) with increasing Mn/Ca values with depth and higher Al/Ca values generally found in the mid-depth cores. High Al/Ca and Mn/Ca values are not unusual for Panama Basin sediment cores, with precipitation of Mn-carbonate coatings (Boyle, 1983; Pena et al., 2005, 2008), formation of Mn-oxides (Balistrieri and Murray, 1986),

hydrothermal activity (Klinkhammer et al., 1977; Marchig et al., 1985), and volcanic debris (Lea et al., 2005) all serving as sources of Mn in this region. Because of the high spatial variability and differing chemical impacts of these processes, it has been proposed that identification of acceptable trace element data should utilize site-specific contamination thresholds (Lea et al., 2005). Here, samples with anomalous Al/Ca and Mn/Ca values (>500 μmol mol^{-1}) were excluded from data analyses, however a lower standard was required for TR163-20B Mn/Ca values (>1000 μmol mol^{-1}) as the mean Mn/Ca value for this core was ~520 μmol mol^{-1}. Low Fe/Ca values for TR163-20B suggest that the high foraminiferal Mn/Ca for this core is not associated with Fe oxides. Furthermore, Mg/Ca values from this core are not anomalously enriched as is the case with contamination from manganese-carbonate overgrowths (Boyle, 1983; Pena et al., 2005, 2008). Sedimentary enrichments of Mn have been attributed to flux from a high-Mn hydrothermal plume (Pedersen, 1979; Klinkhammer et al., 1977) and could be responsible for the elevated Mn/Ca in this core. Despite the higher threshold of Mn/Ca for TR163-20B, the Cd/Ca results from this core agree with previously reported Cd/Ca values from a similar depth Panama Basin core (TR163-31B; Boyle et al., 1988). Furthermore, the cleaned benthic Cd/Ca values for TR163-20B are not significantly correlated with Mn/Ca, Fe/Ca, or Al/Ca values (Supplementary figure D.1).

The cadmium concentration of seawater was estimated from the cleaned benthic foraminiferal Cd/Ca values using the empirical depth-dependent Cd distribution coefficient (D) of Boyle (1992) and normalizing Cd values for the average concentration of cadmium in seawater (0.01 mol kg^{-1}). For water depths greater than 3.0 km, D = 2.9 and for water depths 1.15-3.0 km, the equation from Boyle (1992) was used (Eq. 3.1).

$$D = 1.3 + (depth - 1150) * (1.6/1850) \quad \text{(Eq. 3.1)}$$

Major (^{43}Ca), minor (^{55}Mn), trace (^{27}Al, ^{47}Ti, ^{51}V, ^{53}Cr, ^{57}Fe, ^{59}Co, ^{60}Ni, ^{63}Cu, ^{111}Cd, ^{238}U), and rare earth (^{89}Y, ^{139}La, ^{140}Ce, ^{141}Pr, ^{145}Nd, ^{146}Nd, ^{147}Sm, ^{151}Eu, ^{157}Gd, ^{159}Tb, ^{163}Dy, ^{165}Ho, ^{167}Er, ^{169}Tm, ^{173}Yb, ^{175}Lu) element concentrations were measured on 50 mg samples of mixed planktonic foraminifera from the >355 µg size fraction using a Thermo Element II high resolution ICP-MS. Foraminifera were gently crushed to open shell chambers and cleaned for adhering clays using repeated ultrasonication and rinses of water and methanol (Boyle et al., 1981). Any remaining visible coarse grained silicates were removed by cleaning using a fine brush under a binocular microscope (Barker et al., 2003). A spike solution artificially enriched in ^{145}Nd was added to measured samples and blanks as internal standard. Briefly, the $^{145}Nd/^{146}Nd$ was used to calculate the absolute Nd concentration of each sample by isotope dilution, following the method of Willbold et al., (2003). The Nd concentration and the spike-corrected ^{146}Nd-signal becomes then the internal standard to monitor drift and quantify concentrations using ^{146}Nd-normalized signals. We used the USGS reference material BHVO-2 as an external standard for quantification of the samples. The Nd-concentrations are reproducible to within 1%. Overall precision and accuracy of the method is better than 5% for all elements. Full procedural blanks were corrected for and are insignificant (<1%) for all reported elements. Rare Earth Element (REE) concentrations were normalized to Post-Archaean Australian Shale (PAAS; Taylor and McLennan, 1985).

3.5 Results

The *C. wuellerstorfi* $\delta^{13}C$ values from TR163-25 and TR163-23 increase over the last glacial and interglacial transition by ~0.5‰ (Figure 3.2). This is consistent with the

documented mean whole ocean glacial-interglacial $\delta^{13}C$ increase of -0.46‰ (Curry et al., 1988). The $\delta^{13}C$ values from TR163-20B generally increase from the last glacial to the early Holocene by ~0.3‰, but record a brief return to glacial $\delta^{13}C$ values during the early Holocene (Figure 3.2). Additionally, TR163-23 $\delta^{13}C$ values are highly variable during the Younger Dryas (Figure 3.2).

The eastern equatorial Pacific cores document a glacial-Holocene difference in the seawater cadmium concentration (Cd_W) of ~0.2 nmol kg^{-1} at 2.73 km water depth (TR163-23), with values increasing from ~0.7 nmol kg^{-1} during the LGM to ~0.9 nmol kg^{-1} in the Holocene (Figure 3.3). Slightly larger glacial-interglacial Cd_W increases are recorded at shallower depths: 0.3 nmol kg^{-1} at 1.62 and 2.03 km water-depth (TR163-2 and TR163-18, respectively) and 0.4 nmol kg^{-1} at 2.65 km water-depth (TR163-25) (Figure 3.3). Holocene Cd_W averages for the cores used in this study are similar to eastern and western equatorial Pacific Cd_W values determined from the core-top benthic foraminiferal Cd/Ca data (Boyle,1988, 1992; Table 1; Figure 3.4). As with EEP present-day water column measurements (Key et al., 2004), our EEP foraminiferal Cd_W decreases slightly from 1.0 to 4.5 km water depth during both the Holocene and LGM (Figure 3.4). However, during the Holocene, EEP foraminiferal mean Cd_W values are slightly higher (~0.2 nmol kg^{-1}) in mid-depth waters relative to present-day water column values. This mid-depth feature was enhanced during the Last Glacial Maximum (LGM), with EEP mean Cd_W values being up to ~0.6 nmol kg^{-1} higher at ~2.0 km water depth, relative to the WEP (Figure 3.4). Additionally, the variability of foraminiferal Cd_W also increases during the LGM at these depths.

To assess possible geochemical influences on the foraminiferal Cd/Ca, authigenic REE and trace element compositions were measured on selected bulk planktonic foraminifera samples from deep-water core TR163-20B and mid-depth core TR163-14. The concentration of certain metals (Ni, Co, Cd, Ba, Zn) in marine sediments has been shown to increase with the formation of Mn-oxides (Balistrieri and Murray, 1986; Tribovillard et al., 2006). Pearson's correlation coefficients indicate that Mn has strong ($r^2 > 0.8$) correlations with Cd and Co and a moderately strong correlation ($0.6 < r^2 < 0.8$) with Ni in TR163-14 (Table 3.2). However, these elements were only mildly ($r^2 < 0.4$) correlated with Mn in deep-water core, TR163-20B. Elements characteristic of reducing environments (U, V, Cr; Tribovillard et al., 2006) showed only mild to modest correlations with Mn from TR163-14 (Table 3.2). The average concentration of authigenic Mn is enriched in TR16-20B (~400 ppm) relative to TR163-14 (~75 ppm) but the reverse is true for the average authigenic Cd concentration of TR163-20B (~0.08 ppm) relative to TR163-14 (~0.42 ppm).

Rare earth element profiles from both TR163-14 and TR163-20B record depletions in cerium relative to neighboring REEs (La and Nd; Figure 3.5). For consistency with previous studies the cerium anomaly (Ce/Ce*) was calculated here using the equation from German and Elderfield (1990).

$$Ce/Ce^* = 3 \cdot Ce / (2 \cdot La + Nd) \qquad \text{(Eq. 3.2)}$$

Negative cerium anomalies (Ce/Ce*<1) are a common feature in seawater and occur due to the oxidation of Ce(III) to Ce(IV) in the water column followed by rapid scavenging onto particles (Elderfield and Greaves, 1982). This results in a positive correlation of Ce/Ce* with water-mass age (German and Elderfield, 1990). However, this signal can be

overprinted by the pore-water reduction of Ce(IV) to Ce(III) under sub-oxic conditions resulting in a negligible (Ce/Ce* = 1) or positive (Ce/Ce* > 1) cerium anomaly (Wright et al., 1987). TR163-20B and TR163-14 are marked by negative cerium anomalies throughout (Figure 3.6). TR163-20B records relatively constant Ce/Ce* values of ~0.3 for EEP deep waters from the LGM through the early Holocene (Figure 3.6). In contrast, mid-depth core TR163-14 records Ce/Ce* values of ~0.6 during the last glacial with an abrupt decrease at ~13.0 ka to values of ~ 0.4 during the early Holocene. The cerium anomaly shows a strong negative correlation with Mn for mid-depth core TR163-14 whereas Ce/Ce* and Mn are only mildly correlated for deep-water core TR163-20B (Table 3.2).

3.6 Discussion

5.6.1 The Influence of the Panama Basin Geochemical Environment on Foraminiferal Cadmium

The strong correlation between the bulk planktonic Mn and elements associated with Mn-oxides in mid-depth core TR163-14 (2.4 km) suggests that precipitation of Mn-oxides is the dominant source of authigenic Mn at this site. This is unsurprising as Mn-oxides frequently form on foraminifera and trace element cleaning methods have been developed specifically to address their formation (Boyle and Keigwin, 1985/86). Furthermore, formation of Mn-oxides indicates that mid-depth waters remained oxygenated during deglaciation. However, the strong correlation between bulk planktonic Mn and Ce/Ce* suggests that changes in redox potential at this core depth may have begun to overprint the cerium anomaly. Higher Ce/Ce* values during the last glacial indicate that mid-depth oxygenation was likely reduced during the glacial period, although precipitation of Mn-oxides suggests that suboxia was not reached. This is

supported by independent estimates of bottom-water oxygen developed from the carbon isotopic offset between bottom-waters and the pore-water oxic-anoxic boundary using the calibration of Hoogakker et al. (2014) for similar water-depth core TR163-25 (2,650 m). These carbon isotope oxygenation estimates show that waters at 2.65 km depth had significantly lower oxygen concentrations during the last glacial period relative to the Holocene, although suboxic conditions were never reached (Figure 3.6; Hoogakker et al., submitted). The agreement between the Ce/Ce* and δ^{13}C-oxygenation estimates suggests that changes in oxygenation rather than enhanced flux of Ce/Ce*-depleted hydrothermal fluids is driving the changes in cerium anomaly documented for TR163-14. Furthermore, the strong correlation between bulk planktonic Cd and Mn indicates that much of the authigenic Cd was incorporated in the Mn-oxide phase and effective removal of this phase should limit contamination of cleaned benthic foraminiferal Cd/Ca values. Low Mn/Ca values of <100 μmol mol^{-1} have been shown to contribute negligibly to foraminiferal trace element concentrations (Boyle, 1983). The low Mn/Ca values (<100 μmol mol^{-1}) recorded in the cleaned benthic foraminifera from TR163-14 argues that this phase was indeed effectively removed during cleaning and that we can be confident in the measured benthic Cd/Ca values from this core.

In contrast, bulk planktonic samples from deep-water core TR163-20B (3.2 km) are marked by strong correlations between Mn and the trace elements Cr and Li, rather than the strong correlations for Mn and the cerium anomaly along with Mn and the trace elements Co and Ni recorded by TR163-14 (2.36 km). The different trace element associations recorded for TR163-20B bulk planktonic Mn suggest that the authigenic Mn from this core is not influenced by the same processes affecting TR163-14, indicating a

reduced influence of authigenic Mn-oxide formation at the deeper core depth. However, both cleaned benthic Mn/Ca and bulk planktonic authigenic Mn were significantly elevated in TR163-20B. In the Panama Basin, hydrothermal plumes associated with the Galapagos spreading center account for a significant source of Mn below ~2 km water-depth (Klinkhammer, 1980). TR163-20B shows strong correlations between Li and Mn ($r^2 = 0.97$); hydrothermal activity has been proposed as an important source of Li (Hodkinson et al., 1994) with high concentrations of Li reported for hydrothermal-Mn crusts (Glasby et al., 1997). Thus, the close link between bulk planktonic Mn and Li in TR163-20B could indicate a hydrothermal-Mn contribution. However, riverine flux and alteration of basalts are also important sources and sinks of Li to sediments (Elderfield and Schultz, 1996) and high concentrations of Li do not unequivocally confirm a hydrothermal source.

The flux of hydrothermal-Mn to the sediments and Mn-oxide reduction within the sediments contribute to shallow sedimentary enrichments of Mn(II) which is rapidly removed by mixed Mn-Ca carbonate phases (Pedersen and Price 1982). The tendency of mixed Mn-Ca carbonate phases to form overgrowths on foraminiferal shells has been documented in the Panama basin (Boyle, 1983; Pena et al., 2005, 2008). These conditions likely contribute to the elevated Mn/Ca recorded in TR163-20B benthic foraminifera even after aggressive cleaning treatments. Despite the inability to decrease TR163-20B benthic foraminiferal Mn/Ca, the low correlation between bulk planktonic authigenic Mn and Cd concentrations ($r^2 = 0.5$; Table 3.2) suggests that this cleaning-resistant phase was potentially not an important source of Cd contamination to TR163-20B benthic foraminiferal Cd/Ca values, allowing a larger benthic Mn/Ca contamination threshold of

1000 μmol mol^{-1} for this core. Conversely, correlations for TR163-14 between bulk planktonic foraminiferal Mn and trace element indicators for changing redox conditions (Co, Ni, Ce/Ce*) suggest that authigenic Mn was likely in the form of Mn-oxide coatings, which have a larger potential for Cd-contamination if not successfully removed. This required a lower benthic foraminiferal Mn/Ca contamination threshold of 100 μmol $mol^{-1}$for TR163-14.

5.6.2 Glacial-Interglacial Deep-Water Changes and Carbon Remineralization

Eastern Equatorial Pacific Cd_W was not significantly different during the Holocene and LGM with the exception of increased glacial Cd_W at ~2.0-2.5 km water depth (Figure 3.4). Recent water column measurements of [Cd] and $\delta^{114}Cd$ paired with phosphate concentrations suggest decoupling of Cd and phosphate in low oxygen regions as a result of Cd-sulfide (CdS) precipitation (Janssen et al., 2014). Benthic foraminiferal carbon isotopic estimates of oxygenation indicate that mid-depth waters in the EEP were poorly oxygenated (~55 μmol kg^{-1}) during the last glacial period (Hoogakker et al., submitted). Similarly, the REE and trace element results from TR163-14 suggest that oxygen concentrations at 2.37 km water depth were also reduced during the last glacial period (Figure 3.6). Increased CdS precipitation under reduced oxygen concentrations could account for the increased glacial Cd_W values and enhanced variability recorded at water depths of ~2.0-2.5 km. However, our REE and trace element results indicate that these waters did not become suboxic, and oxygen concentrations may not have been sufficiently low for the formation of Cd-sulfides.

Alternatively, a mid-depth Cd_W maximum during the LGM could reflect increased phosphate concentrations as predicted by the "nutrient deepening" hypothesis

which suggests a transfer of nutrients and CO_2 from intermediate and mid-depth waters to deep, abyssal waters under a more efficient biological pump (Boyle, 1988). However, rather than a transfer of nutrients and/or respired CO_2 to abyssal waters (Boyle, 1988; Jaccard et al., 2009), we suggest that respired carbon accumulated in mid-depth waters due to both decreased mid-depth ventilation (Burke et al., 2015; Fuente et al., 2015; Ronge et al., 2016; Umling and Thunell, 2017) and a more efficient biological pump (Gottschalk et al., 2016; Hertzburg et al., 2016; Umling and Thunell, submitted). Similar Cd_W enrichments and increased variability have also been documented at ~1.0-1.5 km water depth in the Sub-Antarctic Pacific (Lynch-Stieglitz et al., 1996). These water-depths are within the pathway of Upper Circumpolar Deep Water (UCDW) which was also marked by reduced ventilation during the last glacial period (Burke and Robinson, 2012).

However, a shift in the source areas and mixing of the deep and mid-depth water masses in this region could also contribute to changes in nutrient content. The combined $\delta^{13}C$ and Cd_W results from 2.65 to 3.2 km water depth are useful for disentangling signatures of water mass mixing and nutrient content (Figure 3.7). TR163-20B (3.2 km) lies close to the modern boundary between northward flowing Lower Circumpolar Deep Water (LCDW) and the return flow of Pacific Deep Water (PDW). The Cd_W- $\delta^{13}C$ results from TR163-20B suggest increased influence of the air-sea fractionation of $\delta^{13}C$ during the glacial-interglacial transition, from glacial $\delta^{13}C_{as}$ values approaching -1‰ to deglacial $\delta^{13}C_{as}$ values close to 0‰. A $\delta^{13}C_{as}$ value of 0‰ indicates that the influence of air-sea exchange is equal to the air-sea signature of mean ocean water, whereas positive (negative) values indicate a larger (lower) influence of air-sea exchange relative to mean

ocean water (Lynch-Stieglitz et al., 1995). The air-sea signature is imparted on a water-mass at the surface-region of water-mass formation, with the $\delta^{13}C_{as}$ value recorded by cores along the ventilation pathway reflecting mixing among water-masses with differing air-sea signatures (Lynch-Stieglitz et al., 1995). Because TR163-20B falls close to a boundary between two water masses, a shift in the documented $\delta^{13}C_{as}$ suggests movement of that boundary. Reduced TR163-20B glacial $\delta^{13}C_{as}$ values are consistent with increased influence of LCDW during the last glacial period and a shoaling of the boundary between LCDW and PDW. A similar glacial-deglacial $\delta^{13}C_{as}$ increase is recorded at 2.7 km water-depth (TR163-23), along with an additional $\delta^{13}C_{as}$ increase of 1‰ from the deglaciation to the Holocene (Figure 3.7). This additional 1‰ deglacial-Holocene increase in $\delta^{13}C_{as}$ may also be reflected in TR163-20B, however this core does not have sufficient Holocene sampling to address this shift. In contrast, TR163-25 (2.6 km) does not record $\delta^{13}C_{as}$ values values close to -1‰. The recorded shift in $\delta^{13}C_{as}$ values by TR163-23 and TR163-20B but not TR163-25, suggests that the upper boundary of southern sourced LCDW was positioned at ~2.6-2.7 km during the last glacial period. The combined Cd_W and $\delta^{13}C$ data for both TR163-23 and TR163-25 suggests increased remineralization during the last glacial (Figure 3.7). These results indicate that the LCDW-PDW boundary likely shoaled during the LGM in conjunction with increased respired carbon storage in mid-depth PDW.

3.7 Conclusions

The Panama Basin has a complex geochemical environment due to venting of hydrothermal fluids to deep-waters (Klinkhammer et al., 1977; Marchig et al., 1985), subaerial and submarine volcanism (Kowsman, 1973; Lea et al., 2005), varying water

column redox conditions, and high surface productivity (Pennington et al., 2006). Each of these processes can impact foraminiferal trace element chemistry to varying extents, but their impact is spatially variably throughout the basin. Formation of manganese-oxides has the potential for increasing the foraminiferal Cd/Ca values, but Mn/Ca values <100 μmol mol^{-1} have been shown to contribute negligibly to Cd/Ca indicating successful removal of Mn-oxide contamination (Boyle, 1983; Boyle and Keigwin, 1985/86). Our authigenic trace element results from bulk planktonic foraminifera, suggest that Mn coatings are unlikely to be a significant contributor to the Cd/Ca values of the cleaned benthic foraminifera samples.

Our paired Cd/Ca and $\delta^{13}C$ records are consistent with respired carbon accumulation in mid-depth waters along with an expansion of Lower Circumpolar Deep Water. This supports an increased influence of southern sourced waters during periods of increased sea-ice extent and/or stratification. The hypothesized reorganization of overturning circulation required to drive the expansion of southern-sourced deep-waters resulted in decreased communication between upper and lower branches of Southern Ocean overturning circulation (Ferrari et al., 2014) thereby decreasing mid-depth ventilation (Burke et al., 2015). Decreased glacial ventilation would have allowed accumulation of respired carbon in mid-depth waters while a more efficient glacial biological pump would have decreased the CO_2 "leak" to the atmosphere. A resumption of ventilation during deglaciation in conjunction with a less efficient biological pump would have released the respired carbon reservoir to shallow surface waters and the atmosphere. Our results suggest that variability in both ventilation and biological pump

efficiency are important mechanisms for the glacial-interglacial transfer of CO_2 between the oceans and atmosphere.

Table 3.1 Eastern and western equatorial Pacific core locations, depths, and references.

Eastern Equatorial Pacific cores				
Core	**Latitude**	**Longitude**	**Core depth**	**reference**
V19-27	0.47	-82.07	1373	Boyle, 1992
TR163-2	8.24	-84.35	1620	this study
V17-42	3.53	-81.18	1841	Boyle, 1992
TR163-18	2.81	-89.85	2030	this study
TR163-14	3.91	-87.24	2365	this study
TR163-25	-1.65	-88.45	2650	this study
V19-28	-2.37	-84.85	2720	Boyle, 1992
TR163-23	0.41	-92.16	2730	this study
V19-30	-3.38	-82.35	3071	Boyle, 1988, 1992
TR163-20B	0.79	-93.84	3200	this study
TR163-31B	-3.62	-83.97	3210	Boyle, 1988
RC10-65	-0.68	-108.62	3588	Boyle, 1988
KNR73-3	0.37	-106.18	3606	Boyle, 1988, 1992
KNR73-4	10.85	-110.27	3681	Boyle, 1988, 1992
Western Equatorial Pacific cores				
Core	**Latitude**	**Longitude**	**Core depth**	**reference**
V32-159	48.67	147.4	1235	Boyle, 1992
V32-161	48.28	149.07	1600	Boyle, 1992
V28-235	-5.45	160.48	1748	Boyle, 1992
V24-109	0.43	158.8	2367	Boyle, 1988
V26-304	28.53	134.13	2942	Boyle, 1992
Rama 44	53.01	164.65	2980	Boyle, 1992
V28-238	1.02	160.48	3120	Boyle, 1992
V32-128a	36.47	177.17	3623	Boyle, 1992
V32-128b	35.32	174.9	3870	Boyle, 1992

Table 3.2 Pearson correlation coefficients of bulk planktonic authigenic Mn and Cd

	Li	Al	Ca	Ti	V	Cr	Mn	Fe	Co	Ni	Cu	U	Ce/Ce*
Cd	-0.19	-0.03	0.45	-0.16	0.39	-0.57	**0.94****	0.43	**0.96****	**0.93****	-0.11	-0.39	**-0.82***
	0.5	-0.53	**0.84***	-0.49	0.56	-0.28	0.5	-0.5	**0.64**	**0.95****	-0.25	**0.9 ***	-0.14
Mn	-0.32	0.04	0.46	-0.11	0.42	**-0.67**		0.55	**0.9 ****	**0.88 ***	0.31	0.52	**-0.92 ****
	0.97**	-0.58	**0.74**	-0.14	0.12	**-0.8***		-0.35	0.19	**0.61**	-0.39	**0.62**	**-0.65**

Bold font indicates a moderately strong correlation (>0.6) and filled background indicates a strong correlation (>0.8).
Correlation coefficients for TR163-14 are indicated in blue and in red for TR163-20B.
* Statistically significant ($p < 0.05$)
** Highly statistically significant ($p < 0.001$)

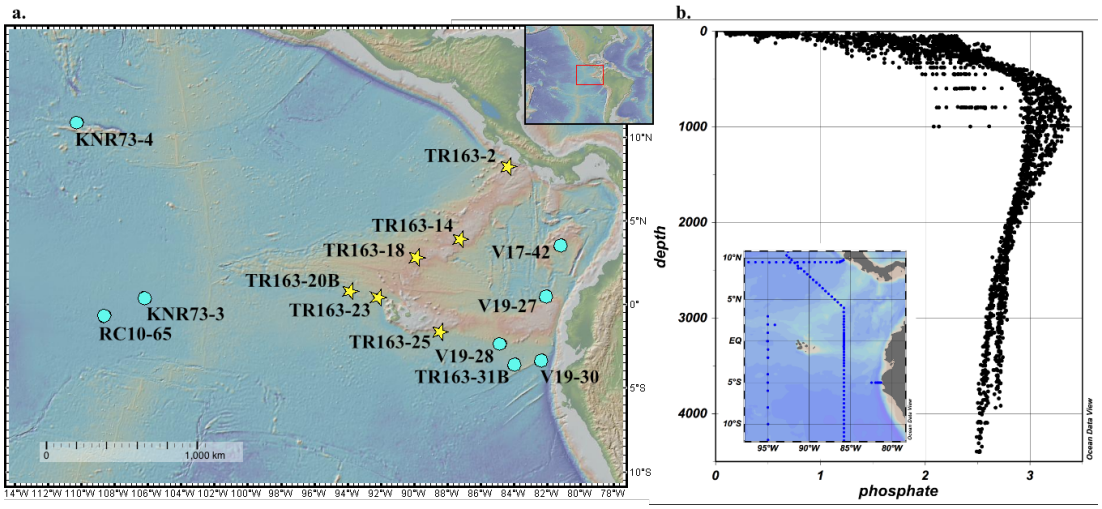

Figure 3.1 **(a)** The location of eastern equatorial Pacific benthic foraminiferal Cd_W records from this study (stars) and Boyle (1988, 1992; circles). **(b)** Phosphate and cadmium are closely linked in the modern ocean, with a phosphate maximum occurring at ~1.0 km in the water column (Key et al., 2004).` Water column cadmium concentrations are estimated from seawater phosphate concentrations following Boyle (1992).

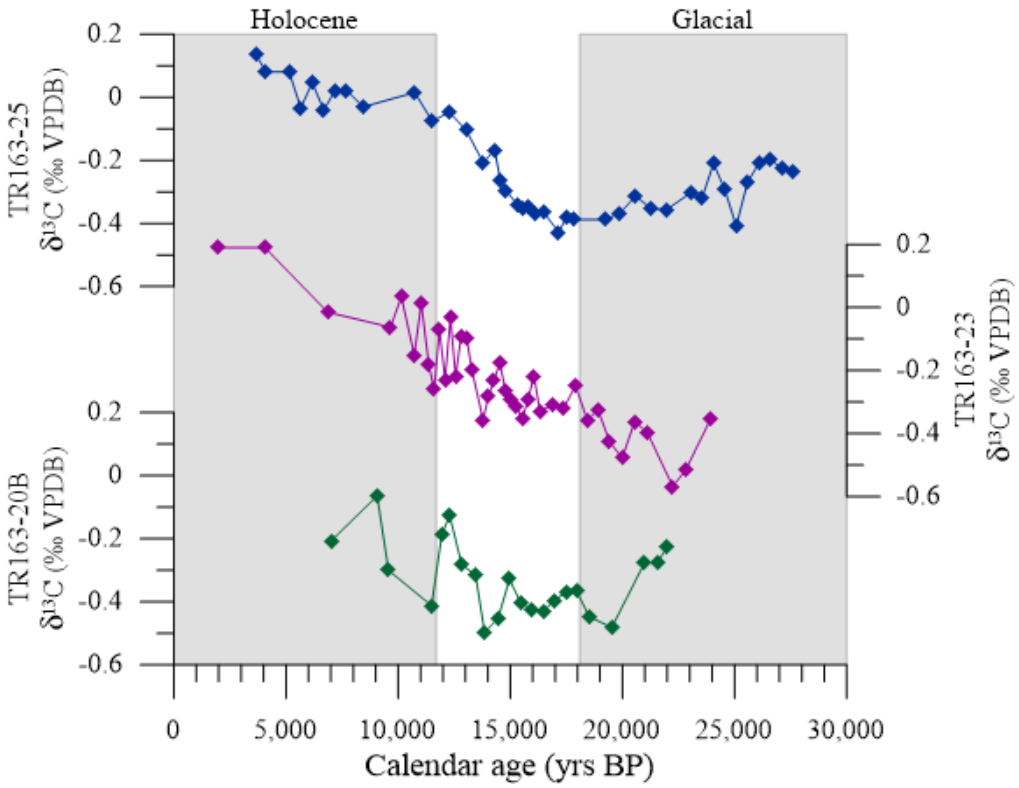

Figure 3.2 Benthic foraminiferal carbon isotopic composition of *C. wuellerstorfi* for cores TR163-25 (2.65 km), TR163-23 (2.73 km), and TR163-20B (3.20 km).

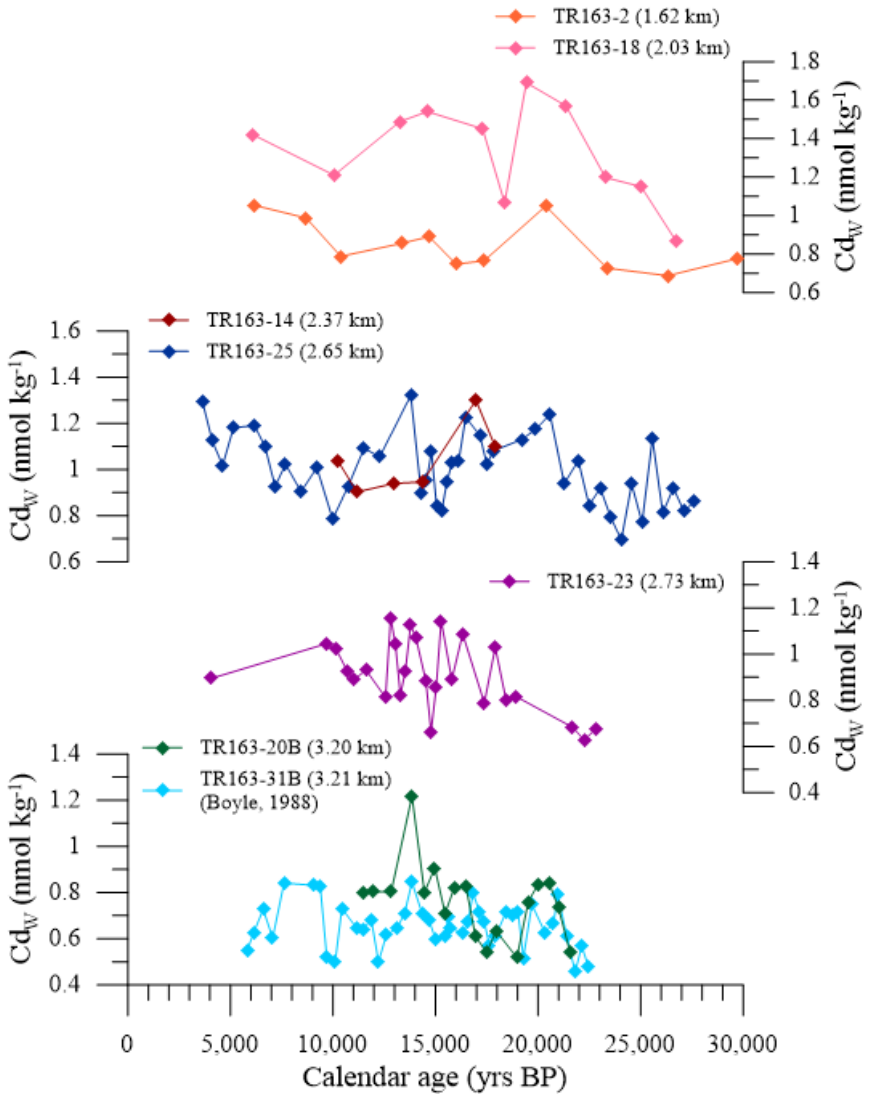

Figure 3.3 Seawater Cadmium (Cd_W) has been estimated for TR163 cores from the Cd/Ca values of *C. wuellerstorfi* and *C. mundulus* (only TR163-2). A new age model for TR163-31B was estimated using the Bayesian age-depth modeling program BACON (Blaauw and Christen, 2011) to calibrate the *N. dutertrei* radiocarbon ages of Shackleton et al. (1988) utilizing variable reservoir ages reported in Umling and Thunell (2017).

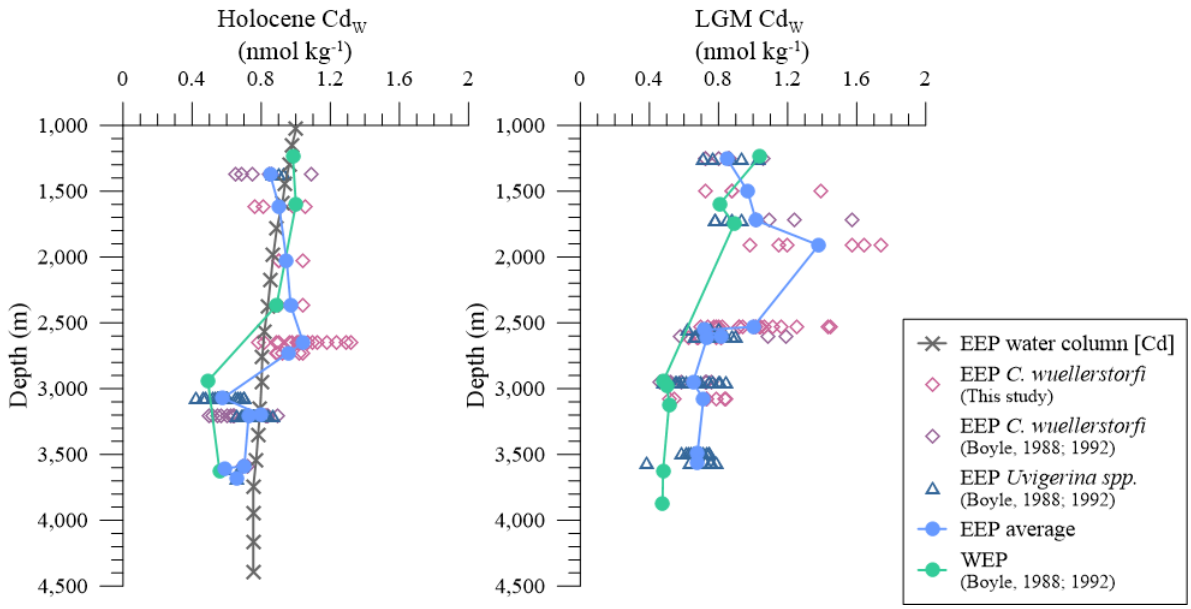

Figure 3.4 Average eastern equatorial Pacific Holocene and LGM Cd_W were estimated for a transect of cores from 1.37-3.68 km water-depth using the Cd/Ca data of this study and Boyle (1988, 1992). Eastern equatorial Pacific water column Cd was estimated from GLODAP station 1894 phosphate (Key et al., 2004) using the relationship Cd(nmol kg^{-1})=0.4*P(µmol kg^{-1})-0.25 from Boyle (1988). Water depths for the last glacial maximum have been adjusted by 120 m to account for lower sea-levels.

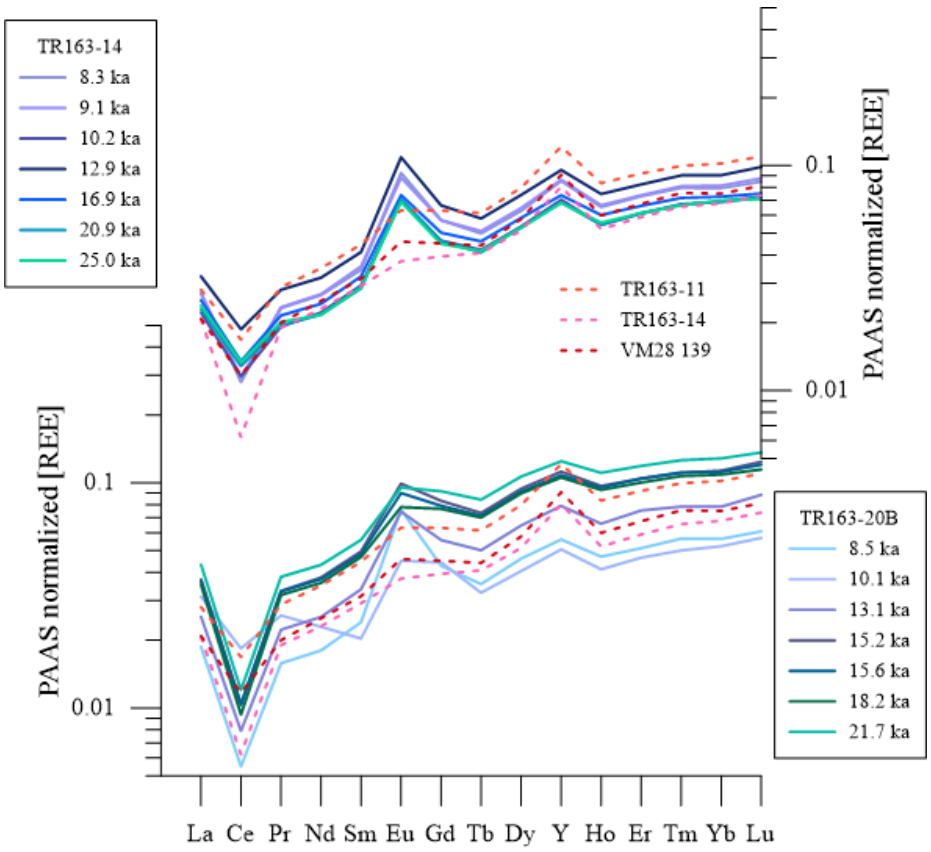

Figure 3.5 The PAAS-normalized distribution of rare earth elements at 2.37 km (TR163-14) and 3.2 km (TR163-20B) compared to published eastern equatorial Pacific core top data from cores TR163-11, TR163-14 and VM28-139 (Osborne et al., 2017).

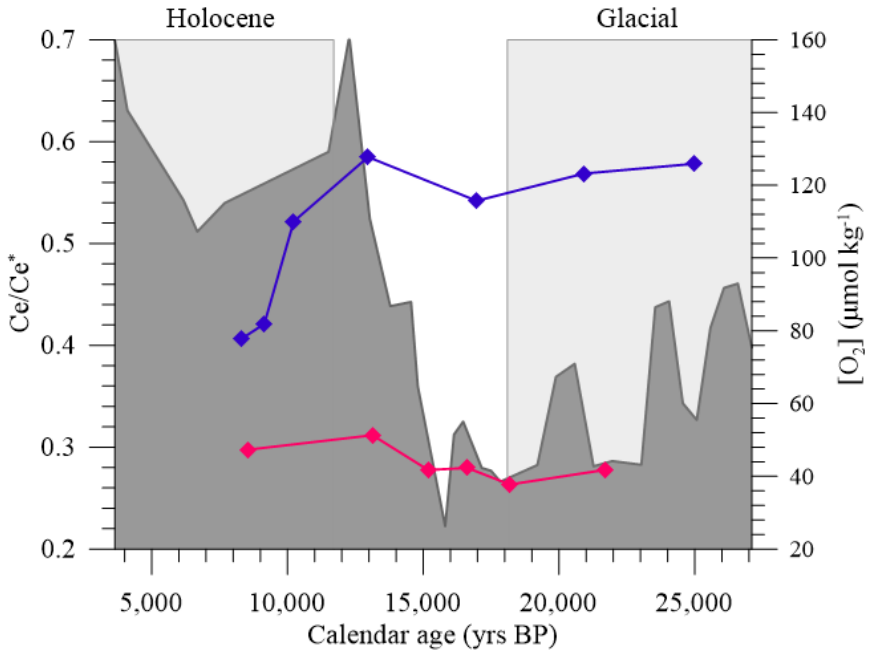

Figure 3.6 The estimated cerium anomalies (Ce/Ce^*) for mid-depth (TR163-14; 2.37 km; blue) and deep-waters (TR163-20B; 3.20 km; red) over the last glacial-interglacial transition. An abrupt shift in the mid-depth Ce/Ce^* value at ~13 ka coincides with increasing mid-depth oxygenation based on benthic foraminiferal $\Delta\delta^{13}C$ (TR163-25; 2.65 km; dark grey; Hoogakker et al., submitted).

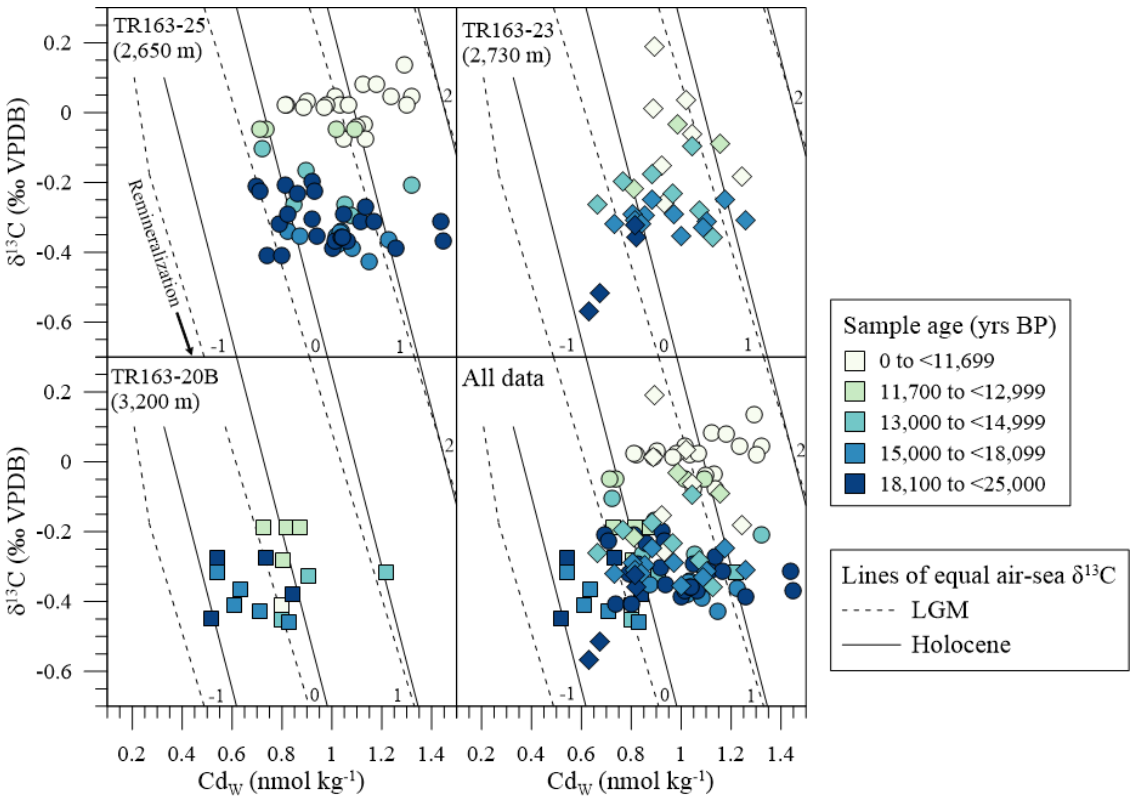

Figure 3.7 Benthic foraminiferal Cd_w values versus $\delta^{13}C$ for three TR163 cores. Lines of equal $\delta^{13}C_{as}$ were plotted following Lynch-Steiglitz et al. (1995, 1996), accounting for the change in Cd-P slope at P=1.3 μmol kg^{-1} (Boyle, 1988) following Oppo and Horowitz (2000).

IMPLICATIONS AND FUTURE DIRECTIONS

A growing body of literature has sought to explain the CO_2 increases of the last glacial-interglacial transition. However, much of the previous research has presented conflicting evidence for mechanisms of oceanic-atmospheric CO_2 exchange (Broecker and Barker, 2007; Calvo et al., 2011; François et al., 1997; Freeman et al., 2015; Hertzberg et al., 2016; Lund et al., 2016; Okazaki et al., 2010; Pichevin et al., 2009; Rae et al., 2014; Stott et al., 2009; Ziegler et al., 2013). The research presented in this study investigated these inconsistencies and documented the role of the eastern equatorial Pacific in the CO_2 change during the last glacial-interglacial transition. By recording changes in deep ocean chemistry and circulation, this study was able to assess both physical and biological mechanisms of oceanic-atmospheric CO_2 exchange.

Chapter one presented evidence for two pulses of gradually increasing ventilation recorded synchronously in both thermocline and mid-depth waters. This finding suggests that during deglaciation, the EEP was a source of CO_2 to the atmosphere much as it is today. By reconciling the influence of a changing reservoir age with the disagreement among ventilation records, chapter one was further able to examine regional trends in ventilation and demonstrate that both Atlantic and Pacific deglacial ventilation occurred synchronously. Additionally, these results indicate that the Southern Ocean recorded an earlier ventilation onset, suggesting a Southern Ocean driver of deglacial ocean ventilation that then propagated northward into both the Pacific and Atlantic Oceans. The

findings of chapter one point to decreased mid-depth ventilation as a possible driver of glacial oceanic CO_2 storage. This is a key departure from the earlier predictions of an isolated abyssal reservoir (Broecker and Barker, 2007), consistent with respired carbon storage in mid-depth rather than deep waters.

However, the radiocarbon content recorded in mid-depth and deep waters can be impacted by processes other than decreased ventilation (Lund et al., 2016). Chapter two investigates whether respired carbon storage did indeed occur in tandem with periods of decreased mid-depth radiocarbon content. If decreased glacial ventilation rates resulted in respired carbon storage, then deep-water oxygenation would be expected to decline accordingly due to increased respiration. Similarly, elevated respired carbon concentrations would result in a decline in carbonate saturation. Results from chapter two indicate that mid-depth oxygen and carbonate ion concentrations were lower during the last glacial period, confirming that glacial decreases in ventilation rate resulted in the accumulation of respired carbon in mid-depth waters. Additionally, the synchronous shifts in ventilation and indicators of the biological pump suggest that both decreased ventilation and a more efficient biological pump worked to sequester CO_2 during the last glacial period and resulted in evasion of a respired carbon reservoir to the atmosphere during deglaciation.

While the EEP records of ventilation and the biological pump tell a consistent story, there are still gaps in the understanding of the mechanisms that may have driven these changes. Chapter three attempts to uncover the role that circulation and water-mass mixing may have played in glacial-interglacial ventilation and biological pump variability by characterizing changes in deep and mid-depth water masses of the EEP. Results from

chapter three suggest that the boundary between northward-flowing Lower Circumpolar Deep Water (LCDW) and its southward return-flow as Pacific Deep Water (PDW), likely shoaled during the last glacial period. This is consistent with a northward shift and shoaling of the lower and upper branches of Southern Ocean overturning circulation in response to changes in buoyancy forcing driven by Southern Ocean sea-ice extent (Ferrari et al., 2014; Watson et al., 2015).

Together, these findings point to a Southern-Ocean driver of changes in ventilation and the biological pump, possibly as a result of increased Antarctic sea ice extent. However, there are still gaps in our understanding of the processes at work during this period and the oceanic participation in some of the rapid centennial-scale increases in atmospheric CO_2. Specifically, Antarctic Intermediate Water (AAIW) has been suggested as the deglacial ventilation pathway for transfer of the mid-depth respired carbon reservoir into shallow waters and the atmosphere. While evidence of radiocarbon-depleted waters has been found in regions sourced by AAIW (Marchitto et al., 2007; Lindsay et al., 2015), evidence for radiocarbon-depletions in the regions where AAIW is being formed has proved more elusive (Rose et al., 2010; Hines et al., 2016). Results from this study (Chapter 1) and boron isotopic pH estimates (Kubota et al., 2014; Martínez-Botí et al., 2015) suggest that the eastern equatorial Pacific was a deglacial source of CO_2 to the atmosphere. However, this CO_2 could have been brought to surface waters by direct ventilation from below or it could have entered the region with the transport of mainly southern-sourced Equatorial Undercurrent (EUC) waters. Future studies should focus on locating the intermediate water pathway that transfers carbon from mid-depth to shallow water-depths. In particular, radiocarbon studies of cores from

western equatorial Pacific EUC waters could shed light on whether the EUC was indeed a source of radiocarbon-depleted waters to the surface waters of the EEP or alternately, whether CO_2 in the EEP was ventilated directly from underlying mid-depth waters. Similarly, the absence of radiocarbon-depletions in regions of AAIW formation could result from a shift in the location of AAIW formation during the last glacial period. Evidence from studies of biogenic opal flux suggest that regions of Southern Ocean upwelling and diatom productivity were located further north during the last glacial period as a result of increased Antarctic sea-ice extent (Anderson et al., 2009). A similar northward shift in the location of AAIW formation would not be unexpected.

In addition to locating the intermediate water pathway for deglacial ventilation of the mid-depth respired carbon reservoir, future studies are needed to determine the oceanic role in the rapid atmospheric CO_2 increases at 11.7 and 16.3 ka (Marcott et al., 2014). While this study (Chapter 1) reveals a close connection between rapid ventilation of a mid-depth respired carbon reservoir and increasing CO_2 at 14.8 ka, there were not sufficient benthic formaniniferal radiocarbon dates close to 11.7 and 16.3 ka to conclusively establish the role of oceanic CO_2 to these atmospheric increases in CO_2. Furthermore, many previously developed deglacial ventilation records have poor sampling resolution during the Younger Dryas period. This study (Chapter 1) and a few studies from the North Atlantic (Robinson et al., 2005; Thornalley et al., 2011; Skinner et al., 2014) and East Pacific (Marchitto et al., 2007; Lindsay et al., 2015) record a period of reduced ventilation during the Younger Dryas. However, Younger Dryas radiocarbon depletions are not recorded in all deglacial ventilation records (Burke and Robinson, 2012; Chen et al., 2015; Fuente et al., 2015; Rae et al., 2014; Skinner et al., 2010). In

many cases this is likely a product of poor sampling resolution during this period, but more extensive investigation is required to determine the regional extent of decreased ventilation at this time.

The results presented in this study provide important insights into changes in ventilation, oxygenation, carbonate saturation, and circulation during the last deglaciation in the eastern equatorial Pacific. These observations have strong implications for the role of the Southern Ocean in controlling glacial-interglacial CO_2 exchange between the oceans and the atmosphere. Furthermore, this work demonstrates that respired carbon was stored in mid-depth waters during the last glacial period and released to the atmosphere with pulses of increased deglacial ventilation. More broadly, this research has given rise to several pathways of future research and further investigation of the role of the oceans in modifying climate on glacial-interglacial timescales. We hope that this research will serve as a basis for future studies of glacial respired carbon storage and the subsequent deglacial transfer of carbon from the oceans to the atmosphere.

REFERENCES

Allen, K. A., E. L. Sikes, B. Hönisch, A. C. Elmore, T. P. Guilderson, Y. Rosenthal, and R. F. Anderson (2015), Southwest Pacific deep water carbonate chemistry linked to high southern latitude climate and atmospheric CO_2 during the Last Glacial Termination, *Quat. Sci. Rev.*, *122*, 180–191, doi:10.1016/j.quascirev.2015.05.007.

Anderson, R. F., S. Ali, L. I. Bradtmiller, S. H. H. Nielsen, M. Q. Fleisher, B. E. Anderson, and L. H. Burckle (2009), Wind-Driven Upwelling in the Southern Ocean and the Deglacial Rise in Atmospheric CO_2, *Science*, *323*(5920), 1443–1448, doi:10.1126/science.1167441.

Anderson, R. F., Z. Chase, M. Q. Fleisher, and J. Sachs (2002), The Southern Ocean's biological pump during the Last Glacial Maximum, *Deep-Sea Res.*, *49*(9–10), 1909–1938, doi:10.1016/S0967-0645(02)00018-8.

Balistrieri, L. S., and J. W. Murray (1986), The surface chemistry of sediments from the Panama Basin: The influence of Mn oxides on metal adsorption, *Geochim. Cosmochim. Ac.*, *50*(10), 2235–2243, doi:10.1016/0016-7037(86)90078-5.

Balmer, S., M. Sarnthein, M. Mudelsee, and P. M. Grootes (2016), Refined modeling and ^{14}C plateau tuning reveal consistent patterns of glacial and deglacial ^{14}C reservoir ages of surface waters in low-latitude Atlantic, *Paleoceanography*, *31*(8), 1030–1040, doi:10.1002/2016PA002953.

Barker, S., M. Greaves, and H. Elderfield (2003), A study of cleaning procedures used for foraminiferal Mg/Ca paleothermometry, *Geochem. Geophys. Geosyst.*, *4*(9), 8407, doi:10.1029/2003GC000559.

Bauska, T. K., D. Baggenstos, E. J. Brook, A. C. Mix, S. A. Marcott, V. V. Petrenko, H. Schaefer, J. P. Severinghaus, and J. E. Lee (2016), Carbon isotopes characterize rapid changes in atmospheric carbon dioxide during the last deglaciation, *Proc. Natl. Acad. Sci. USA.*, *113*(13), 3465–3470, doi:10.1073/pnas.1513868113.

Bereiter, B., S. Eggleston, J. Schmitt, C. Nehrbass-Ahles, T. F. Stocker, H. Fischer, S. Kipfstuhl, and J. Chappellaz (2015), Revision of the EPICA Dome C CO_2 record from 800 to 600 kyr before present: Analytical bias in the EDC CO2 record, *Geophys. Res. Lett.*, *42*(2), 542–549, doi:10.1002/2014GL06195

Blaauw, M., and J. A. Christen (2011), Flexible paleoclimate age-depth models using an autoregressive gamma process, *Bayesian Anal.*, *6*(3), 457–474, doi:10.1214/11-BA618.

Blaauw, M., J. A. Christen, D. Mauquoy, J. van der Plicht, and K. D. Bennett (2007), Testing the timing of radiocarbon-dated events between proxy archives, *Holocene*, *17*(2), 283–288, doi:10.1177/0959683607075857.

Boiteau, R., M. Greaves, and H. Elderfield (2012), Authigenic uranium in foraminiferal coatings: A proxy for ocean redox chemistry, *Paleoceanography*, *27*(3), PA3227, doi:10.1029/2012PA002335.

Boyle, E. A., and L. D. Keigwin (1985), Comparison of Atlantic and Pacific paleochemical records for the last 215,000 years: changes in deep ocean circulation and chemical inventories, *Earth Planet. Sci. Lett.*, *76*(1–2), 135–150, doi:10.1016/0012-821X(85)90154-2.

Boyle, E. A., and Y. Rosenthal (1996), Chemical hydrography of the South Atlantic during the last glacial maximum: Cd vs. $\delta^{13}C$, in *The South Atlantic: Present and Past Circulation*, pp. 423–443, Springer-Verlag.

Broecker, W., S. Barker, E. Clark, I. Hajdas, G. Bonani, and L. Stott (2004), Ventilation of the Glacial Deep Pacific Ocean, *Science*, *306*(5699), 1169–1172, doi:10.1126/science.1102293.

Broecker, W., and S. Barker (2007), A 190‰ drop in atmosphere's $\Delta^{14}C$ during the "Mystery Interval" (17.5 to 14.5 kyr), *Earth Planet. Sci. Lett.*, *256*(1–2), 90–99, doi:10.1016/j.epsl.2007.01.015.

Broecker, W., E. Clark, and S. Barker (2008), Near constancy of the Pacific Ocean surface to mid-depth radiocarbon-age difference over the last 20 kyr, *Earth Planet. Sci. Lett.*, *274*(3–4), 322–326, doi:10.1016/j.epsl.2008.07.035.

Broecker, W. S., and T.-H. Peng (1987), The role of $CaCO_3$ compensation in the glacial to interglacial atmospheric CO_2 change, *Glob. Biogeochem. Cy.*, *1*(1), 15–29, doi:10.1029/GB001i001p00015.

Bronk Ramsey, C. et al. (2012), A Complete Terrestrial Radiocarbon Record for 11.2 to 52.8 kyr B.P., *Science*, *338*(6105), 370–374, doi:10.1126/science.1226660.

Burke, A., and L. F. Robinson (2012), The Southern Ocean's Role in Carbon Exchange During the Last Deglaciation, *Science*, *335*(6068), 557–561, doi:10.1126/science.1208163.

Burke, A., A. L. Stewart, J. F. Adkins, R. Ferrari, M. F. Jansen, and A. F. Thompson (2015), The glacial mid-depth radiocarbon bulge and its implications for the overturning circulation, *Paleoceanography*, *30*(7), 1021–1039, doi:10.1002/2015PA002778.

Calvo, E., C. Pelejero, L. D. Pena, I. Cacho, and G. A. Logan (2011), Eastern Equatorial Pacific productivity and related-CO_2 changes since the last glacial period, *Proc. Natl. Acad. Sci. USA.*, *108*(14), 5537–5541, doi:10.1073/pnas.1009761108.

Chen, T., L. F. Robinson, A. Burke, J. Southon, P. Spooner, P. J. Morris, and H. C. Ng (2015), Synchronous centennial abrupt events in the ocean and atmosphere during the last deglaciation, *Science*, *349*(6255), 1537–1541, doi:10.1126/science.aac6159.

Cook, M. S., and L. D. Keigwin (2015), Radiocarbon profiles of the NW Pacific from the LGM and deglaciation: Evaluating ventilation metrics and the effect of uncertain surface reservoir ages: Northwest Pacific radiocarbon, *Paleoceanography*, *30*(3), 174–195, doi:10.1002/2014PA002649.

Costa, K. M., A. W. Jacobel, J. F. McManus, R. F. Anderson, G. Winckler, and N. Thiagarajan (2017), Productivity patterns in the equatorial Pacific over the last 30,000 years: Productivity in the Equatorial Pacific, *Glob. Biogeochem. Cy.*, doi:10.1002/2016GB005579.

Crichton, K. A., N. Bouttes, D. M. Roche, J. Chappellaz, and G. Krinner (2016), Permafrost carbon as a missing link to explain CO_2 changes during the last deglaciation, *Nat. Geosci.*, *9*(9), 683–686, doi:10.1038/ngeo2793.

Curry, W. B., J. C. Duplessy, L. D. Labeyrie, and N. J. Shackleton (1988), Changes in the distribution of $\delta^{13}C$ of deep water ΣCO_2 between the Last Glaciation and the Holocene, *Paleoceanography*, *3*(3), 317–341, doi:10.1029/PA003i003p00317.

De Pol-Holz, R., L. Keigwin, J. Southon, D. Hebbeln, and M. Mohtadi (2010), No signature of abyssal carbon in intermediate waters off Chile during deglaciation, *Nat. Geosci.*, *3*(3), 192–195, doi:10.1038/ngeo745.

Dickson, A. G. (1990), Thermodynamics of the dissociation of boric acid in synthetic seawater from 273.15 to 318.15 K, *Deep-Sea Res.*, *37*(5), 755–766, doi:10.1016/0198-0149(90)90004-F.

Dickson, A. G., and F. J. Millero (1987), A comparison of the equilibrium constants for the dissociation of carbonic acid in seawater media, *Deep-Sea Res.*, *34*(10), 1733–1743, doi:10.1016/0198-0149(87)90021-5.

Druffel, E. R. M., S. Griffin, S. R. Beaupré, and R. B. Dunbar (2007), Oceanic climate and circulation changes during the past four centuries from radiocarbon in corals, *Geophys. Res. Lett.*, *34*(9), doi:10.1029/2006GL028681.

Dubois, N., M. Kienast, S. S. Kienast, and A. Timmermann (2014), Millennial-scale Atlantic/East Pacific sea surface temperature linkages during the last 100,000 years, *Earth Planet. Sci. Lett.*, *396*, 134–142, doi:10.1016/j.epsl.2014.04.008.

Elderfield, H., and M. J. Greaves (1982), The rare earth elements in seawater, *Nature*, *296*(5854), 214–219, doi:10.1038/296214a0.

Elderfield, H., and A. Schultz (1996), Mid-Ocean Ridge Hydrothermal Fluxes and the Chemical Composition of the Ocean, *Ann. Rev. Earth Planet. Sci.*, *24*(1), 191–224, doi:10.1146/annurev.earth.24.1.191.

Ferrari, R., M. F. Jansen, J. F. Adkins, A. Burke, A. L. Stewart, and A. F. Thompson (2014), Antarctic sea ice control on ocean circulation in present and glacial climates, *Proc. Natl. Acad. Sci. USA.*, *111*(24), 8753–8758, doi:10.1073/pnas.1323922111.

Fiedler, P. C., and L. D. Talley (2006), Hydrography of the eastern tropical Pacific: A review, *Prog. Oceanogr.*, *69*(2-4), 143–180, doi:10.1016/j.pocean.2006.03.008.

François, R., M. A. Altabet, E.-F. Yu, D. M. Sigman, M. P. Bacon, M. Frank, G. Bohrmann, G. Bareille, and L. D. Labeyrie (1997), Contribution of Southern Ocean surface-water stratification to low atmospheric CO_2 concentrations during the last glacial period, *Nature*, *389*, 929–935, doi:10.1038/40073.

Freeman, E., L. C. Skinner, A. Tisserand, T. Dokken, A. Timmermann, L. Menviel, and T. Friedrich (2015), An Atlantic–Pacific ventilation seesaw across the last deglaciation, *Earth Planet. Sci. Lett.*, *424*, 237–244, doi:10.1016/j.epsl.2015.05.032.

de la Fuente, M., L. Skinner, E. Calvo, C. Pelejero, and I. Cacho (2015), Increased reservoir ages and poorly ventilated deep waters inferred in the glacial Eastern Equatorial Pacific, *Nat. Commun.*, *6*, 7420, doi:10.1038/ncomms8420.

Galbraith, E. D., E. Y. Kwon, D. Bianchi, M. P. Hain, and J. L. Sarmiento (2015), The impact of atmospheric pCO_2 on carbon isotope ratios of the atmosphere and ocean, *Glob. Biogeochem. Cy.*, *29*(3), 307–324, doi:10.1002/2014GB004929.

German, C. R., and H. Elderfield (1990), Application of the Ce anomaly as a paleoredox indicator: The ground rules, *Paleoceanography*, *5*(5), 823–833, doi:10.1029/PA005i005p00823.

Glasby, G. P., D. Stüben, G. Jeschke, P. Stoffers, and C.-D. Garbe-Schönberg (1997), A model for the formation of hydrothermal manganese crusts from the Pitcairn Island hotspot, *Geochim. Cosmochim. Ac.*, *61*(21), 4583–4597, doi:10.1016/S0016-7037(97)00262-7.

Gottschalk, J., L. C. Skinner, J. Lippold, H. Vogel, N. Frank, S. L. Jaccard, and C. Waelbroeck (2016), Biological and physical controls in the Southern Ocean on past millennial-scale atmospheric CO_2 changes, *Nat. Commun.*, *7*, 11539, doi:10.1038/ncomms11539.

Hain, M. P., D. M. Sigman, and G. H. Haug (2011), Shortcomings of the isolated abyssal reservoir model for deglacial radiocarbon changes in the mid-depth Indo-Pacific Ocean, *Geophys. Res. Lett.*, *38*(4), n/a-n/a, doi:10.1029/2010GL046158.

Hain, M. P., D. M. Sigman, and G. H. Haug (2014), Distinct roles of the Southern Ocean and North Atlantic in the deglacial atmospheric radiocarbon decline, *Earth Planet. Sci. Lett.*, *394*, 198–208, doi:10.1016/j.epsl.2014.03.020.

Heaton, T. J., E. Bard, and K. A. Hughen (2013), Elastic Tie-Pointing—Transferring Chronologies between Records via a Gaussian Process, *Radiocarbon*, *55*(4), 1975–1997, doi:10.2458/azu_js_rc.55.17777.

Hertzberg, J. E., D. C. Lund, A. Schmittner, and A. L. Skrivanek (2016), Evidence for a biological pump driver of atmospheric CO_2 rise during Heinrich Stadial 1, *Geophys. Res. Lett.*, *43*(23), 12,242-12,251, doi:10.1002/2016GL070723.

Hines, S. K. V., J. R. Southon, and J. F. Adkins (2015), A high-resolution record of Southern Ocean intermediate water radiocarbon over the past 30,000 years, *Earth Planet. Sci. Lett.*, *432*, 46–58, doi:10.1016/j.epsl.2015.09.0\\

Hodkinson, R. A., P. Stoffers, J. Scholten, D. S. Cronan, G. Jeschke, and T. D. S. Rogers (1994), Geochemistry of hydrothermal manganese deposits from the Pitcairn Island hotspot, southeastern Pacific, *Geochim. Cosmochim. Ac.*, *58*(22), 5011–5029, doi:10.1016/0016-7037(94)90228-3.

Holmen, K. (1992), The global carbon cycle, in *Global Biogeochemical Cycles*, edited by S. S. Butcher, R. J. Charlson, G. H. Orians, and G. V. Wolfe, pp. 239–262, Academic Press, London.

Hoogakker, B. A. A., H. Elderfield, G. Schmiedl, I. N. McCave, and R. E. M. Rickaby (2014), Glacial–interglacial changes in bottom-water oxygen content on the Portuguese margin, *Nat. Geosci.*, *8*(1), 40–43, doi:10.1038/ngeo2317.

Hoogakker, B. A. A., Z. Lu, N. Umling, L. Jones, X. Zhou, R. Rickaby, R. Thunell, O. Cartapanis, E. Galbraith, Submitted.

Huang, K.-F., D. W. Oppo, and W. B. Curry (2014), Decreased influence of Antarctic intermediate water in the tropical Atlantic during North Atlantic cold events, Earth Planet. Sci. Lett., 389, 200–208, doi:10.1016/j.epsl.2013.12.037.

Hughen, K. A., J. R. Southon, S. J. Lehman, and J. T. Overpeck (2000), Synchronous radiocarbon and climate shifts during the last deglaciation, *Science*, *290*(5498), 1951–1955.

Inoue, H., and Y. Sugimura (1985), Carbon isotopic fractionation during the CO_2 exchange process between air and sea water under equilibrium and kinetic conditions, *Geochim. Cosmochim. Ac.*, *49*(11), 2453–2460, doi:10.1016/0016-7037(85)90245-5.

IPCC, 2014*:* Climate Change 2014: Synthesis Report. Contribution of Working Groups I, II and III to the Fifth Assesment Report of the Intergovernmental Panel on Climate Change., 151, Geneva, Switzerland.

Jaccard, S. L., and E. D. Galbraith (2011), Large climate-driven changes of oceanic oxygen concentrations during the last deglaciation, *Nat. Geosci.*, *5*(2), 151–156, doi:10.1038/ngeo1352.

Jaccard, S. L., E. D. Galbraith, D. M. Sigman, G. H. Haug, R. Francois, T. F. Pedersen, P. Dulski, and H. R. Thierstein (2009), Subarctic Pacific evidence for a glacial deepening of the oceanic respired carbon pool, *Earth Planet. Sci. Lett.*, *277*(1–2), 156–165, doi:10.1016/j.epsl.2008.10.017.

Janssen, D. J., T. M. Conway, S. G. John, J. R. Christian, D. I. Kramer, T. F. Pedersen, and J. T. Cullen (2014), Undocumented water column sink for cadmium in open ocean oxygen-deficient zones, *Proc. Natl. Acad. Sci. USA.*, *111*(19), 6888–6893, doi:10.1073/pnas.1402388111.

Johnsen, S. J. et al. (1997), The $\delta^{18}O$ record along the Greenland Ice Core Project deep ice core and the problem of possible Eemian climatic instability, *J. Geophys. Res.*, *102*(C12), 26397–26410, doi:10.1029/97JC00167.

Jorissen, F. J., H. C. de Stigter, and J. G. V. Widmark (1995), A conceptual model explaining benthic foraminiferal microhabitats, *Mar. Micropaleontol.*, *26*(1–4), 3–15, doi:10.1016/0377-8398(95)00047-X.

Keeling, R. F., and B. B. Stephens (2001), Antarctic sea ice and the control of Pleistocene climate instability, *Paleoceanography*, *16*(1), 112–131, doi:10.1029/2000PA000529.

Key, R. M., P. D. Quay, G. A. Jones, A. P. McNichol, K. F. Von Reden, and R. J. Schneider (1996), WOCE AMS Radiocarbon I: Pacific Ocean Results (P6, P16 and P17), *Radiocarbon*, *38*(3), 425–518, doi:10.1017/S0033822200030071.

Key, R. M., A. Kozyr, C. L. Sabine, K. Lee, R. Wanninkhof, J. L. Bullister, R. A. Feely, F. J. Millero, C. Mordy, and T.-H. Peng (2004), A global ocean carbon climatology: Results from Global Data Analysis Project (GLODAP), *Glob. Biogeochem. Cy.*, *18*(4), GB4031, doi:10.1029/2004GB002247.

Kienast, M., S. S. Kienast, S. E. Calvert, T. I. Eglinton, G. Mollenhauer, R. François, and A. C. Mix (2006), Eastern Pacific cooling and Atlantic overturning circulation during the last deglaciation, *Nature*, *443*(7113), 846–849, doi:10.1038/nature05222.

Klinkhammer, G., M. Bender, and R. F. Weiss (1977), Hydrothermal manganese in the Galapagos Rift, *Nature*, *269*(5626), 319–320, doi:10.1038/269319a0.

Klinkhammer, G. P. (1980), Observations of the distribution of manganese over the East Pacific Rise, *Chem. Geol.*, *29*(1–4), 211–226, doi:10.1016/0009-2541(80)90021-2.

Kohfeld, K. E. (2005), Role of Marine Biology in Glacial-Interglacial CO_2 Cycles, *Science*, *308*(5718), 74–78, doi:10.1126/science.1105375.

Köhler, P., G. Knorr, and E. Bard (2014), Permafrost thawing as a possible source of abrupt carbon release at the onset of the Bølling/Allerød, *Nat. Commun.*, *5*, 5520, doi:10.1038/ncomms6520.

Kubota, K., Y. Yokoyama, T. Ishikawa, S. Obrochta, and A. Suzuki (2015), Larger CO_2 source at the equatorial Pacific during the last deglaciation, *Sci. Rep.*, *4*(1), doi:10.1038/srep05261.

Lacis, A. A., G. A. Schmidt, D. Rind, and R. A. Ruedy (2010), Atmospheric CO_2: Principal Control Knob Governing Earth's Temperature, *Science*, *330*(6002), 356–359, doi:10.1126/science.1190653.

Lal, D., Peters, B., 1967. Cosmic rays produced radioactivity on the Earth. In: Handbuch der Physik, vol. 46, pp. 551–612.

Lea, D. W., D. K. Pak, and G. Paradis (2005), Influence of volcanic shards on foraminiferal Mg/Ca in a core from the Galápagos region, *Geochem. Geophys. Geosyst.*, *6*(11), n/a-n/a, doi:10.1029/2005GC000970.

Leduc, G., L. Vidal, K. Tachikawa, F. Rostek, C. Sonzogni, L. Beaufort, and E. Bard (2007), Moisture transport across Central America as a positive feedback on abrupt climatic changes, *Nature*, *445*(7130), 908–911, doi:10.1038/nature05578.

Lee, K., T.-W. Kim, R. H. Byrne, F. J. Millero, R. A. Feely, and Y.-M. Liu (2010), The universal ratio of boron to chlorinity for the North Pacific and North Atlantic oceans, *Geochim. Cosmochim. Ac.*, *74*(6), 1801–1811, doi:10.1016/j.gca.2009.12.027.

Lenton, T. M., V. N. Livina, V. Dakos, and M. Scheffer (2012), Climate bifurcation during the last deglaciation?, *Clim. Past*, *8*(4), 1127–1139, doi:10.5194/cp-8-1127-2012.

Lindsay, C. M., S. J. Lehman, T. M. Marchitto, and J. D. Ortiz (2015), The surface expression of radiocarbon anomalies near Baja California during deglaciation, *Earth Planet. Sci. Lett.*, *422*, 67–74, doi:10.1016/j.epsl.2015.04.012.

Lund, D. C. (2013), Deep Pacific ventilation ages during the last deglaciation: Evaluating the influence of diffusive mixing and source region reservoir age, *Earth Planet. Sci. Lett.*, *381*, 52–62, doi:10.1016/j.epsl.2013.08.032.

Lund, D. C., P. D. Asimow, K. A. Farley, T. O. Rooney, E. Seeley, E. W. Jackson, and Z. M. Durham (2016), Enhanced East Pacific Rise hydrothermal activity during the last two glacial terminations, *Science*, *351*(6272), 478–482, doi:10.1126/science.aad4296.

Lynch-Stieglitz, J., and R. G. Fairbanks (1994), A conservative tracer for glacial ocean circulation from carbon isotope and palaeo-nutrient measurements in benthic foraminifera, *Nature*, *369*(6478), 308–310, doi:10.1038/369308a0.

Lynch-Stieglitz, J., T. F. Stocker, W. S. Broecker, and R. G. Fairbanks (1995), The influence of air-sea exchange on the isotopic composition of oceanic carbon: Observations and modeling, *Glob. Biogeochem. Cy.*, *9*(4), 653–665, doi:10.1029/95GB02574.

Lynch-Stieglitz, J., A. van Geen, and R. G. Fairbanks (1996), Interocean exchange of glacial North Atlantic Intermediate Water: Evidence from subantarctic Cd/Ca and carbon isotope measurements, *Paleoceanography*, *11*(2), 191–201, doi:10.1029/95PA03772.

Mackensen, A. (2008), On the use of benthic foraminiferal $\delta^{13}C$ in palaeoceanography: constraints from primary proxy relationships, *Geol. Soc. Spec. Publ.*, *303*(1), 121–133, doi:10.1144/SP303.9.

Mackensen, A., H.-W. Hubberten, T. Bickert, G. Fischer, and D. K. Fütterer (1993), The $\delta^{13}C$ in benthic foraminiferal tests of *Fontbotia wuellerstorfi* (Schwager) Relative to the $\delta^{13}C$ of dissolved inorganic carbon in Southern Ocean Deep Water: Implications for glacial ocean circulation models, *Paleoceanography*, *8*(5), 587–610, doi:10.1029/93PA01291.

Magana, A. L., J. R. Southon, J. P. Kennett, E. B. Roark, M. Sarnthein, and L. D. Stott (2010), Resolving the cause of large differences between deglacial benthic foraminifera radiocarbon measurements in Santa Barbara Basin, *Paleoceanography*, *25*(4), PA4102, doi:10.1029/2010PA002011.

Marchig, V., P. Möller, H. Bäcker, and P. Dulski (1984), Foraminiferal ooze from the Galapagos Rift area- Hydrothermal impact and diagenetic mobilization of elements, *Mar. Geol.*, *62*(1–2), 85–104, doi:10.1016/0025-3227(84)90056-2.

Marchitto, T. M., S. J. Lehman, J. D. Ortiz, J. Fluckiger, and A. van Geen (2007), Marine Radiocarbon Evidence for the Mechanism of Deglacial Atmospheric CO_2 Rise, *Science*, *316*(5830), 1456–1459, doi:10.1126/science.1138679.

Marcott, S. A. et al. (2014), Centennial-scale changes in the global carbon cycle during the last deglaciation, *Nature*, *514*(7524), 616–619, doi:10.1038/nature13799.

Martin, J. H. (1990), Glacial-interglacial CO_2 change: The Iron Hypothesis, *Paleoceanography*, *5*(1), 1–13, doi:10.1029/PA005i001p00001.

Martínez-Botí, M. A., G. Marino, G. L. Foster, P. Ziveri, M. J. Henehan, J. W. B. Rae, P. G. Mortyn, and D. Vance (2015a), Boron isotope evidence for oceanic carbon dioxide leakage during the last deglaciation, *Nature*, *518*(7538), 219–222, doi:10.1038/nature14155.

Martinez-Garcia, A., D. M. Sigman, H. Ren, R. F. Anderson, M. Straub, D. A. Hodell, S. L. Jaccard, T. I. Eglinton, and G. H. Haug (2014), Iron Fertilization of the Subantarctic Ocean During the Last Ice Age, *Science*, *343*(6177), 1347–1350, doi:10.1126/science.1246848.

Matsumoto, K., J. L. Sarmiento, and M. A. Brzezinski (2002), Silicic acid leakage from the Southern Ocean: A possible explanation for glacial atmospheric pCO_2, *Glob. Biogeochem. Cy.*, *16*(3), 5-1-5–23, doi:10.1029/2001GB001442.

Matsumoto, K., and Y. Yokoyama (2013), Atmospheric $\Delta^{14}C$ reduction in simulations of Atlantic overturning circulation shutdown, *Glob. Biogeochem. Cy.*, *27*(2), 296–304, doi:10.1002/gbc.20035.

McCorkle, D. C., and S. R. Emerson (1988), The relationship between pore water carbon isotopic composition and bottom water oxygen concentration, *Geochim. Cosmochim. Ac.*, *52*(5), 1169–1178, doi:10.1016/0016-7037(88)90270-0.

McCorkle, D. C., L. D. Keigwin, B. H. Corliss, and S. R. Emerson (1990), The influence of microhabitats on the carbon isotopic composition of deep-sea benthic foraminifera, *Paleoceanography*, *5*(2), 161–185, doi:10.1029/PA005i002p00161.

McManus, J., W. M. Berelson, G. P. Klinkhammer, D. E. Hammond, and C. Holm (2005), Authigenic uranium: Relationship to oxygen penetration depth and organic carbon rain, *Geochim. Cosmochim. Ac.*, *69*(1), 95–108, doi:10.1016/j.gca.2004.06.023.

Mehrbach, C., C. H. Culberson, J. E. Hawley, and R. M. Pytkowicx (1973), Measurement of the apparent dissociation constants of carbonic acid in seawater at atmospheric pressure, *Limnol. Oceanogr.*, *18*(6), 897–907, doi:10.4319/lo.1973.18.6.0897.

Misra, S., M. Greaves, R. Owen, J. Kerr, A. C. Elmore, and H. Elderfield (2014), Determination of B/Ca of natural carbonates by HR-ICP-MS, *Geochem. Geophys. Geosyst.*, *15*(4), 1617–1628, doi:10.1002/2013GC005049.

Monnin, E. (2001), Atmospheric CO_2 Concentrations over the Last Glacial Termination, *Science*, *291*(5501), 112–114, doi:10.1126/science.291.5501.112.

Morford, J. L., and S. Emerson (1999), The geochemistry of redox sensitive trace metals in sediments, *Geochim. Cosmochim. Ac.*, *63*(11–12), 1735–1750, doi:10.1016/S0016-7037(99)00126-X.

Okazaki, Y., A. Timmermann, L. Menviel, N. Harada, A. Abe-Ouchi, M. O. Chikamoto, A. Mouchet, and H. Asahi (2010), Deepwater Formation in the North Pacific During the Last Glacial Termination, *Science*, *329*(5988), 200–204, doi:10.1126/science.1190612.

Ortlieb, L., G. Vargas, and J.-F. Saliège (2011), Marine radiocarbon reservoir effect along the northern Chile–southern Peru coast (14–24°S) throughout the Holocene, *Quat. Res.*, *75*(1), 91–103, doi:10.1016/j.yqres.2010.07.018.

Osborne, A. H., E. C. Hathorne, J. Schijf, Y. Plancherel, P. Böning, and M. Frank (2017), The potential of sedimentary foraminiferal rare earth element patterns to trace water masses in the past, *Geochem. Geophys. Geosyst.*, *18*(4), 1550–1568, doi:10.1002/2016GC006782.

Pahnke, K., S. L. Goldstein, and S. R. Hemming (2008), Abrupt changes in Antarctic Intermediate Water circulation over the past 25,000 years, *Nat. Geosci.*, *1*(12), 870–874, doi:10.1038/ngeo360.

Parrenin, F., V. Masson-Delmotte, P. Kohler, D. Raynaud, D. Paillard, J. Schwander, C. Barbante, A. Landais, A. Wegner, and J. Jouzel (2013), Synchronous Change of Atmospheric CO_2 and Antarctic Temperature During the Last Deglacial Warming, *Science*, *339*(6123), 1060–1063, doi:10.1126/science.1226368.

Paterne, M., L. K. Ayliffe, M. Arnold, G. Cabioch, N. Tisnérat-Laborde, C. Hatté, E. Douville, and E. Bard (2004), Paired 14C and 230Th/U Dating of Surface Corals from the Marquesas and Vanuatu (Sub-Equatorial Pacific) in the 3000 to 15,000 Cal Yr Interval, *Radiocarbon*, *46*(2), 551–566, doi:10.1017/S0033822200035608.

Pedersen, T. F. (1979), The geochemistry of sediments of the Panama Basin, eastern equatorial Pacific Ocean. PhD dissertation, Univ. of Edinburgh.

Pena, L. D., E. Calvo, I. Cacho, S. Eggins, and C. Pelejero (2005), Identification and removal of Mn-Mg-rich contaminant phases on foraminiferal tests: Implications for Mg/Ca past temperature reconstructions: Mg/Ca, *Geochem. Geophys. Geosyst.*, *6*(9), Q09P02, doi:10.1029/2005GC000930.

Pena, L. D., I. Cacho, E. Calvo, C. Pelejero, S. Eggins, and A. Sadekov (2008), Characterization of contaminant phases in foraminifera carbonates by electron microprobe mapping, *Geochem. Geophys. Geosyst.*, *9*(7), Q07012, doi:10.1029/2008GC002018.

Pennington, J. T., K. L. Mahoney, V. S. Kuwahara, D. D. Kolber, R. Calienes, and F. P. Chavez (2006), Primary production in the eastern tropical Pacific: A review, *Prog. Oceanogr.*, *69*(2–4), 285–317, doi:10.1016/j.pocean.2006.03.012.

Pichevin, L. E., B. C. Reynolds, R. S. Ganeshram, I. Cacho, L. Pena, K. Keefe, and R. M. Ellam (2009), Enhanced carbon pump inferred from relaxation of nutrient limitation in the glacial ocean, *Nature*, *459*(7250), 1114–1117, doi:10.1038/nature08101.

Praetorius, S. K., and A. C. Mix (2014), Synchronization of North Pacific and Greenland climates preceded abrupt deglacial warming, *Science*, *345*(6195), 444–448, doi:10.1126/science.1252000.

Rae, J. W. B., G. L. Foster, D. N. Schmidt, and T. Elliott (2011), Boron isotopes and B/Ca in benthic foraminifera: Proxies for the deep ocean carbonate system, *Earth Planet. Sci. Lett.*, *302*(3–4), 403–413, doi:10.1016/j.epsl.2010.12.034.

Rae, J. W. B., M. Sarnthein, G. L. Foster, A. Ridgwell, P. M. Grootes, and T. Elliott (2014), Deep water formation in the North Pacific and deglacial CO_2 rise, *Paleoceanography*, *29*(6), 645–667, doi:10.1002/2013PA002570.

Rasmussen, S. O. et al. (2014), A stratigraphic framework for abrupt climatic changes during the Last Glacial period based on three synchronized Greenland ice-core records: refining and extending the INTIMATE event stratigraphy, *Quat. Sci. Rev.*, *106*, 14–28, doi:10.1016/j.quascirev.2014.09.007.

Reimer, P. J. et al. (2013), IntCal13 and Marine13 Radiocarbon Age Calibration Curves 0–50,000 Years cal BP, *Radiocarbon*, *55*(4), 1869–1887, doi:10.2458/azu_js_rc.55.16947.

Robbins, L. L., M. E. Hansen, J. A. Kleypas, and S. C. Meylan (2010), *CO2calc—A user-friendly seawater carbon calculator for Windows, Max OS X, and iOS (iPhone)*, Open-File Report, U. S. Geological Survey.

Robinson, L. F. (2005), Radiocarbon Variability in the Western North Atlantic During the Last Deglaciation, *Science*, *310*(5753), 1469–1473, doi:10.1126/science.1114832.

Rodgers, K. B., B. Blanke, G. Madec, O. Aumont, P. Ciais, and J.-C. Dutay (2003), Extratropical sources of Equatorial Pacific upwelling in an OGCM, *Geophys. Res. Lett.*, *30*(2), doi:10.1029/2002GL016003.

Ronge, T. A., R. Tiedemann, F. Lamy, P. Köhler, B. V. Alloway, R. De Pol-Holz, K. Pahnke, J. Southon, and L. Wacker (2016), Radiocarbon constraints on the extent and evolution of the South Pacific glacial carbon pool, *Nat. Commun.*, *7*, 11487, doi:10.1038/ncomms11487.

Rose, K. A., E. L. Sikes, T. P. Guilderson, P. Shane, T. M. Hill, R. Zahn, and H. J. Spero (2010), Upper-ocean-to-atmosphere radiocarbon offsets imply fast deglacial carbon dioxide release, *Nature*, *466*(7310), 1093–1097, doi:10.1038/nature09288.

Sarnthein, M., S. Balmer, P. M. Grootes, and M. Mudelsee (2015), Planktic and Benthic ^{14}C Reservoir Ages for Three Ocean Basins, Calibrated by a Suite of ^{14}C Plateaus in the Glacial-to-Deglacial Suigetsu Atmospheric ^{14}C Record, *Radiocarbon*, *57*(1), 129–151, doi:10.2458/azu_rc.57.17916.

Schlitzer, R., 2015. Ocean Data View, odv.awi.de

Seierstad, I. K. et al. (2014), Consistently dated records from the Greenland GRIP, GISP2 and NGRIP ice cores for the past 104 ka reveal regional millennial-scale δ^{18}O gradients with possible Heinrich event imprint, *Quat. Sci. Rev.*, *106*, 29–46, doi:10.1016/j.quascirev.2014.10.032.

Shackleton, N. J., J.-C. Duplessy, M. Arnold, P. Maurice, M. A. Hall, and J. Cartlidge (1988), Radiocarbon age of last glacial Pacific deep water, *Nature*, *335*(6192), 708–711, doi:10.1038/335708a0.

Shakun, J. D., P. U. Clark, F. He, S. A. Marcott, A. C. Mix, Z. Liu, B. Otto-Bliesner, A. Schmittner, and E. Bard (2012), Global warming preceded by increasing carbon dioxide concentrations during the last deglaciation, *Nature*, *484*(7392), 49–54, doi:10.1038/nature10915.

Siani, G., E. Michel, R. De Pol-Holz, T. DeVries, F. Lamy, M. Carel, G. Isguder, F. Dewilde, and A. Lourantou (2013), Carbon isotope records reveal precise timing of enhanced Southern Ocean upwelling during the last deglaciation, *Nat. Commun.*, *4*, doi:10.1038/ncomms3758.

Sigman, D. M., and E. A. Boyle (2000), Glacial/interglacial variations in atmospheric carbon dioxide, *Nature*, *407*(6806), 859–869, doi:10.1038/35038000.

Sikes, E. L., and T. P. Guilderson (2016), Southwest Pacific Ocean surface reservoir ages since the last glaciation: Circulation insights from multiple-core studies, *Paleoceanography*, *31*(2), 298–310, doi:10.1002/2015PA002855.

Sikes, E. L., C. R. Samson, T. P. Guilderson, and W. R. Howard (2000), Old radiocarbon ages in the southwest Pacific Ocean during the last glacial period and deglaciation, *Nature*, *405*(6786), 555–559, doi:10.1038/35014581.

Sikes, E. L., M. S. Cook, and T. P. Guilderson (2016), Reduced deep ocean ventilation in the Southern Pacific Ocean during the last glaciation persisted into the deglaciation, *Earth Planet. Sci. Lett.*, *438*, 130–138, doi:10.1016/j.epsl.2015.12.039.

Skinner, L., I. N. McCave, L. Carter, S. Fallon, A. E. Scrivner, and F. Primeau (2015), Reduced ventilation and enhanced magnitude of the deep Pacific carbon pool during the last glacial period, *Earth Planet. Sci. Lett.*, *411*, 45–52, doi:10.1016/j.epsl.2014.11.024.

Skinner, L. C. (2009), Glacial-interglacial atmospheric CO_2 change: a possible "standing volume" effect on deep-ocean carbon sequestration, *Clim. Past*, *5*(3), 537–550, doi:10.5194/cp-5-537-2009.

Skinner, L. C., S. Fallon, C. Waelbroeck, E. Michel, and S. Barker (2010), Ventilation of the Deep Southern Ocean and Deglacial CO_2 Rise, *Science*, *328*(5982), 1147–1151, doi:10.1126/science.1183627.

Skinner, L. C., C. Waelbroeck, A. E. Scrivner, and S. J. Fallon (2014), Radiocarbon evidence for alternating northern and southern sources of ventilation of the deep Atlantic carbon pool during the last deglaciation, *Proc. Natl. Acad. Sci. USA.*, *111*(15), 5480–5484, doi:10.1073/pnas.1400668111.

Southon, J., A. L. Noronha, H. Cheng, R. L. Edwards, and Y. Wang (2012), A high-resolution record of atmospheric 14C based on Hulu Cave speleothem H82, *Quat. Sci. Rev.*, *33*, 32–41, doi:10.1016/j.quascirev.2011.11.022.

Stephens, B. B., and R. F. Keeling (2000), The influence of Antarctic sea ice on glacial–interglacial CO_2 variations, *Nature*, *404*(6774), 171–174, doi:10.1038/35004556.

Stott, L., J. Southon, A. Timmermann, and A. Koutavas (2009), Radiocarbon age anomaly at intermediate water depth in the Pacific Ocean during the last deglaciation, *Paleoceanography*, *24*(2), n/a-n/a, doi:10.1029/2008PA001690.

Stuiver, M., and H. A. Polach (1977), Discussion Reporting of ^{14}C Data, *Radiocarbon*, *19*(3), 355–363, doi:10.1017/S0033822200003672.

Takahashi, T. et al. (2002), Global sea–air CO2 flux based on climatological surface ocean pCO_2, and seasonal biological and temperature effects, *Deep-Sea Res.*, *49*(9–10), 1601–1622, doi:10.1016/S0967-0645(02)00003-6.

Taylor, S. R., and S. M. McLennan (1985), *The Continental Crust: Its composition and Evolution*, Blackwell Sci., Oxford, U.K.

Thornalley, D. J. R., S. Barker, W. S. Broecker, H. Elderfield, and I. N. McCave (2011), The Deglacial Evolution of North Atlantic Deep Convection, *Science*, *331*(6014), 202–205, doi:10.1126/science.1196812.

Thornalley, D. J. R., H. A. Bauch, G. Gebbie, W. Guo, M. Ziegler, S. M. Bernasconi, S. Barker, L. C. Skinner, and J. Yu (2015), A warm and poorly ventilated deep Arctic Mediterranean during the last glacial period, *Science*, *349*(6249), 706–710, doi:10.1126/science.aaa9554.

Toggweiler, J. R., K. Dixon, and W. S. Broecker (1991), The Peru upwelling and the ventilation of the south Pacific thermocline, *J. Geophys. Res.*, *96*(C11), 20467, doi:10.1029/91JC02063.

Toggweiler, J. R., J. L. Russell, and S. R. Carson (2006), Midlatitude westerlies, atmospheric CO_2, and climate change during the ice ages, *Paleoceanography*, *21*(2), PA2005, doi:10.1029/2005PA001154.

Tribovillard, N., T. J. Algeo, T. Lyons, and A. Riboulleau (2006), Trace metals as paleoredox and paleoproductivity proxies: An update, *Chem. Geol.*, *232*(1–2), 12–32, doi:10.1016/j.chemgeo.2006.02.012.

Tsuchiya, M., and L. D. Talley (1998), A Pacific hydrographic section at 88°W: Water-property distribution, *J. Geophys. Res.*, *103*(C6), 12899–12918, doi:10.1029/97JC03415.

Umling, N. E., and R. C. Thunell (2017), Synchronous deglacial thermocline and deep-water ventilation in the eastern equatorial Pacific, *Nat. Commun.*, *8*, 14203, doi:10.1038/ncomms14203.

Wang, Y. J. (2001), A High-Resolution Absolute-Dated Late Pleistocene Monsoon Record from Hulu Cave, China, *Science*, *294*(5550), 2345–2348, doi:10.1126/science.1064618.

Watson, A. J., and A. C. Naveira Garabato (2006), The role of Southern Ocean mixing and upwelling in glacial-interglacial atmospheric CO_2 change, *Tellus B*, *58*(1), 73–87, doi:10.1111/j.1600-0889.2005.00167.x.

Watson, A. J., G. K. Vallis, and M. Nikurashin (2015), Southern Ocean buoyancy forcing of ocean ventilation and glacial atmospheric CO_2, *Nat. Geosci.*, *8*(11), 861–864, doi:10.1038/ngeo2538.

Willbold, M., K. P. Jochum, I. Raczek, M. A. Amini, B. Stoll, and A. W. Hofmann (2003), Validation of multi-element isotope dilution ICPMS for the analysis of basalts, *Anal. Bioanal. Chem.*, *377*(1), 117–125, doi:10.1007/s00216-003-2037-4.

Wright, J., H. Schrader, and W. T. Holser (1987), Paleoredox variations in ancient oceans recorded by rare earth elements in fossil apatite, *Geochim. Cosmochim. Ac.*, *51*(3), 631–644, doi:10.1016/0016-7037(87)90075-5.

Wu, J., Y. Wang, H. Cheng, and L. R. Edwards (2009), An exceptionally strengthened East Asian summer monsoon event between 19.9 and 17.1 ka BP recorded in a Hulu stalagmite, *Sci. China D*, *52*(3), 360–368, doi:10.1007/s11430-009-0031-1.

Xie, S.-P., Y. Okumura, T. Miyama, and A. Timmermann (2008), Influences of Atlantic Climate Change on the Tropical Pacific via the Central American Isthmus, *J. Climate*, *21*(15), 3914–3928, doi:10.1175/2008JCLI2231.1.

Yu, J., H. Elderfield, and A. M. Piotrowski (2008), Seawater carbonate ion-δ13C systematics and application to glacial–interglacial north Atlantic Ocean circulation, *Earth Planet. Sci. Lett.*, *271*(1–4), 209–220, doi:10.1016/j.epsl.2008.04.010.

Yu, J., W. S. Broecker, H. Elderfield, Z. Jin, J. McManus, and F. Zhang (2010), Loss of Carbon from the Deep Sea Since the Last Glacial Maximum, *Science*, *330*(6007), 1084–1087, doi:10.1126/science.1193221.

Yu, J., R. F. Anderson, Z. Jin, J. W. B. Rae, B. N. Opdyke, and S. M. Eggins (2013), Responses of the deep ocean carbonate system to carbon reorganization during the Last Glacial–interglacial cycle, *Quat. Sci. Rev.*, *76*, 39–52, doi:10.1016/j.quascirev.2013.06.020.

Yu, J., R. F. Anderson, Z. Jin, L. Menviel, F. Zhang, F. J. Ryerson, and E. J. Rohling (2014), Deep South Atlantic carbonate chemistry and increased interocean deep water exchange during last deglaciation, *Quat. Sci. Rev.*, *90*, 80–89, doi:10.1016/j.quascirev.2014.02.018.

Ziegler, M., P. Diz, I. R. Hall, and R. Zahn (2013), Millennial-scale changes in atmospheric CO_2 levels linked to the Southern Ocean carbon isotope gradient and dust flux, *Nat. Geosci.*, *6*(6), 457–461, doi:10.1038/ngeo1782.

APPENDIX A

PERMISSION TO REPRINT

Permission requests from authors

The authors of articles published by Nature Publishing Group, or the authors' designated agents, do not usually need to seek permission for re-use of their material as long as the journal is credited with initial publication. For further information about the terms of re-use for authors please see below.

Author Requests

If you are the author of this content (or his/her designated agent) please read the following. Since 2003, ownership of copyright in in original research articles remains with the Authors*, and provided that, when reproducing the Contribution or extracts from it, the Authors acknowledge first and reference publication in the Journal, the Authors retain the following non-exclusive rights:

a. To reproduce the Contribution in whole or in part in any printed volume (book or thesis) of which they are the author(s).
b. They and any academic institution where they work at the time may reproduce the Contribution for the purpose of course teaching.
c. To reuse figures or tables created by them and contained in the Contribution in other works created by them.
d. To post a copy of the Contribution as accepted for publication after peer review (in Word or Tex format) on the Author's own web site, or the Author's institutional repository, or the Author's funding body's archive, six months after publication of the printed or online edition of the Journal, provided that they also link to the Journal article on NPG's web site (eg through the DOI).

NPG encourages the self-archiving of the accepted version of your manuscript in your funding agency's or institution's repository, six months after publication. This policy complements the recently announced policies of the US National Institutes of Health, Wellcome Trust and other research funding bodies around the world. NPG recognizes the efforts of funding bodies to increase access to the research they fund, and we strongly encourage authors to participate in such efforts.

Authors wishing to use the published version of their article for promotional use or on a web site must request in the normal way.

If you require further assistance please read NPG's online author reuse guidelines.

Note: *British Journal of Cancer* maintains copyright polices of its own that are different from the general NPG policies. Please consult this journal to learn more.

* Commissioned material is still subject to copyright transfer conditions

APPENDIX B

CHAPTER 1 SUPPLEMENTARY INFORMATION

Table B.1 Benthic and planktonic radiocarbon data from TR163-23.

TR163-23 depth (cm)	Planktonic radiocarbon				Benthic radiocarbon				
	UCIAMS ID	taxa	14C age 14C yrs	±1σ	UCIAMS ID	14C age (14C yrs)	±1σ	B-P 14C yrs	±1σ
5	142516	*N. dutertrei*	2440	25	143508	3905	25	1465	35
30					152087	6705	30		
60.5	152095	*N. dutertrei*	9090	20	143509	10275	40	1185	45
60.5	141004	*G. ruber*	8790	25					
70.5	141005	*N. dutertrei*	9920	25	143510	11070	40	1150	47
75					152088	11575	35		
80					152089	11745	45		
85	159392	*N. dutertrei*	11250	25	143511	12540	55	1290	60
85	141006	*G. ruber*	11210	30					
87.5	162945	*N. dutertrei*	11485	20					
90	144872	*N. dutertrei*	12270	35	144881	13055	40	785	53
92.5	162946	*N. dutertrei*	11945	20	152090	13020	60	1075	63
95	144873	*N. dutertrei*	12425	35	144882	13500	45	1075	57
97.5	147290	*N. dutertrei*	11760	35	147285	13040	50	1280	61
100	159393	*N. dutertrei*	12575	40	143512	13960	60	1385	72
100	142517	*G. ruber*	12595	30					
102.5	162947	*N. dutertrei*	12995	25					
105	144874	*N. dutertrei*	12605	35	144883	13770	45	1165	57
107.5	147291	*N. dutertrei*	12630	40	147286	13890	60	1260	72
110	142518	*N. dutertrei*	12925	40					
112.5	147292	*N. dutertrei*	12600	45	147287	13780	60	1180	75
115	159394	*N. dutertrei*	13095	35	144884	14760	60	1665	69
115	144875	*G. ruber*	12525	30					
117.5	147293	*N. dutertrei*	14160	50	147288	15750	80	1590	94
120	142519	*N. dutertrei*	14260	45	143513	15660	70	1400	83
122.5	162948	*N. dutertrei*	14430	25	152091	15830	60	1400	65
125	144876	*N. dutertrei*	14970	45	144885	16230	60	1260	75
127.5	162949	*N. dutertrei*	14605	30					
130	162950	*N. dutertrei*	15085	30	152092	16690	50	1605	58
135	147294	*N. dutertrei*	15505	50	147289	17070	80	1565	94
140	162951	*N. dutertrei*	16625	35	152093	17890	50	1265	61
145	152096	*N. dutertrei*	16990	60	143514	18310	90	1320	108
145	142520	*G. ruber, sacculifer*	16600	70					
150	162952	*N. dutertrei*	17410	35					
154.5	144877	*N. dutertrei*	17840	60					
159.5	162953	*N. dutertrei*	18175	40					
169.5	144878	*N. dutertrei*	18960	70	152094	20180	90	1220	114
184.5	159395	*N. dutertrei*	20470	90					
184.5	144879	*G. ruber, sacculifer*	19380	110					
194.5	162954	*N. dutertrei*	21500	70					

Table B.2 Age model constructed using a constant reservoir age.

TR163-23	Constant reservoir age (ΔR=147±13)			
depth (cm)	min age (yrs BP)	max age (yrs BP)	mean age (yrs BP)	Sedimentation rate (cm/kyr)
0.5	1011	1801	1477	
5	1795	2095	1923	10.08
15.5	2729	4170	3372	7.25
20	3233	4854	3990	7.27
25	3855	5544	4681	7.24
30	4510	6277	5400	6.95
35.5	5309	7036	6182	7.04
40	5978	7604	6798	7.31
45.5	6743	8275	7534	7.47
50	7456	8797	8157	7.23
55.5	8353	9338	8916	7.24
60.5	9495	9731	9591	7.41
65	9812	10399	10084	9.13
70.5	10566	10927	10709	8.80
75	10945	11730	11305	7.56
80	11545	12330	11974	7.47
82.5	11920	12562	12304	7.58
85	12511	12719	12622	7.86
87.5	12717	12963	12836	11.69
90	12910	13400	13183	7.19
92.5	13204	13522	13343	15.66
95	13382	13728	13555	11.78
97.5	13489	13860	13694	17.96
100	13701	14010	13854	15.64
102.5	13818	14213	13975	20.76
105	13914	14341	14062	28.67
107.5	14010	14500	14179	21.40
110	14182	14700	14406	11.00
112.5	14378	14957	14668	9.54
115	14758	15326	15013	7.24
117.5	15804	16430	16179	2.14
120	16329	16762	16547	6.80
122.5	16634	17019	16839	8.56
125	16876	17404	17161	7.77
127.5	17094	17582	17349	13.25
130	17487	17877	17684	7.46
135	18056	18518	18256	8.75
140	19049	19517	19312	4.73
145	19630	20045	19840	9.48
150	20147	20518	20343	9.93
154.5	20620	21018	20819	9.47
159.5	21042	21522	21282	10.79
164.5	21487	22080	21787	9.89
169.5	22018	22509	22298	9.80
174.5	22491	23270	22869	8.75
179.5	23016	23828	23428	8.94
184.5	23700	24291	24004	8.69
189.5	24242	24997	24628	8.00
194.5	25004	25464	25253	8.01
199.5	25369	26237	25763	9.80

Table B.3 Tie point constraint of TR163-23 independent age models.

TR163-23 depth (cm)	Elastically derived Tie Points		
	Greenland tuned	Hulu cave tuned	Suigetsu 14C-plateau tuned
5	*N. dutertrei* 14C	*N. dutertrei* 14C	*N. dutertrei* 14C
60.5	*N. dutertrei* 14C	*N. dutertrei* 14C	*N. dutertrei* 14C
70.5	*N. dutertrei* 14C	*N. dutertrei* 14C	*N. dutertrei* 14C
80	GICC05 11443±90yrs	Hulu speleothem H82 11352±111	
90			plateau YD top 12499±137
95			
97.5			plateau YD base 13259±105
98.5			Hiatus
100	GICC05 13464±63 yrs	Hulu speleothem H82 13359±59	Plateau 1a top 13512±96
107.5			
110	GICC05 14486±75 yrs	Hulu speleothem H82 14363±58	
115			Plateau 1 base 15032±83
117.5			Plateau 2a top 15285±89
120			
122.5		Hulu speleothem H82 15618±86	Plateau 2a/2b 15792±106
130			Plateau 2b base 16551±138
135			
159.5		Hulu speleothem MSD 19497±113	
164.5			
199.5	GICC05 23992±204 yrs	Hulu speleothem MSD 24161±217	GICC05 23992±204 yrs

Table B.4 TR163-23 oxygen isotope tuned age models.

TR163-23	Greenland tuned age				Hulu tuned age			
depth (cm)	min age yrs BP	max age yrs BP	mean age yrs BP	Sedimentation rate cm/kyrs	min age yrs BP	max age yrs BP	mean age yrs BP	Sedimentation rate cm/kyrs
0.5	1041	1823	1502		965	1832	1500	
5	1836	2145	1978	9.46	1834	2157	1981	9.36
15.5	2733	4211	3422	7.27	2720	4247	3430	7.24
20	3249	4936	4055	7.10	3255	4962	4063	7.11
25	3883	5694	4758	7.11	3851	5697	4759	7.18
30	4539	6409	5459	7.14	4515	6435	5469	7.05
35.5	5279	7148	6218	7.25	5312	7120	6226	7.26
40	5923	7711	6843	7.20	5933	7683	6855	7.16
45.5	6738	8369	7594	7.33	6730	8372	7604	7.34
50	7454	8869	8215	7.25	7460	8874	8228	7.21
55.5	8422	9401	8987	7.12	8394	9405	8996	7.16
60.5	9561	9798	9656	7.47	9558	9795	9657	7.56
65	9858	10440	10141	9.28	9858	10450	10143	9.26
70.5	10596	10871	10726	9.40	10583	10861	10720	9.55
75	10845	11290	11058	13.57	10822	11274	11031	14.45
80	11223	11655	11421	13.77	11153	11635	11372	14.68
82.5	11390	11983	11659	10.51	11314	11947	11602	10.84
85	11567	12287	11904	10.22	11486	12225	11841	10.46
87.5	11760	12559	12150	10.15	11684	12491	12086	10.22
90	11987	12801	12394	10.22	11905	12728	12326	10.40
92.5	12237	13024	12642	10.11	12160	12927	12564	10.49
95	12491	13225	12890	10.06	12436	13122	12807	10.30
97.5	12811	13404	13140	10.03	12723	13286	13042	10.62
100	13212	13574	13389	10.02	13109	13447	13281	10.46
102.5	13406	13914	13644	9.83	13305	13794	13532	9.96
105	13611	14192	13897	9.85	13499	14064	13784	9.94
107.5	13861	14414	14152	9.82	13746	14270	14029	10.19
110	14200	14606	14401	10.06	14109	14435	14275	10.16
112.5	14372	15029	14661	9.60	14289	14813	14530	9.82
115	14531	15411	14921	9.61	14479	15102	14782	9.92
117.5	14719	15757	15186	9.46	14696	15348	15030	10.09
120	14910	16079	15448	9.52	14951	15561	15280	9.98
122.5	15121	16400	15714	9.41	15304	15758	15533	9.88
125	15340	16701	15981	9.37	15501	16145	15793	9.60
127.5	15575	17005	16247	9.37	15683	16501	16053	9.64
130	15799	17315	16511	9.50	15883	16815	16320	9.35
135	16245	17875	17045	9.36	16315	17415	16851	9.42
140	16712	18458	17571	9.51	16796	17960	17378	9.48
145	17172	19022	18093	9.58	17313	18483	17907	9.46
150	17674	19540	18619	9.49	17851	18962	18434	9.49
154.5	18143	20053	19102	9.32	18392	19345	18909	9.46
159.5	18648	20568	19631	9.46	19093	19749	19427	9.66
164.5	19189	21091	20154	9.56	19541	20490	19984	8.97
169.5	19720	21593	20682	9.46	19987	21175	20548	8.86
174.5	20261	22076	21209	9.50	20464	21801	21110	8.91
179.5	20826	22571	21741	9.39	20984	22396	21679	8.78
184.5	21416	23073	22276	9.35	21516	22946	22246	8.82
189.5	21998	23545	22810	9.36	22080	23503	22812	8.84
194.5	22614	23999	23335	9.51	22674	24008	23381	8.78
199.5	23256	24418	23859	9.55	23303	24483	23943	8.90

Table B.5 TR163-23 radiocarbon plateau tuned age models.

TR163-23	Plateau tuned age			
depth (cm)	min age (yrs BP)	max age (yrs BP)	mean age (yrs BP)	Sedimentation rate (yrs BP)
0.5	1043	1818	1481	
5	1833	2150	1977	9.07
15.5	2741	4256	3423	7.26
20	3302	4933	4057	7.10
25	3894	5660	4742	7.30
30	4534	6360	5448	7.08
35.5	5285	7096	6213	7.19
40	5923	7689	6844	7.14
45.5	6696	8354	7585	7.42
50	7441	8862	8214	7.15
55.5	8370	9402	8974	7.24
60.5	9557	9799	9656	7.33
65	9860	10451	10148	9.15
70.5	10604	10913	10740	9.29
75	10864	11472	11140	11.25
80	11233	11943	11577	11.43
82.5	11426	12165	11796	11.42
85	11649	12363	12015	11.44
87.5	11889	12548	12231	11.57
90	12172	12723	12451	11.35
92.5	12393	12977	12687	10.62
95	12634	13185	12921	10.65
97.5	12913	13360	13151	10.86
100	13268	13740	13484	7.52
102.5	13439	14018	13705	11.29
105	13629	14315	13959	9.83
107.5	13862	14571	14212	9.89
110	14099	14789	14463	9.96
112.5	14385	14973	14711	10.09
115	14764	15137	14959	10.10
117.5	15026	15382	15202	10.26
120	15220	15695	15451	10.06
122.5	15483	15929	15703	9.92
125	15696	16253	15960	9.74
127.5	15911	16523	16211	9.94
130	16173	16770	16463	9.92
135	16555	17502	16995	9.39
140	16966	18166	17524	9.45
145	17408	18763	18056	9.40
150	17857	19370	18591	9.35
154.5	18278	19889	19063	9.53
159.5	18781	20422	19594	9.42
164.5	19292	20977	20129	9.36
169.5	19784	21492	20655	9.49
174.5	20326	22024	21189	9.38
179.5	20875	22530	21722	9.37
184.5	21422	23013	22254	9.41
189.5	21990	23503	22783	9.45
194.5	22597	23976	23320	9.30
199.5	23190	24370	23802	10.39

Table B.6 Estimates of TR163-23 $\Delta^{14}C_0$, $\Delta^{14}C_{0\text{-atm}}$, and reservoir ages using the Hulu-tuned age model.

TR163-23 depth (cm)	Hulu-tuned mean age (yrs BP)	*N. dutertrei*							Mixed benthic							
		$\Delta^{14}C_0$ (‰)	+ 2σ	- 2σ	$\Delta^{14}C_{0\text{-atm}}$ (‰)	+ 2σ	- 2σ	Reservoir age (14C yrs)	±	$\Delta^{14}C_0$ (‰)	+ 2σ	- 2σ	$\Delta^{14}C_{0\text{-atm}}$ (‰)	+ 2σ	- 2σ	Reservoir age (14C yrs)	±
5	1980	-62.47	19.7	16.1	-50.62	20.0	16.1	413	77	-218.76	15.7	13.6	-206.91	15.3	13.8	1878	83
30	5451									-159.93	97.2	91.9	-229.04	99.1	92.9	1926	454
60.5	9656	37.29	18.3	12.2	-50.28	18.6	12.9	360	43	-104.98	15.6	11.6	-192.55	15.6	12.1	1545	62
70.5	10727	64.73	19.1	16.9	-58.77	20.3	16.5	426	73	-77.29	17.0	14.7	-200.79	17.3	14.8	1576	91
75	11058									-98.05	25.3	23.4	-243.83	27.3	26.2	1915	110
80	11424									-77.27	26.0	23.0	-227.59	29.0	24.8	1755	77
85	11885	40.38	49.6	41.8	-146.18	52.5	43.8	1036	121	-113.97	41.8	35.7	-300.53	44.2	37.6	2326	128
87.5	12116	40.94	51.3	47.4	-161.85	53.3	51.8	1154	126								
90	12357	-27.62	48.6	48.5	-239.40	48.0	52.0	1770	195	-118.15	42.9	42.6	-329.93	44.5	44.2	2555	203
92.5	12599	43.29	48.8	49.5	-171.46	50.1	50.3	1237	264	-87.38	42.2	46.2	-302.14	41.8	48.2	2312	262
95	12832	12.78	42.7	48.1	-197.67	44.5	48.3	1465	270	-114.07	35.3	43.6	-324.53	38.4	44.4	2540	271
97.5	13075	133.88	36.6	45.7	-69.27	36.5	47.3	511	186	-33.13	30.7	39.7	-236.29	30.8	40.8	1791	191
100	13317	55.87	23.7	23.4	-142.90	24.1	22.7	1020	122	-111.35	20.5	19.8	-310.12	20.4	19.7	2405	119
102.5	13561	33.40	34.3	29.8	-162.03	33.7	30.5	1160	155								
105	13810	118.65	40.8	37.8	-79.46	41.1	38.2	596	146	-32.37	36.2	34.0	-230.48	38.3	32.6	1761	153
107.5	14059	150.05	36.9	41.2	-54.90	38.9	42.6	409	140	-16.90	31.1	33.9	-221.86	32.3	35.6	1669	156
110	14301	142.43	29.2	28.0	-77.87	37.3	30.6	531	57								
112.5	14556	227.69	55.6	42.5	-23.45	58.9	47.4	119	71	59.97	48.3	37.3	-191.17	50.6	42.8	1299	86
115	14816	191.22	69.2	56.6	-79.54	67.9	59.1	472	166	-31.78	56.9	47.4	-302.54	58.1	49.0	2137	169
117.5	15075	77.22	73.0	60.0	-208.91	74.4	64.0	1381	207	-116.22	62.4	51.3	-402.36	64.0	53.6	2971	202
120	15334	98.24	84.6	73.0	-201.11	84.8	74.1	1311	236	-77.41	70.7	61.8	-376.76	72.8	62.7	2711	240
122.5	15592	110.35	96.4	80.7	-199.57	97.8	82.6	1283	266	-67.24	73.0	64.4	-377.16	76.7	66.8	2683	274
125	15864	72.22	95.2	83.4	-248.66	93.2	83.0	1642	290	-83.44	78.8	75.3	-404.31	81.3	76.6	2902	292
127.5	16132	158.86	106.0	93.5	-175.25	109.3	93.1	1095	300								
130	16401	126.96	106.9	97.5	-219.02	107.1	96.0	1388	310	-77.14	93.3	75.7	-423.12	96.6	78.4	2993	306
135	16945	140.98	121.2	111.5	-227.44	118.7	109.6	1450	332	-61.00	95.4	90.3	-429.42	100.6	93.6	3015	330
140	17484	57.69	116.3	110.5	-329.76	111.5	109.9	2172	414	-96.42	101.5	95.8	-483.87	99.8	97.5	3437	410
145	18030	76.56	122.7	123.8	-321.47	123.7	125.3	2098	487	-86.57	107.1	102.8	-484.60	103.7	101.7	3418	486
150	18574	88.94	115.2	128.3	-315.09	110.6	128.0	2057	509								
154.5	19067	94.25	131.7	127.0	-316.43	127.5	127.7	2048	503								
159.5	19608	118.87	126.9	123.5	-299.26	127.2	130.2	1935	471								
169.5	20684	152.35	128.7	140.3	-293.40	123.3	149.1	1854	439	-10.02	108.7	113.9	-454.13	59.1	56.1	3018	234
184.5	22295	157.91	110.1	121.5	-333.80	111.0	123.5	2071	449								
194.5	23360	157.89	95.1	104.4	-349.27	99.9	100.6	2154	330								

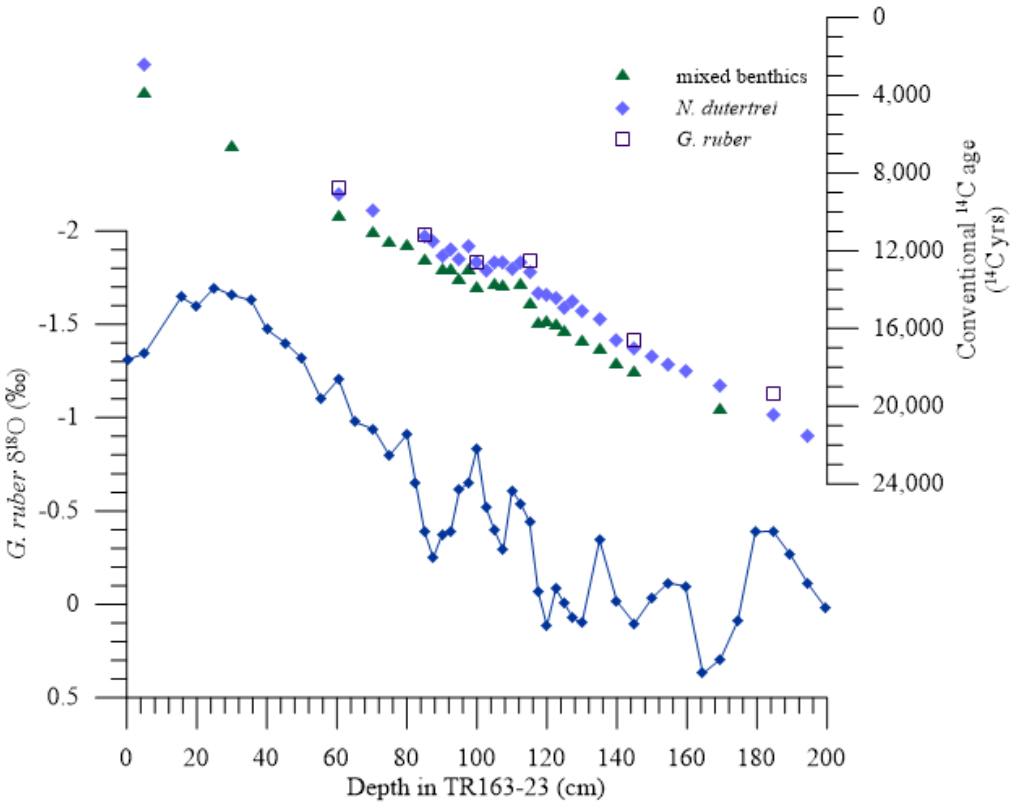

Figure B.1 TR163-23 *G. ruber* oxygen isotopes and conventional radiocarbon ages from benthic and planktonic foraminifera plotted versus core depth.

APPENDIX C

CHAPTER 2 SUPPLEMENTARY INFORMATION

Table C.1 TR163 planktonic radiocarbon ages.

Core	depth in core (cm)	UCIAMS ID	14C age (14C yrs)	±1σ	taxa
TR163-2	10	140995	8165	20	*N. dutertrei*
	20	140996	10735	25	*N. dutertrei*
	40	140997	15325	35	*N. dutertrei*
	55	142510	24000	120	*N. dutertrei*
	70	142511	34890	460	*N. dutertrei*
	85.5	142512	>49500		*N. dutertrei*
TR163-14	15	159399	10325	25	*G. ruber*
	25	159400	12045	35	*G. ruber*
	40.5	159401	16300	60	*G. ruber*
TR163-18	10	140998	7720	25	*N. dutertrei*
		157828	7985	30	*G. ruber*
	20	140999	10700	25	*N. dutertrei*
	40	141000	16370	40	*N. dutertrei*
		157829	15750	70	*G. ruber*
	50	142513	17960	70	*N. dutertrei*
	60	142514	21420	90	*N. dutertrei*
	70	142515	24880	140	*N. dutertrei*
TR163-25	40	159402	16300	60	*G. ruber*
	80	157822	12895	45	*N. dutertrei*
		157825	12685	45	*G. ruber*
	100	157823	14250	60	*N. dutertrei*
		157826	14080	60	*G. ruber*
	145	157824	20850	130	*N. dutertrei*
		157827	20490	110	*G. ruber, sacculifer*
TR163-20B	35.5	159396	9795	25	*G. ruber, sacculifer*
	50.5	159397	11170	30	*G. ruber*
	59.5	159398	12270	35	*G. ruber*

Table C.2 Reservoir ages used for radiocarbon age calibration.

	ΔR	±	Citation
Holocene	147	13	Stuiver, M., Reimer, P.J., and Reimer, R.W., 2017, CALIB 7.1 [WWW program] at http://calib.org, accessed 2017-5-27
Younger Dryas	990	30	Umling and Thunell, 2017
Bølling Allerød	101	200	Umling and Thunell, 2017
Heinrich Stadial 1	1119	171	Umling and Thunell, 2017
Last Glacial Maximum	1773	136	Umling and Thunell, 2017

Table C.3 Published data references

Core	Latitude	Longitude	Depth (m)	Holocene CO_3^{2-} µmol/kg	LGM CO_3^{2-} µmol/kg	Citation
RR0503-83	-36.7375	176.6398	1627	78.3	73.4	Allen et al., 2015
VM28-122	12	-79	3623	114.3	144.8	Yu et al., 2013
MW91-9 GGC15	0	158	2311	70	73	Yu et al., 2013
MW91-9 GGC48	0	161	3400	79	74	Yu et al., 2013
TTNO13 PC61	0.86	-140	4276	86	87	Yu et al., 2013
TNO57-21	-41.1	7.8	4981	84.4	86.9	Yu et al., 2014
BOFS 17K	58	-16.5	1150	123	154	Yu et al., 2008
BOFS 11K	55.2	-20.4	2004	117	135	Yu et al., 2008
NEAP 8K	59.8	-23.8	2360	109	134	Yu et al., 2008
BOFS 10K	54.7	-20.7	2777	110	114	Yu et al., 2008
BOFS 5K	50.7	-21.9	3547	108	90	Yu et al., 2008
BOFS 8K	52.5	-22.1	4045	105	86	Yu et al., 2008

Table C.4 *C. wuellerstorfi* carbon isotopes for TR163-23.

		C. wuellerstorfi
depth (cm)	mean age (yrs BP)	δ13C ‰ VPDB
5	1981	0.159
20	4063	0.189
40	6855	0.018
40	6855	-0.048
60.5	9657	-0.063
65	10143	0.034
70.5	10720	-0.152
75	11031	0.013
80	11372	-0.182
82.5	11602	-0.259
85	11841	-0.072
87.5	12086	-0.160
87.5	12086	-0.298
90	12326	-0.033
92.5	12564	-0.183
92.5	12564	-0.252
95	12807	-0.090
97.5	13042	-0.095
100	13281	-0.196
105	13784	-0.357
107.5	14029	-0.281
110	14275	-0.233
112.5	14530	-0.176
115	14782	-0.262
117.5	15030	-0.294
120	15280	-0.313
122.5	15533	-0.355
125	15793	-0.290
127.5	16053	-0.217
130	16320	-0.329
135	16851	-0.310
140	17378	-0.319
145	17907	-0.248
150	18434	-0.359
154.5	18909	-0.323
159.5	19427	-0.425
164.5	19984	-0.478
169.5	20548	-0.362
174.5	21110	-0.397
184.5	22246	-0.568
189.5	22812	-0.516
199.5	23943	-0.351

Table C.5 *Uvigerina* spp. carbon isotopes for TR163-23.

Uvigerina spp.

depth (cm)	mean age (yrs BP)	δ13C ‰ VPDB	replicates		
5	1981	-0.865			
15.5	3430	-0.482			
20	4063	-0.456	-0.625		
25	4759	-0.406	-0.373		
30	5469	-0.590			
35.5	6226	-0.462	-0.336	-0.484	
40	6855	-0.748	-0.603	-0.512	-0.411
45.5	7604	-0.497	-0.783		
50	8228	-0.423	-0.783	-0.587	
55.5	8996	-0.818	-0.484		
60.5	9657	-0.843	-0.771		
65	10143	-0.618	-0.755		
70.5	10720	-0.868	-0.794		
75	11031	-0.746			
80	11372	-0.667			
82.5	11602	-0.746	-1.098	-1.002	
85	11841	-1.016	-0.612		
87.5	12086	-0.761	-0.742	-1.038	-0.992
90	12326	-0.957			
92.5	12564	-1.076			
95	12807	-0.863	-0.883		
100	13281	-0.955	-1.301		
102.5	13532	-0.955	-0.842		
105	13784	-0.963	-1.108		
107.5	14029	-1.129			
110	14275	-1.283	-0.822	-1.015	
112.5	14530	-1.136			
115	14782	-0.795	-1.062		
117.5	15030	-1.103			
120	15280	-1.315	-1.043		
122.5	15533	-1.184			
125	15793	-1.294			
127.5	16053	-0.828	-1.118	-1.014	
130	16320	-0.935	-1.297	-0.743	
135	16851	-0.971	-1.199		
140	17378	-0.945			
145	17907	-1.208	-1.053		
150	18434	-1.136	-0.876	-1.115	
154.5	18909	-1.342	-1.186	-0.861	
159.5	19427	-1.004	-1.058	-1.027	
164.5	19984	-0.931			
169.5	20548	-1.202			
174.5	21110	-1.032	-1.130		
179.5	21679	-0.886			
184.5	22246	-0.968	-1.279	-0.953	
189.5	22812	-0.965	-0.951	-1.145	-0.707
194.5	23381	-1.192	-1.030		
199.5	23943	-0.797	-1.269		

Table C.6 *Globobulimina* spp. and *Chilostomella oolina* carbon isotopes for TR163-23.

		Globobulimina spp.	*Chilostomella oolina*
depth (cm)	mean age (yrs BP)	δ13C ‰ VPDB	δ13C ‰ VPDB
5	1981		-2.556
15.5	3430	-1.624	-2.269
20	4063	-1.593	-2.467
45.5	7604		-2.355
50	8228	-1.184	-2.620
55.5	8996	-1.451	-2.385
55.5	8996	-1.620	
60.5	9657	-1.841	-2.049
65	10143	-1.697	-2.264
65	10143	-1.575	
65	10143	-1.648	
70.5	10720	-1.672	-2.217
70.5	10720	-1.659	
75	11031	-1.611	-2.579
80	11372	-1.566	-2.377
82.5	11602	-1.752	
85	11841	-1.687	-2.300
90	12326	-1.647	-2.481
92.5	12564	-1.487	-2.770
92.5	12564	-1.599	
95	12807	-1.794	-2.631
97.5	13042	-1.587	-2.842
100	13281	-1.676	-2.715
107.5	14029		-2.785
115	14782	-1.607	
115	14782	-1.303	
117.5	15030	-1.787	
120	15280	-1.671	
125	15793	-1.363	-2.586
125	15793	-1.691	
130	16320	-1.662	
140	17378	-1.543	
140	17378	-1.606	
145	17907	-1.442	
150	18434	-1.413	
174.5	21110	-1.637	

Table C.7 Benthic carbon isotope difference and [O_2] estimates

TR163-23 depth (cm)	mean age (yrs BP)	Δδ13C *Uvigerina spp.* - *Globobulimina spp* ‰ VPDB	Δδ13C *C. wuellerstorfi* - *Globobulimina spp* ‰ VPDB	estimated [O2] µmol/kg
20	4063	1.052	1.782	177.15
55.5	8996	0.885		
60.5	9657	1.033	1.778	176.57
65	10143	0.954	1.674	163.18
70.5	10720	0.834	1.514	142.41
75	11031	0.866	1.624	156.69
80	11372	0.899	1.384	125.54
82.5	11602	0.803	1.493	139.71
85	11841	0.873	1.615	155.55
90	12326	0.690	1.644	159.21
92.5	12564	0.466	1.325	117.99
95	12807	0.921	1.704	167.07
97.5	13042		1.492	139.62
100	13281	0.547	1.479	137.94
117.5	15030	0.685	1.493	139.68
120	15280	0.492	1.358	122.21
125	15793	0.233	1.237	106.58
130	16320	0.670	1.333	118.98
140	17378	0.630	1.255	108.89
145	17907	0.312	1.194	101.03
150	18434	0.371	1.055	82.93
174.5	21110	0.556	1.240	106.90

Table C.8 *N. dutertrei* authigenic uranium estimates for TR163-25

depth (cm)	mean age (yrs BP)	U/Ca µmol/mol	Mn/Ca µmol/mol	U/Mn mmol/mol
0.5	3646	0.0320	108.2	0.296
5	4107	0.0428	51.9	0.825
10	4623	0.0975	111.0	0.878
15	5145	0.0552	80.6	0.684
20	5658	0.0910	87.8	1.036
25	6171	0.1007	99.3	1.013
30	6680	0.0807	79.3	1.018
35	7178	0.0751	52.4	1.433
40	7689	0.0557	50.4	1.103
45	8445	0.0839	104.0	0.807
50	9209	0.1235	150.0	0.823
55	9982	0.1468	103.6	1.417
60	10741	0.1547	161.4	0.958
65	11511	0.1439	126.8	1.135
70	12274	0.2308	201.1	1.148
75	13031	0.1283	99.2	1.293
80	13789	0.2270	114.7	1.979
85	14299	0.1794	198.4	0.904
87.5	14554	0.5547	162.9	3.405
90	14802	0.2950	220.5	1.337
92.5	15054	0.3456	183.5	1.883
95	15307	0.2093	116.2	1.802
97.5	15558	0.4189	131.2	3.194
100	15809	0.2684	125.4	2.140
102.5	16132	0.3963	136.7	2.899
105	16469	0.1881	123.9	1.518
107.5	16812	0.3787	122.3	3.097
110	17156	0.2493	178.3	1.398
112.5	17498	0.3487	96.9	3.598
115	17839	0.1463	77.7	1.884
120	18528	0.1878	83.1	2.261
125	19205	0.1975	62.7	3.148
130	19890	0.3901	179.1	2.178
135	20580	0.2320	79.0	2.936
140	21274	0.3644	111.1	3.281
145	21957	0.3797	234.4	1.620
150	22481	0.3485	101.6	3.430
160.5	23546	0.3018	59.0	5.117
175.5	25071	0.2382	41.0	5.813
180.5	25574	0.5889	117.1	5.028
185.5	26079	0.4534	97.6	4.644
190.5	26591	0.6140	194.2	3.162
195.5	27101	0.5064	115.7	4.378
200.5	27611	0.4063	83.0	4.897

Table C.9 *N. dutertrei* authigenic uranium estimates for TR163-23

depth (cm)	mean age (yrs BP)	U/Ca µmol/mol	Mn/Ca µmol/mol	U/Mn mmol/mol
0.5	1500	0.039	147.4	0.262
5	1981	0.012	145.9	0.083
15.5	3430	0.024	110.4	0.218
20	4063	0.029	60.2	0.482
25	4759	0.033	81.9	0.399
30	5469	0.028	101.8	0.273
35.5	6226	0.031	104.0	0.297
40	6855	0.072	171.9	0.416
45.5	7604	0.031	163.1	0.191
50	8228	0.033	213.4	0.153
55.5	8996	0.033	79.0	0.419
60.5	9657	0.040	56.2	0.720
65	10143	0.043	74.2	0.578
70.5	10720	0.038	90.2	0.420
75	11031	0.034	66.5	0.516
80	11372	0.084	118.7	0.708
82.5	11602	0.082	76.8	1.066
85	11841	0.080	112.6	0.713
87.5	12086	0.082	78.4	1.052
90	12326	0.091	117.4	0.776
92.5	12564	0.098	88.5	1.112
95	12807	0.052	71.3	0.733
97.5	13042	0.092	96.6	0.956
100	13281	0.055	89.3	0.615
102.5	13532	0.103	121.1	0.849
105	13784	0.072	140.1	0.512
107.5	14029	0.098	126.4	0.775
110	14275	0.081	140.1	0.578
112.5	14530	0.045	66.7	0.674
115	14782	0.086	226.2	0.380
117.5	15030	0.113	210.9	0.536
120	15280	0.052	125.8	0.417
122.5	15533	0.107	245.9	0.435
125	15793	0.070	151.1	0.462
127.5	16053	0.070	140.7	0.495
130	16320	0.075	173.7	0.429
135	16851	0.084	147.8	0.566
140	17378	0.080	162.8	0.494
145	17907	0.076	173.2	0.437
150	18434	0.070	165.1	0.425
154.5	18909	0.096	177.1	0.542
159.5	19427	0.070	148.5	0.472
164.5	19984	0.139	260.6	0.533
169.5	20548	0.038	102.5	0.375
174.5	21110	0.056	179.4	0.309
179.5	21679	0.071	164.1	0.430
184.5	22246	0.097	254.6	0.380
189.5	22812	0.065	208.4	0.311
194.5	23381	0.074	205.5	0.361
199.5	23943	0.109	168.5	0.646

Table C.10 *N. dutertrei* authigenic uranium estimates for TR163-20B

depth (cm)	mean age (yrs BP)	U/Ca µmol/mol	Mn/Ca µmol/mol	U/Mn mmol/mol
0.75	7016	0.0277	254.6	0.109
5.25	7480	0.0328	246.3	0.133
10.5	8019	0.0555	566.6	0.098
15.5	8533	0.0648	398.6	0.163
20.5	9044	0.0592	223.0	0.266
25.5	9559	0.0809	254.0	0.319
30.5	10074	0.1247	385.3	0.324
35.5	10574	0.1235	347.5	0.355
40.5	10933	0.1572	384.0	0.409
45.75	11311	0.1579	417.5	0.378
50.5	11655	0.1464	722.3	0.203
54.25	12016	0.1332	626.7	0.213
59.5	12529	0.1505	528.9	0.284
65.5	13130	0.1596	678.3	0.235
69.5	13538	0.1625	1066.7	0.152
75.75	14164	0.1701	977.3	0.174
80.5	14647	0.1314	733.1	0.179
85.75	15178	0.0905	691.7	0.131
90	15613	0.1598	1319.1	0.121
95.75	16196	0.1222	707.4	0.173
100	16623	0.1233	978.6	0.126
105.75	17201	0.1208	984.3	0.123
110	17638	0.1674	1347.0	0.124
115.5	18194	0.1713	1508.9	0.114
120	18655	0.0874	611.8	0.143
125.5	19215	0.1120	1138.3	0.098
130	19675	0.1905	1540.4	0.124
135.5	20232	0.1318	1140.6	0.116
140	20684	0.1245	1311.9	0.095
145.5	21239	0.1216	979.5	0.124
150	21700	0.0904	978.7	0.092

Table C.11 TR163-14 and TR163-20B Bulk planktonic authigenic uranium estimates

TR163-14

depth (cm)	mean age (yrs BP)	[U] ppm	[Mn] ppm	U/Mn
0.5	8296	0.0376	186.4	0.202
5.5	9147	0.0333	127.7	0.261
10.5	10232	0.0309	38.2	0.808
25	12964	0.0534	40.5	1.318
40.5	16967	0.2527	29.3	8.638
60	20919	0.3218	38.2	8.434
80	24990	0.1641	44.1	3.724

TR163-20B

depth (cm)	mean age (yrs BP)	[U] ppm	[Mn] ppm	U/Mn
15.5	8533	0.1182	115.7	1.022
30.5	10074	0.1596	128.8	1.240
65.5	13130	0.3233	352.6	0.917
85.75	15178	0.2844	488.8	0.582
100	16623	0.2260	479.7	0.471
115.5	18194	0.1910	457.9	0.417
150	21700	0.2236	509.6	0.439

Table C.12 Trace element data for TR163-2, TR163-14, and TR163-20B.

TR163-2 *C. mundulus*

depth (cm)	mean age (yrs BP)	Al/Ca µmol/mol	Mn/Ca µmol/mol	Fe/Ca µmol/mol	B/Ca µmol/mol	ΔCO_3^{2-} µmol/kg	CO_3^{2-} µmol/kg
5	6182	1291	100	96	147	38.7	95.0
10	8689	1103	127	71	141	31.3	87.5
15	10381	1395	109	67	129	13.4	69.6
25	13356	1179	121	123	146	38.3	94.6
30	14674	951	100	63	143	32.9	89.2
35	16004	959	109	58	128	11.0	67.3
40	17359	619	68	64	137	25.3	81.5
45	20371	1583	61	102	148	40.5	96.8

TR163-14

depth (cm)	mean age (yrs BP)	Al/Ca µmol/mol	Mn/Ca µmol/mol	Fe/Ca µmol/mol	B/Ca µmol/mol	ΔCO_3^{2-} µmol/kg	CO_3^{2-} µmol/kg
10	10232	382	74	46	197	17.8	84.4
14.5	11168	134	68	17	179	2.1	68.7
24.5	12964	208	76	30	187	9.4	76.0
24.5	12964	769	93	46	169	-6.3	60.3
30.5	14365	160	92	43	191	12.7	79.3
34.5	15529	299	79	39	211	30.2	96.8
40	16967	36	82	11	181	4.0	70.6
40	16967	157	81	122	177	0.2	66.7
44.5	17893	382	92	64	178	0.9	67.5

TR163-18

depth (cm)	mean age (yrs BP)	Al/Ca µmol/mol	Mn/Ca µmol/mol	Fe/Ca µmol/mol	B/Ca µmol/mol	ΔCO_3^{2-} µmol/kg	CO_3^{2-} µmol/kg
0.5	6085	173	155	9	201	21.0	84.1
5	7063	248	118	24	203	23.2	86.3
10	8171	281	151	13	190	12.2	75.3
10	8171	1135	141	770	202	22.6	85.7
15	10048	119	170	77	199	19.4	82.6
15	10048	104	176	10	194	15.6	78.8
25	13252	77	223	20	222	40.2	103.3
30	14598	80	296	24	210	29.6	92.8
30	14598	178	281	24	206	26.2	89.3
35	15949	134	340	26	189	11.0	74.1
40	17297	227	410	29	200	20.8	83.9
40	17297	274	332	38	217	35.4	98.5
40	17297	160	287	19	203	23.2	86.3
45	18364	131	370	45	190	11.6	74.7
45	18364	116	255	25	194	15.6	78.8
50	19426	109	201	19	215	33.5	96.6
50	19426	163	220	58	202	22.5	85.6
55.5	21356	62	263	16	204	24.4	87.5
60	23283	89	369	25	200	20.4	83.5
65	25016	121	354	23	185	7.6	70.8
65	25016	113	276	20	214	33.2	96.3
70	26734	103	305	26	221	38.6	101.7

Table C.13 Trace element data for TR163-25

depth (cm)	mean age (yrs BP)	Al/Ca µmol/mol	Mn/Ca µmol/mol	Fe/Ca µmol/mol	B/Ca µmol/mol	ΔCO_3^{2-} µmol/kg	CO_3^{2-} µmol/kg
0.5	3646	425	97	19	200	20.6	90.7
10	4623	8	159	13	194	15.5	85.6
20	5658	540	219	496	192	13.3	83.4
25	6171	144	206	11	197	17.6	87.6
30	6680	137	209	249	190	12.1	82.1
35	7178	13	217	14	200	20.5	90.5
35	7178	1235	197	31	199	20.0	90.0
40	7689	406	311	20	185	7.2	77.3
50	9209	76	249	12	186	8.5	78.5
55	9982	113	151	19	226	43.1	113.1
60	10741	467	220	15	204	24.4	94.4
60	10741	149	253	26	179	2.2	72.2
65.5	11511	63	317	10	197	18.2	88.3
65	11511	283	234	30	197	17.9	87.9
70	12274	104	195	7	197	18.2	88.2
70	12274	896	172	313	224	41.9	112.0
70	12274	853	170	310	225	42.8	112.9
75	13031	858	171	311	225	42.5	112.5
80	13789	197	204	34	180	2.9	72.9
85	14299	154	167	36	193	14.8	84.8
87.5	14554	80	184	1	182	4.6	74.7
87.5	14554	199	177	44	200	20.4	90.4
90	14802	112	157	16	206	26.2	96.2
92.5	15054	218	174	24	189	10.7	80.8
95	15307	651	245	20	194	15.1	85.2
95	15307	419	151	23	198	18.4	88.4
100	15809	341	160	43	192	13.8	83.8
102.5	16132	76	219	14	178	1.6	71.6
105	16469	442	178	38	195	16.3	86.3
110	17156	330	177	24	194	15.2	85.2
112.5	17498	368	131	45	199	20.0	90.1
115	17839	158	156	24	204	24.0	94.0
125	19205	454	161	28	176	-0.2	69.8
125	19205	430	162	42	185	7.0	77.1
130	19890	72	221	22	170	-6.2	63.8
130	19890	66	178	10	186	8.4	78.5
135	20580	64	189	16	193	14.1	84.1
135	20580	179	152	24	197	17.9	87.9
140	21274	84	174	22	176	-0.4	69.7
145	21957	248	181	29	179	1.9	72.0
145	21957	129	181	15	182	4.8	74.9
150	22481	335	180	23	185	7.4	77.5
155.5	23034	182	160	18	183	6.0	76.0
160.5	23546	112	173	18	188	10.3	80.3
165.5	24057	34	140	19	193	14.1	84.1
170.5	24564	134	155	24	187	9.2	79.2
175.5	25071	105	152	25	179	2.5	72.5
175.5	25071	383	166	14	203	23.1	93.1
180.5	25574	228	149	28	200	20.5	90.6
185.5	26079	171	157	29	217	35.6	105.6
190.5	26591	195	162	39	163	-12.0	58.0
195.5	27101	90	178	13	192	13.8	83.8
195.5	27101	256	165	38	188	10.3	80.4
200.5	27611	99	149	35	190	11.8	81.8

Table C.14 Trace element data for TR163-23

depth (cm)	mean age (yrs BP)	Al/Ca µmol/mol	Mn/Ca µmol/mol	Fe/Ca µmol/mol	B/Ca µmol/mol	ΔCO_3^{2-} µmol/kg	CO_3^{2-} µmol/kg
20	4063	30	152	28	209	28.5	101.4
60.5	9657	169	181	35	195	15.8	88.7
65	10143	40	245	39	181	3.9	76.7
70.5	10720	116	191	29	211	30.4	103.3
80	11372	542	235	77	187	9.3	82.2
90	12326	335	231	136	178	1.0	73.9
92.5	12564	44	172	37	192	13.8	86.7
95	12807	178	231	42	184	6.4	79.3
97.5	13042	152	194	32	200	20.3	93.2
100	13281	315	179	63	193	14.2	87.1
102.5	13532	349	312	191	208	27.7	100.6
107.5	14029	244	251	47	200	20.1	93.0
110	14275	876	317	59	220	38.2	111.1
112.5	14530	115	190	35	193	14.7	87.6
115	14782	193	193	87	219	37.1	110.0
117.5	15030	276	243	64	203	22.9	95.8
120	15280	32	327	89	204	24.0	96.9
125	15793	116	254	45	199	19.5	92.4
130	16320	179	271	49	192	13.8	86.7
135	16851	476	274	278	197	18.2	91.1
135	16851	773	236	135	174	-2.2	70.7
140	17378	70	283	51	215	33.4	106.2
140	17378	118	194	26	191	12.5	85.3
145	17907	74	288	48	175	-1.3	71.6
145	17907	159	260	72	193	14.4	87.3
150	18434	81	308	72	194	15.3	88.1
154.5	18909	152	130	34	205	25.0	97.9
179.5	21679	38	341	1005	199	19.8	92.7
184.5	22246	200	274	52	205	24.6	97.5
189.5	22812	99	363	76	216	34.3	107.2

Table C.15 Trace element data for TR163-20B

depth (cm)	mean age (yrs BP)	Al/Ca µmol/mol	Mn/Ca µmol/mol	Fe/Ca µmol/mol	B/Ca µmol/mol	ΔCO_3^{2-} µmol/kg	CO_3^{2-} µmol/kg
30.5	10078	212	353	24	194	15.4	91.2
40.5	11036	1086	453	63	197	18.2	94.0
45.75	11490	135	338	7	206	25.4	101.1
54.25	12290	636	431	64	182	5.0	80.7
59.5	12836	40	398	24	199	20.1	95.8
65.5	13852	110	603	25	187	9.3	85.0
75.75	14457	82	648	16	197	17.8	93.5
80.5	14961	143	574	15	209	28.8	104.5
90	15466	58	472	10	181	3.5	79.3
95.75	15923	106	545	742	190	11.7	87.4
100	16480	97	526	66	191	12.3	88.1
105.75	16939	191	448	14	203	23.3	99.0
110	17492	152	515	34	180	2.8	78.6
115.5	17951	95	601	33	168	-7.4	68.4
125.5	18966	105	444	7	197	17.9	93.7
130	19521	130	808	19	176	-0.8	75.0
135	19976	116	712	49	197	17.7	93.5
140	20540	100	828	19	181	3.8	79.5
145.5	20992	80	661	15	175	-1.0	74.7
150	21552	108	505	35	203	23.2	99.0

Table C.16 Eastern equatorial Pacific profiles of carbonate ion concentration

Core	Core depth	Modern CO_3^{2-} µmol/kg	Holocene CO_3^{2-} µmol/kg	Bolling Allerod CO_3^{2-} µmol/kg	LGM CO_3^{2-} µmol/kg
TR163-2	1620	56.26	84.0	91.9	89.2
TR163-18	2030	63.14	82.1	95.2	86.7
TR163-14	2365	66.57	84.4	79.3	68.3
TR163-25	2650	70.04	87.1	83.8	79.3
TR163-23	2730	72.88	92.5	97.5	99.1
TR163-20B	3200	75.76	95.4	94.4	84.4

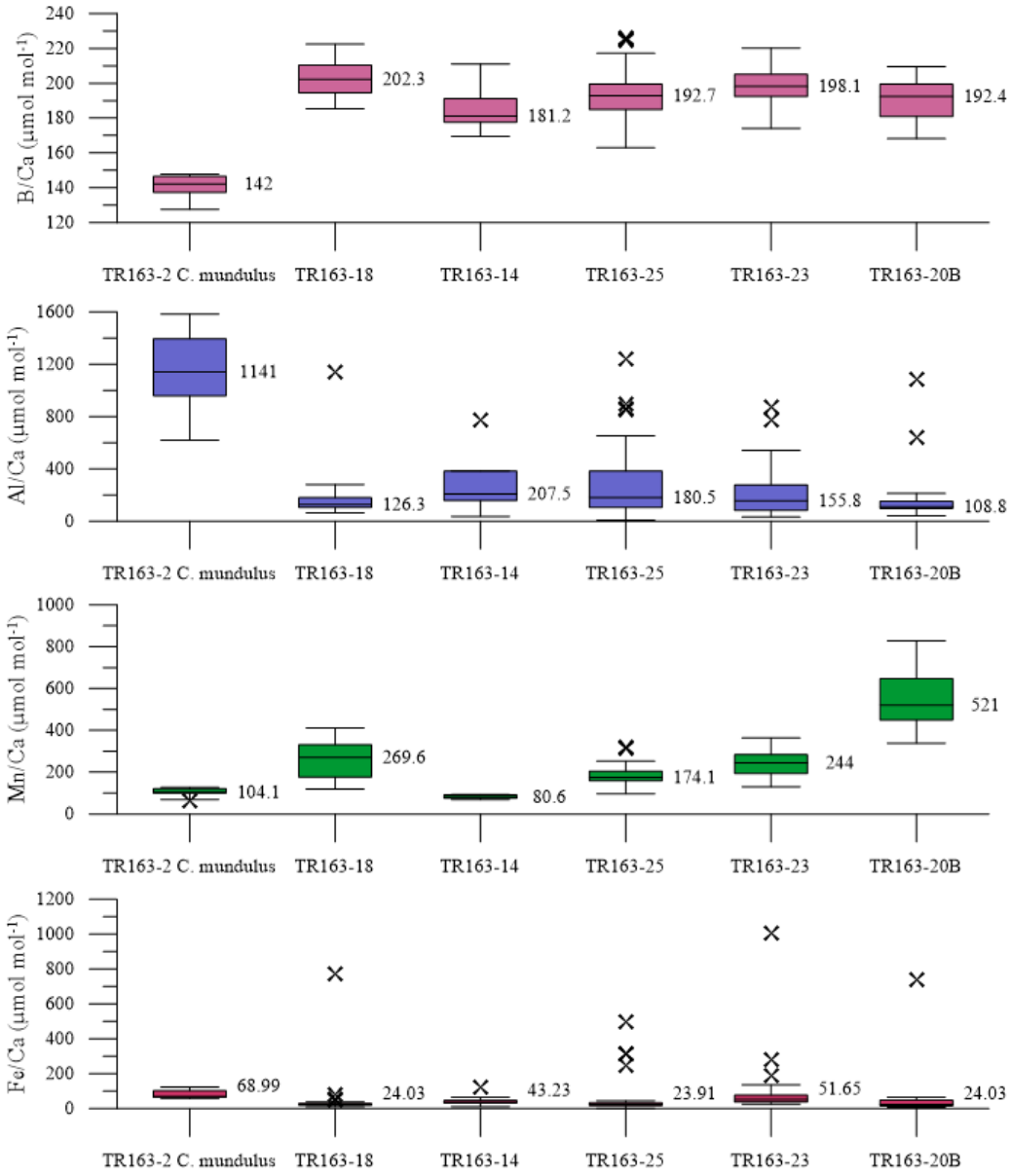

Figure C.1 Box and whisker plots of trace element ratios to calcium. Median values are labeled and outliers are marked with an X. Benthic foraminifera species *Cibicidoides wuellerstorfi* was utilized for each core except for TR163-2 which utilized *Cibicidoides mundulus.*

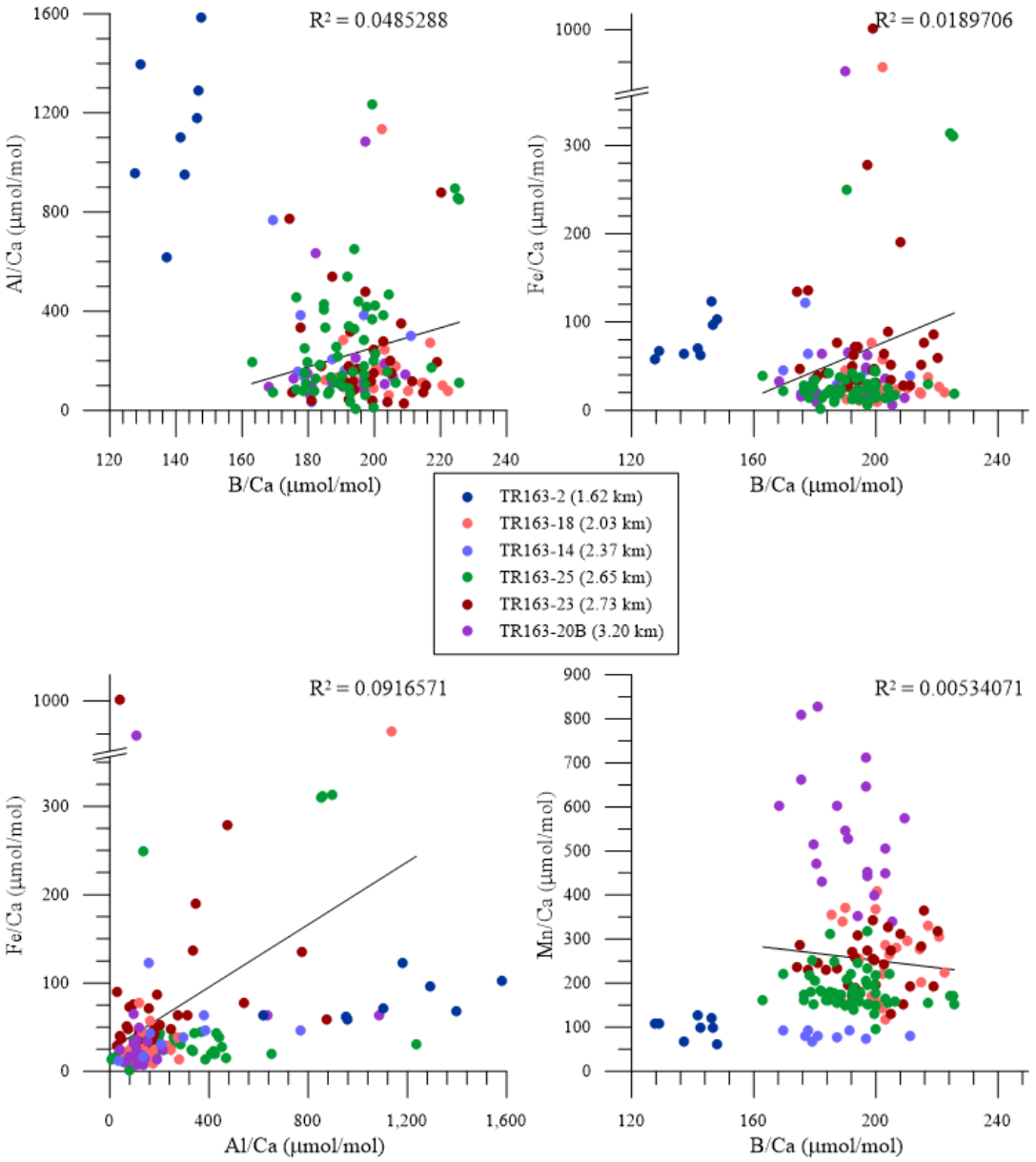

Figure C.2 Boron does not show a correlation with any of the diagenetic indicators. TR163-2 *C. mundulus* values were not included in calculation of the R^2 value.

APPENDIX D

CHAPTER 3 SUPPLEMENTARY INFORMATION

Table D.1 Age models for TR163-2, TR163-18, TR163-14

TR163-2

depth (cm)	mean age (yrs BP)	min age (yrs BP)	max age (yrs BP)
0.5	3725	937	6089
5	6182	3260	7615
10	8689	8481	9019
15	10381	9531	11184
20.25	12022	11601	12330
25	13356	12517	14393
30	14674	13622	15852
35	16004	14923	17258
40	17359	16555	18576
45	20371	18540	22375
50	23351	21355	25043
55	26326	25793	27097
60	29731	27783	31925

TR163-18

depth (cm)	mean age (yrs BP)	min age (yrs BP)	max age (yrs BP)
0.5	6085	4817	6977
5	7063	6228	7673
10	8171	8004	8421
15	10048	9121	10956
20	11922	11505	12258
25	13252	12416	14174
30	14598	13582	15603
35	15949	14961	16790
40	17297	16666	17782
45	18364	17643	19081
50	19426	18936	20123
55	21356	20303	22386
60	23283	22703	23827
65	25016	24020	26032
70	26734	25777	27425

TR163-14

depth (cm)	mean age (yrs BP)	min age (yrs BP)	max age (yrs BP)
1	8296	6626	9520
5	9147	7796	10141
10	10232	9339	10841
14.5	11168	10967	11319
20	12157	11627	12782
24.5	12964	12380	13702
30	14365	13438	15316
34.5	15529	14572	16424
40	16967	16205	17551
44.5	17893	16953	18842
50	19011	17827	20269

Table D.2 Age model for TR163-25

TR163-25			
depth (cm)	mean age (yrs BP)	min age (yrs BP)	max age (yrs BP)
0.5	3646	2203	4641
5	4107	2754	5062
10	4623	3409	5515
15	5145	4060	5971
20	5658	4683	6388
25	6171	5332	6798
30	6680	5996	7171
35	7178	6669	7519
40	7689	7557	7835
45	8445	7960	9093
50	9209	8510	10000
55	9982	9143	10878
60	10741	9825	11679
65	11511	10543	12465
70	12274	11299	13173
75	13031	12078	13846
80	13789	12875	14478
85	14299	13401	15061
87.5	14554	13679	15360
90	14802	13952	15644
92.5	15054	14215	15916
95	15307	14480	16187
97.5	15558	14764	16465
100	15809	15048	16745
102.5	16132	15313	17089
105	16469	15579	17459
107.5	16812	15864	17839
110	17156	16144	18199
112.5	17498	16431	18576
115	17839	16732	18926
120	18528	17291	19669
125	19205	17887	20342
130	19890	18489	21003
135	20580	19104	21647
140	21274	19701	22280
145	21957	20303	22845
150	22481	20768	23509
155.5	23034	21274	24176
160.5	23546	21754	24788
165.5	24057	22224	25379
170.5	24564	22675	25954
175.5	25071	23160	26537
180.5	25574	23625	27112
185.5	26079	24091	27664
190.5	26591	24573	28247
195.5	27101	25032	28816
200.5	27611	25518	29375

Figure D.3 Age model for TR163-20B

TR163-20B			
depth (cm)	mean age (yrs BP)	min age (yrs BP)	max age (yrs BP)
0.75	7014	5858	7977
5.25	7477	6394	8359
10.5	8043	7092	8833
15.5	8556	7714	9256
20.5	9060	8324	9654
25.5	9567	8944	10042
30.5	10078	9637	10403
35.5	10585	10408	10738
40.5	11036	10738	11395
45.75	11490	11100	11927
50.5	11943	11494	12432
54.25	12290	11791	12803
59.5	12836	12283	13357
65.5	13444	12787	14127
69.5	13852	13122	14608
75.75	14457	13633	15323
80.5	14961	14048	15909
85.75	15466	14495	16496
90	15923	14892	17045
95.75	16480	15392	17664
100	16939	15796	18153
105.75	17492	16275	18770
110	17951	16693	19284
115.5	18511	17186	19899
120	18966	17585	20421
125.5	19521	18074	21035
130	19976	18505	21523
135.5	20540	19010	22139
140	20992	19414	22634
145.5	21552	19923	23229
150	22003	20330	23731

Table D.4 Benthic carbon isotopes for TR163-25

TR163-25		*C. wuellerstorfi*	
Depth (cm)	Age (yrs BP)	δ13C (‰ VPDB)	δ18O (‰ VPDB)
0.5	3646	0.136	2.798
5	4107	0.081	3.097
15	5145	0.079	2.579
20	5658	-0.034	2.724
25	6171	0.046	2.754
30	6680	-0.040	2.912
35	7178	0.020	3.275
40	7689	0.022	3.253
45	8445	0.032	2.890
60	10741	0.015	3.245
65	11511	-0.076	3.367
70	12274	-0.048	3.542
75	13031	-0.104	3.630
80	13789	-0.208	3.801
85	14299	-0.167	3.889
87.5	14554	-0.265	4.032
90	14802	-0.295	4.145
95	15307	-0.340	4.045
97.5	15558	-0.352	3.772
100	15809	-0.345	4.167
102.5	16132	-0.370	4.187
105	16469	-0.363	4.242
110	17156	-0.428	4.376
112.5	17498	-0.380	4.480
115	17839	-0.389	4.258
125	19205	-0.387	4.401
130	19890	-0.367	4.062
135	20580	-0.313	4.377
140	21274	-0.353	4.327
145	21957	-0.357	4.237
155.5	23034	-0.304	4.181
160.5	23546	-0.319	4.291
165.5	24057	-0.210	4.232
170.5	24564	-0.292	4.178
175.5	25071	-0.409	3.990
180.5	25574	-0.271	4.183
185.5	26079	-0.209	4.081
190.5	26591	-0.197	4.117
195.5	27101	-0.226	4.131
200.5	27611	-0.234	4.139

Table D.5 Benthic carbon isotopes for TR163-20B

TR163-20B		*C. wuellerstorfi*	
Depth (cm)	Age (yrs BP)	δ13C (‰ VPDB)	δ18O (‰ VPDB)
0.75	7014	-0.207	3.140
20.5	9060	-0.064	2.974
25.5	9567	-0.300	2.795
45.75	11490	-0.412	3.539
50.5	11943	-0.189	3.518
54.25	12290	-0.126	3.410
59.5	12836	-0.283	3.788
65.5	13444	-0.315	4.215
69.5	13852	-0.497	4.268
75.75	14457	-0.452	4.337
80.5	14961	-0.328	4.495
85.75	15466	-0.404	4.353
90	15923	-0.428	4.543
95.75	16480	-0.403	4.416
100	16939	-0.458	4.520
105.75	17492	-0.410	4.466
110	17951	-0.317	4.417
115.5	18511	-0.365	4.404
125.5	19521	-0.447	4.340
140	20992	-0.379	4.369
145.5	21552	-0.275	4.411
150	22003	-0.274	4.211

Table D.6 Benthic Cd/Ca and Cd_W for TR163-2

TR163-2 *C. wuellerstorfi*

Depth (cm)	Age (yrs BP)	Cd/Ca µmol/mol	Cdw nmol/kg
15	10381	0.131	0.765
30	14674	0.186	1.087
45	20371	0.150	0.877
45	20371	0.150	0.877
50	23351	0.124	0.727
55	26326	0.117	0.687
60	29731	0.133	0.777

TR163-2 *C. mundulus*

Depth (cm)	Age (yrs BP)	Cd/Ca µmol/mol	Cdw nmol/kg
5	6182	0.180	1.052
10	8689	0.169	0.987
15	10381	0.138	0.810
25	13356	0.146	0.856
30	14674	0.118	0.693
35	16004	0.128	0.748
40	17359	0.130	0.765
45	20371	0.238	1.394

Table D.7 Benthic Cd/Ca and Cd_W for TR163-18 and TR163-14

TR163-18

Depth (cm)	Age (yrs BP)	Cd/Ca µmol/mol	Cdw nmol/kg
0.5	6085	0.293	1.421
15	10048	0.240	1.162
15	10048	0.259	1.257
25	13252	0.307	1.488
30	14598	0.328	1.593
30	14598	0.307	1.489
40	17297	0.333	1.616
40	17297	0.324	1.573
40	17297	0.286	1.386
40	17297	0.279	1.353
45	18364	0.236	1.147
45	18364	0.203	0.986
50	19426	0.359	1.740
50	19426	0.338	1.641
55.5	21356	0.324	1.570
60	23283	0.247	1.197
65	25016	0.297	1.442
65	25016	0.177	0.858
70	26734	0.178	0.866

TR163-14

Depth (cm)	Age (yrs BP)	Cd/Ca µmol/mol	Cdw nmol/kg
10	10232	0.244	1.039
14.5	11168	0.212	0.902
24.5	12964	0.212	0.901
24.5	12964	0.230	0.977
30.5	14365	0.222	0.946
40	16967	0.306	1.300
44.5	17893	0.259	1.101

Table D.8 Benthic Cd/Ca and Cd_W for TR163-25 0-90 cm

TR163-25

Depth (cm)	Age (yrs BP)	Cd/Ca µmol/mol	Cdw nmol/kg	δ13C (‰ VPDB)
0.5	3646	0.335	1.290	0.136
5	4107	0.292	1.124	0.081
10	4623	0.264	1.017	
15	5145	0.307	1.181	0.079
25	6171	0.321	1.236	0.046
25	6171	0.343	1.320	0.046
25	6171	0.263	1.013	0.046
30	6680	0.286	1.100	-0.040
35	7178	0.213	0.821	0.020
35	7178	0.268	1.033	0.020
40	7689	0.277	1.067	0.022
40	7689	0.254	0.979	0.022
45	8445	0.235	0.903	0.032
50	9209	0.262	1.008	
55	9982	0.204	0.785	
60	10741	0.231	0.889	0.015
60	10741	0.251	0.968	0.015
65.5	11511	0.295	1.134	-0.076
65	11511	0.272	1.048	-0.076
70	12274	0.284	1.092	-0.048
70	12274	0.264	1.017	-0.048
80	13789	0.343	1.321	-0.208
85	14299	0.232	0.895	-0.167
87.5	14554	0.220	0.846	-0.265
87.5	14554	0.274	1.054	-0.265
90	14802	0.279	1.076	-0.295

Table D.9 Benthic Cd/Ca and Cd_W for TR163-25 92.5-200.5 cm

TR163-25

Depth (cm)	Age (yrs BP)	Cd/Ca µmol/mol	Cdw nmol/kg	δ13C (‰ VPDB)
92.5	15054	0.218	0.841	
95	15307	0.214	0.823	-0.340
97.5	15558	0.265	1.020	-0.352
97.5	15558	0.227	0.873	-0.352
100	15809	0.268	1.030	-0.345
102.5	16132	0.270	1.038	-0.370
105	16469	0.318	1.226	-0.363
110	17156	0.298	1.148	-0.428
112.5	17498	0.266	1.024	-0.380
115	17839	0.281	1.081	-0.389
125	19205	0.327	1.258	-0.387
125	19205	0.260	1.002	-0.387
130	19890	0.376	1.446	-0.367
130	19890	0.276	1.063	-0.367
130	19890	0.263	1.014	-0.367
135	20580	0.289	1.113	-0.313
135	20580	0.303	1.167	-0.313
135	20580	0.373	1.437	-0.313
140	21274	0.244	0.939	-0.353
145	21957	0.269	1.037	-0.357
145	21957	0.270	1.041	-0.357
150	22481	0.238	0.918	
150	22481	0.200	0.771	
155.5	23034	0.239	0.919	-0.304
160.5	23546	0.205	0.790	-0.319
165.5	24057	0.181	0.695	-0.210
170.5	24564	0.272	1.047	-0.292
170.5	24564	0.214	0.824	-0.292
175.5	25071	0.192	0.740	-0.409
175.5	25071	0.208	0.801	-0.409
180.5	25574	0.295	1.134	-0.271
185.5	26079	0.211	0.811	-0.209
190.5	26591	0.239	0.920	-0.197
195.5	27101	0.184	0.709	-0.226
195.5	27101	0.242	0.930	-0.226
200.5	27611	0.223	0.860	-0.234

Table D.10 Benthic Cd/Ca and Cd_W for TR163-23

TR163-23

Depth (cm)	Age (yrs BP)	Cd/Ca µmol/mol	Cdw nmol/kg	δ13C (‰ VPDB)
20	4063	0.239	0.895	0.189
60.5	9657	0.279	1.044	-0.063
65	10143	0.272	1.021	0.034
70.5	10720	0.246	0.924	-0.152
75	11031	0.237	0.889	0.013
82.5	11602	0.248	0.932	-0.259
92.5	12564	0.216	0.812	-0.217
95	12807	0.309	1.158	-0.090
97.5	13042	0.279	1.045	-0.095
100	13281	0.234	0.879	-0.196
100	13281	0.204	0.766	
102.5	13532	0.238	0.892	
102.5	13532	0.257	0.963	
105	13784	0.300	1.126	-0.357
107.5	14029	0.286	1.074	-0.281
112.5	14530	0.236	0.885	-0.176
115	14782	0.177	0.663	-0.262
117.5	15030	0.228	0.855	-0.294
120	15280	0.294	1.104	-0.313
120	15280	0.300	1.126	
120	15280	0.320	1.202	
125	15793	0.259	0.971	-0.290
125	15793	0.215	0.808	-0.290
130	16320	0.290	1.087	-0.329
140	17378	0.224	0.841	-0.319
140	17378	0.196	0.734	-0.319
145	17907	0.313	1.176	-0.248
145	17907	0.235	0.883	-0.248
150	18434	0.218	0.818	-0.359
150	18434	0.210	0.787	
154.5	18909	0.218	0.816	-0.323
179.5	21679	0.182	0.683	
184.5	22246	0.167	0.628	-0.568
189.5	22812	0.180	0.675	-0.516

Table D.11 Benthic Cd/Ca and Cd_W for TR163-20B

TR163-20B

Depth (cm)	Age (yrs BP)	Cd/Ca µmol/mol	Cdw nmol/kg	δ13C (‰ VPDB)
45.75	11490	0.232	0.800	-0.412
50.5	11943	0.237	0.817	-0.189
50.5	11943	0.210	0.726	-0.189
50.5	11943	0.253	0.872	-0.189
59.5	12836	0.233	0.804	-0.283
65.5	13852	0.353	1.218	-0.315
75.75	14457	0.232	0.801	-0.452
80.5	14961	0.263	0.907	-0.328
90	15466	0.206	0.709	-0.428
95.75	15923	0.239	0.823	-0.403
100	16480	0.240	0.828	-0.458
105.75	16939	0.177	0.611	-0.410
110	17492	0.157	0.541	-0.317
115.5	17951	0.184	0.633	-0.365
125.5	18966	0.150	0.518	-0.447
130	19521	0.229	0.788	
130	19521	0.212	0.731	
135	19976	0.242	0.833	
140	20540	0.244	0.841	-0.379
145.5	20992	0.213	0.734	-0.275
150	21552	0.157	0.542	-0.274

Table D.12 Water column phosphate data and Cd estimates

GLODAP Station ID: 1894 85.827°W, 11.49°S

depth (m)	PO4 (μmol/kg)	Cd (nmol/kg)
1027	3.13	1.00
1150	3.07	0.98
1297	3.03	0.96
1444	2.97	0.94
1590	2.93	0.92
1787	2.85	0.89
1984	2.8	0.87
2178	2.76	0.85
2374	2.72	0.84
2566	2.67	0.82
2759	2.64	0.81
2953	2.63	0.80
3151	2.61	0.79
3350	2.58	0.78
3548	2.55	0.77
3745	2.51	0.75
3942	2.51	0.75
4164	2.51	0.75
4397	2.51	0.75

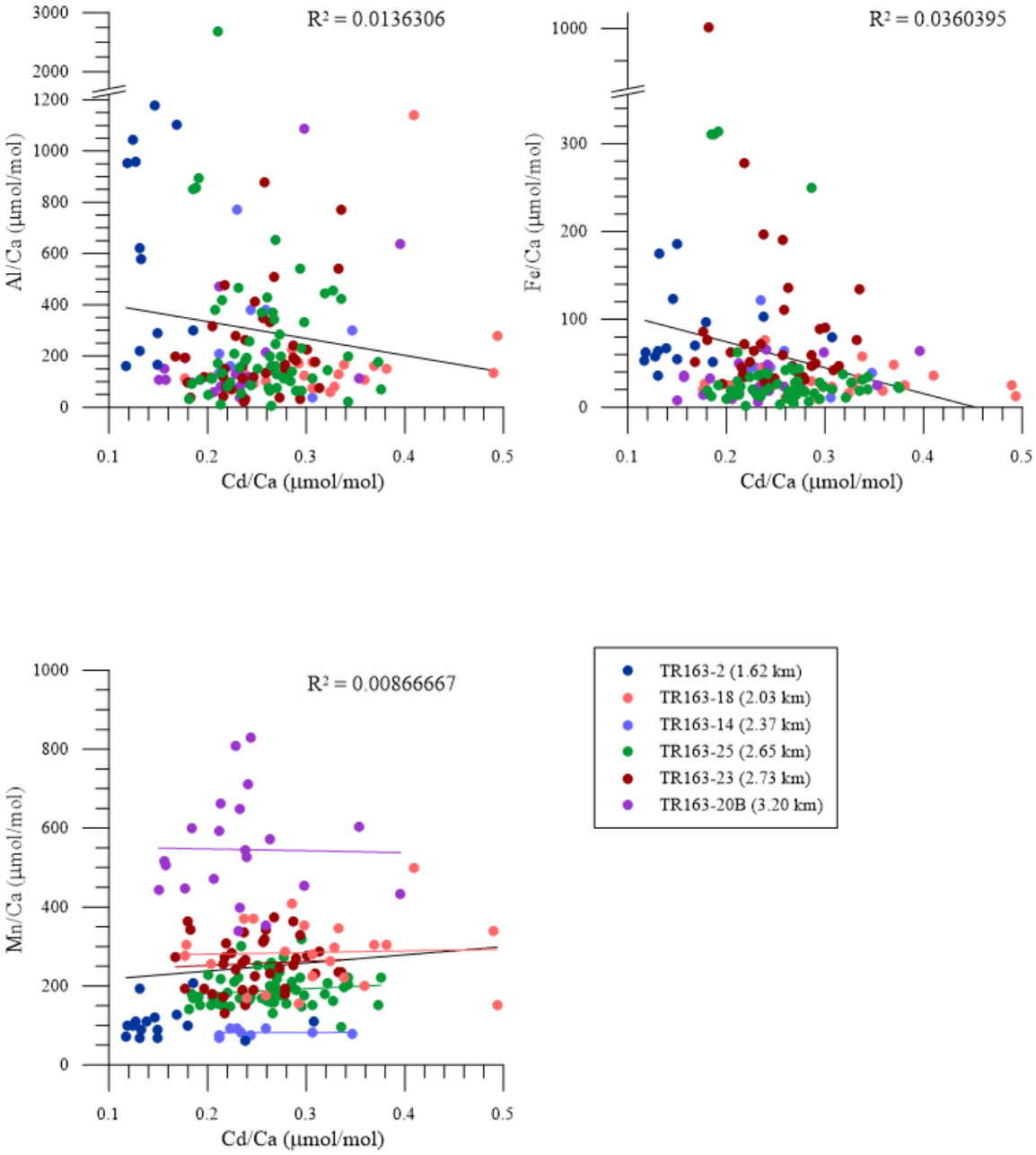

Figure D.1 Cadmium does not show a correlation with any of the diagenetic indicators.